FINE PARTICLE SYNTHESIS IN TUBULAR FLAME SYSTEMS
（管状火炎システムによる微粒子合成）

A Thesis submitted to
The Chemical Engineering Program
Graduate School of Advanced Science and Engineering
Hiroshima University

presented by

TOMOYUKI HIRANO

In Partial Fulfillment of the Requirements for the Degree of
Doctor of Engineering

Hiroshima University
March 2022

Approved by

Professor Takashi Ogi
Adviser

FINE PARTICLE SYNTHESIS IN TUBULAR FLAME SYSTEMS

TOMOYUKI HIRANO

March 2022

ACKNOWLEDGMENTS

I would like to express my deepest gratitude to Prof. Takashi Ogi, Chemical Engineering Program, Graduate School of Advanced Science and Engineering, Hiroshima University, for his continuing guidance, encouragement, support, and patience throughout the five years of my study in his laboratory.

I am grateful to Prof. Kikuo Okuyama for all their help and advice. Many thanks go to Prof. Daisuke Shimokuri who introduced me to the field of combustion science.

I wish to thank Prof. Akihiro Yabuki and Prof. Kunihiro Fukui for their patience, wisdom, and valuable comments and suggestions. My grateful thanks are also dedicated to Dr. Shuhei Nakakura, Dr. Annie Mufyda Rahmatica, and Dr. Kiet Le Anh Cao for their great support, advice, and guidance during my research.

I am grateful to Mrs. Michiyo Tachibana, Mrs. Eka Lutfi Septiani, Mr. Hiroyuki Murata, Mr. Hayato Horiuchi, Mr. Shuto Taniguchi, Mr. Hiromitsu Fukazawa, Mr. Hikaru Osakada, Mr. Kazuki Kamikubo, Mr. Chikara Nishikawa, Ms. Yuki Matsuo, Mr. Hisaaki Inaba, Mr. Kazuya Tasaka, Mr. Jun Kikkawa, Ms. Marin Nishida, Mr. Tue Tri Nguyen, Mr. Yusuke Kitou, Mr. Youhei Toyoda, Mr. Phong Hoai Le, Mr. Takama Tsuboi, Mr. Shogo Kaseda, Mr. Yasuhiko Kitamoto, Mr. Ryosuke Narui, Mr. Shunki Yamashita, and all other members of the Thermal-Fluid Engineering Laboratory for their day-to-day help and kindness.

The Japan Society for the Promotion of Science (JSPS), Hosokawa Powder Technology Foundation, and Kato Foundation for Promotion of Science are acknowledged for the financial support of my research at Hiroshima University and my living allowance.

Finally, I would like to express my appreciation to my father Kazuyuki Hirano, my mother Mayumi Hirano, and my brother Souta Hirano for their patience, support, and love, without which it would have been very difficult to persevere through my many years of school.

Tomoyuki Hirano
Higashi Hiroshima,
February 2022

SUMMARY

In this dissertation, we apply a tubular flame to the reaction field in gas-phase synthesis of fine particles. Flames have been used to fabricate various functional fine particles and devices, and it is important to predict the temperature and gas concentration to control particle characteristics with high energy efficiency even in the so-called "dirty" gas phase generated by combustion. Tubular flame combustion, a new combustion technology, has high thermal and aerodynamic stability, and the flame temperature and gas composition can be controlled. In addition, the tubular structure is convenient and can be easily integrated into various gas-phase processes. As a first step toward the development of a particle synthesis process using tubular flame combustion, we developed a new tubular flame burner, investigated the effects of various combustion parameters on particle formation, and clarified the detailed flame structure by spectral analysis of chemiluminescence. A brief description of each chapter in this dissertation is given below.

Chapter 1 introduces the current research background for flame aerosol synthesis of nanostructured particles. A review of gas-phase combustion synthesis and burner types in previous research is also presented in this chapter.

In Chapter 2, we describe the development of a tubular flame burner for particle synthesis and investigate the synthesis of tungsten oxide nanoparticles by efficient use of combustion energy. When synthesizing fine particles using the flame-assisted spray pyrolysis method—which is one of the flame aerosol synthesis methods—submicron-sized particles are easily obtained owing to the size of the raw material droplets. However, by using a high-temperature tubular flame, energy can be supplied to the particles efficiently. As a result, the gasification of the particles is accelerated and they renucleate in the gas phase, resulting in the formation of tungsten oxide nanoparticles with a primary particle size of 5-20 nm.

Chapter 3, describes the successful preparation of tungsten metal nanoparticles using fuel-rich methane/air tubular flames due to the effect of reducing species in the combustion gas. Because the tubular flame structure has high-temperature combustion gas inside and low-temperature unburned gas outside, the produced particles are not affected by the unburned gas and react in the combustion gas with a controlled composition and temperature. When the composition of the combustion gas was examined under various equivalence ratio (ϕ) conditions, the oxygen concentration approached zero for $\phi > 1.0$, while the concentration of CO, a reducing species, increased significantly. Under the condition $\phi > 1.0$, tungsten trioxide was synthesized as described in the previous chapter. In addition to tungsten trioxide (WO_3), the crystalline phases of tungsten suboxide ($WO_{2.72}$) and tungsten metal (W) were precipitated. Furthermore, increasing the residence time of the particles in the tubular flame accelerated the reduction effect and caused the WO_3 and $WO_{2.72}$ phases to disappear, and only the W phase was observed. The particle size decreased with increasing residence time, and the primary particle size of the tungsten metal particles was 5–10 nm. It was shown

that the oxidation state and particle size of the flame-made particles could be widely controlled using the controlled reaction atmosphere of tubular flame combustion and by adjusting the residence time.

In Chapter 4, a direct spray type tubular flame burner was developed and its flame structure was analyzed to establish a particle synthesis system by liquid fuel combustion using a tubular flame burner. Liquid fuel (ethanol) was sprayed into the tubular flame burner from the axial direction using a two-fluid nozzle capable of transporting liquid at a high flow rate, and the characteristics of the resulting flame were evaluated. When ethanol was sprayed onto the burner with a tubular flame, a uniform tubular flame was observed. The flame appearance was observed while varying the overall equivalence ratio, and it was shown that combustion was possible for a wide range of equivalence ratios. Temperature measurements showed that the flame structure comprised high-temperature gas inside and low-temperature gas outside, and exhibited the temperature distribution characteristics of tubular flames.

Furthermore, the detailed flame structure and the effect of tubular flame combustion were investigated by measuring the intensity distribution of the chemiluminescence of the flames. It was found that when the equivalence ratio of the tubular flame was outside the combustible range, the base of the flame was lifted even when the overall equivalence ratio was in the combustible range. In contrast, if the tubular flame was in the combustible range, a stable flame could be formed from the burner base.

In Chapter 5, we summarize the results obtained in this study and detail the prospects of the tubular flame system for particle synthesis.

CONTENTS

LIST OF FIGURES

LIST OF TABLES

1

OVERVIEW: PARTICLE SYNTHESIS IN FLAMES

1.1 INTRODUCTION

Combustion synthesis in the gas phase (flame aerosol synthesis) produces fine particles with high purity and well-controlled crystallinity using the high-temperature region of flames. Owing to its versatility, it is used industrially to produce various functional materials on a large scale [1–10]. Recently, it has been recognized that such processes also have significant potential to produce high-performance catalysts [11–15] and non-aggregated particles [16, 17], and electronic devices such as batteries and gas sensors [18–21]. The following companies in Japan have obtained patents for flame-based processes and prepared materials.

- Sumitomo Electric Industries, Ltd.
- Furukawa Electric Co., Ltd.
- AGC Inc.
- TAIHEIYO CEMENT CORPORATION
- TAIYO NIPPON SANSO CORPORATION
- Shin-Etsu Chemical Co., Ltd.
- Tokuyama Corporation
- NIPPON AEROSIL CO., LTD.
- Admatechs Company Limited
- Ube Industries, Ltd.
- CHUGAI RO CO., LTD.
- Hosokawa Micron Corporation

Recent developments in the available technology have led to the science of flame aerosol synthesis also being better understood [22–29]. This chapter summarizes the basic background of the types of flame aerosol synthesis, flame-made particles, the burners used, and tubular flame combustion.

1.2 THE FLAME AEROSOL PROCESS

Flame aerosol synthesis can be classified into two general categories according to the precursor state, i.e., vapor-fed aerosol flame synthesis (VAFS), and liquid-fed aerosol flame synthesis (LAFS) [4, 6, 7, 10]. The particles are produced via various routes depending on the flame aerosol synthesis method.

1.2.1 *Vapor-fed aerosol flame synthesis (VAFS)*

In VAFS, a metal precursor in the form of vapor is transferred to a reactor for combustion. The combustion, reaction/decomposition, nucleation, and particle growth occur in external hydrocarbon or hydrogen flames. VAFS is currently the most widely used flame process in industry; however, the difficulty in obtaining volatile precursors at reasonable cost limits the use of VAFS for producing a wide variety of functional nanoparticles.

Figure 1.1 shows flame production of TiO_2 nanoparticles using a Bunsen burner. Emissions from Ti species in the flame result in the red appearance. TTIP (titanium tetraisopropoxide) vapor, a precursor of TiO_2, is supplied to CH_4/air Bunsen flames, resulting in the formation of TiO_2 nanoparticles through gas-to-particle conversion. The transition of the gaseous precursor into nanoparticles across the flame front as well as diffusion of the nanoparticles in the post-flame zone, can be visualized using laser-based diagnostics [26].

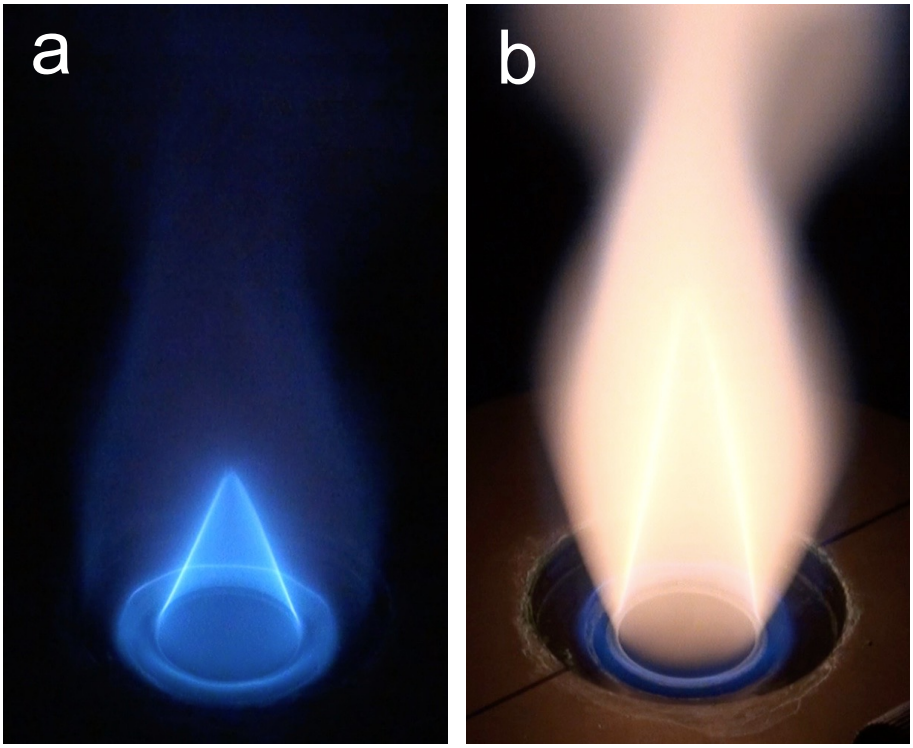

Figure 1.1: Vapor-fed aerosol flame synthesis: CH_4/air premixed Bunsen flame (a) with TTIP vapor feeding (b).

1.2.2 *Liquid-fed aerosol flame synthesis (LAFS)*

LAFS is a flame aerosol synthesis using liquid precursors. LAFS was first proposed by Sokolowaski *et al.* in 1977 for the synthesis of Al_2O_3 [30]. When the liquid precursor solution drives the combustion reaction, and the energy contribution is substantial

(more significant than 50%), LAFS is recognized as flame spray pyrolysis (FSP). When the energy contribution from the liquid precursor solution is low, it is usually called flame-assisted spray pyrolysis (FASP).

1.2.2.1 *Flame-assisted spray pyrolysis (FASP)*

In FASP, a non-combustible liquid precursor is generally sprayed and transported into the external hydrogen or hydrocarbon flames, as shown in Figure 1.2. The liquid precursors are sprayed using a two-fluid nozzle or an ultrasonic atomizer. In this method, nanoparticles are obtained when the precursor reacts in the gas phase, while hollow and/or micron-sized particles tend to be formed when the precursor precipitates in the droplet. The FASP method enables the synthesis of multicomponent nanoparticles with strictly controlled composition because the particles precipitate and react in the restricted region of the tiny droplets. In addition, as shown in Figure 1.3, the addition of energetic materials such as urea to the liquid precursor solution can promote the formation of nanoparticles [31].

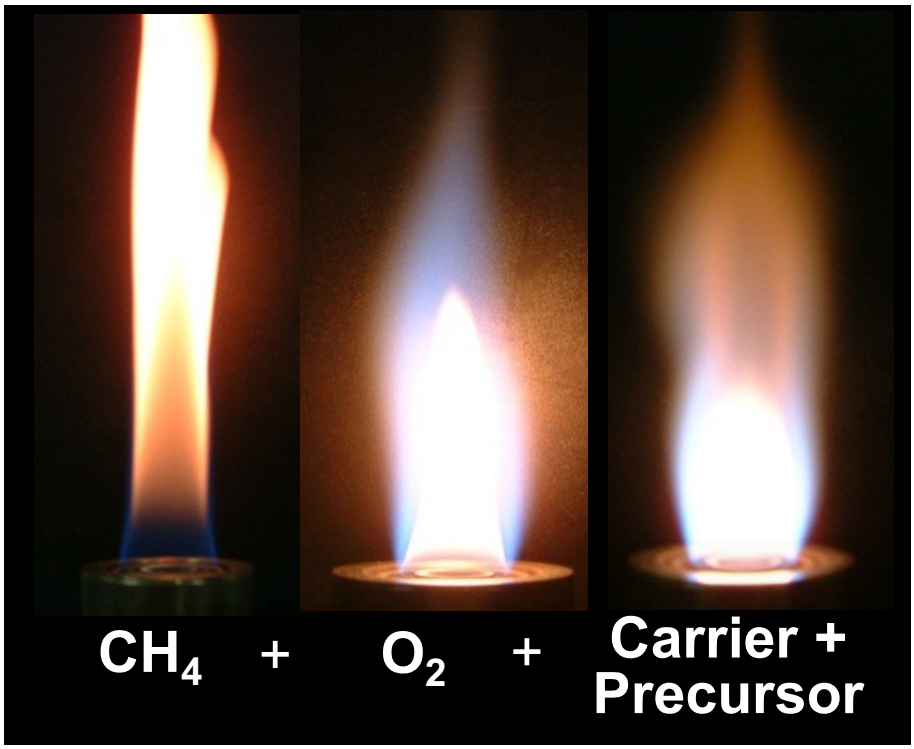

Figure 1.2: Flame-assisted spray pyrolysis.

Our group has successfully synthesized highly crystalline $Cs_{0.32}WO_3$ nanoparticles using the FASP method with diffusion flames [32]. $Cs_{0.32}WO_3$ has attracted attention as a material that can selectively absorb near-infrared radiation from sunlight. The conventional synthesis method requires many elaborate and multi-steps, including heating under a hydrogen atmosphere and mechanical grinding. By using the FASP process, $Cs_{0.32}WO_3$ nanoparticles with a narrow particle size distribution were obtained

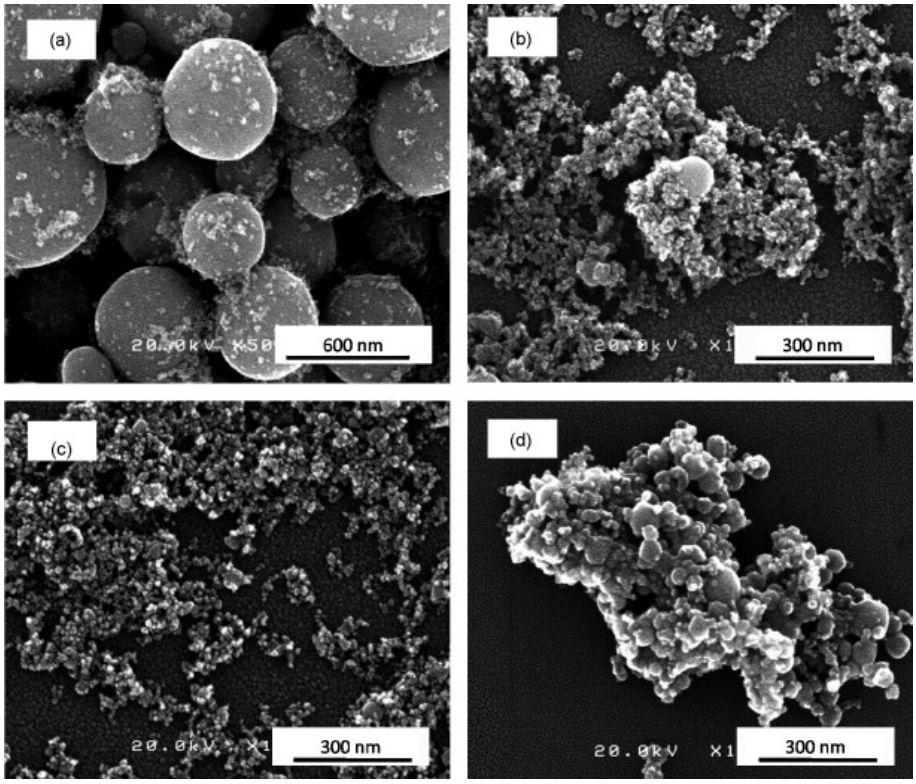

Figure 1.3: SEM images of $YAlO_3$ produced by FASP from precursor without urea (a) and with the addition of 1 M (b), 2 M (c), and 3 M (d) urea. Adapted from [31].

in only a few seconds. After annealing at 650°C for 1 h under a 5% H_2/Ar atmosphere, the prepared particles exhibited marked near-infrared shielding properties.

1.2.2.2 *Flame spray pyrolysis (FSP)*

The FSP system, outlined in Figure 1.4, is a more straightforward and more effective technique in which particles are produced in the self-sustained spray flames of precursor materials [33]. Without the dilution and interference effects of assisting flames, homogeneous nanoparticles can be produced with a higher yield. FSP is the most recent synthesis method of the three processes (VAFS, FASP, and FSP), and has critical technical elements such as spray combustion, use of liquid precursors, proven scalability, and high temperature.

Using this spray flame, our group synthesized Pt-loaded Nb-doped SnO_2 nanoparticles (Pt/Nb-SnO_2) in a single step for highly durable fuel cell catalysts [34]. Typically, PEFC cathode and anode catalysts are platinum nanoparticles supported on carbon. However, the corrosion degradation and oxidation of carbon at high temperatures and high potentials lead to limited fuel cell durability. Niobium-doped tin oxide nanoparticles have good durability when subjected to voltage cycling up to a high potential with relatively high electronic mobility and conductivity. In the aforementioned study, Pt/Nb-SnO_2 were prepared by multiple processes: (1) synthesis of Nb-SnO_2, (2) Pt

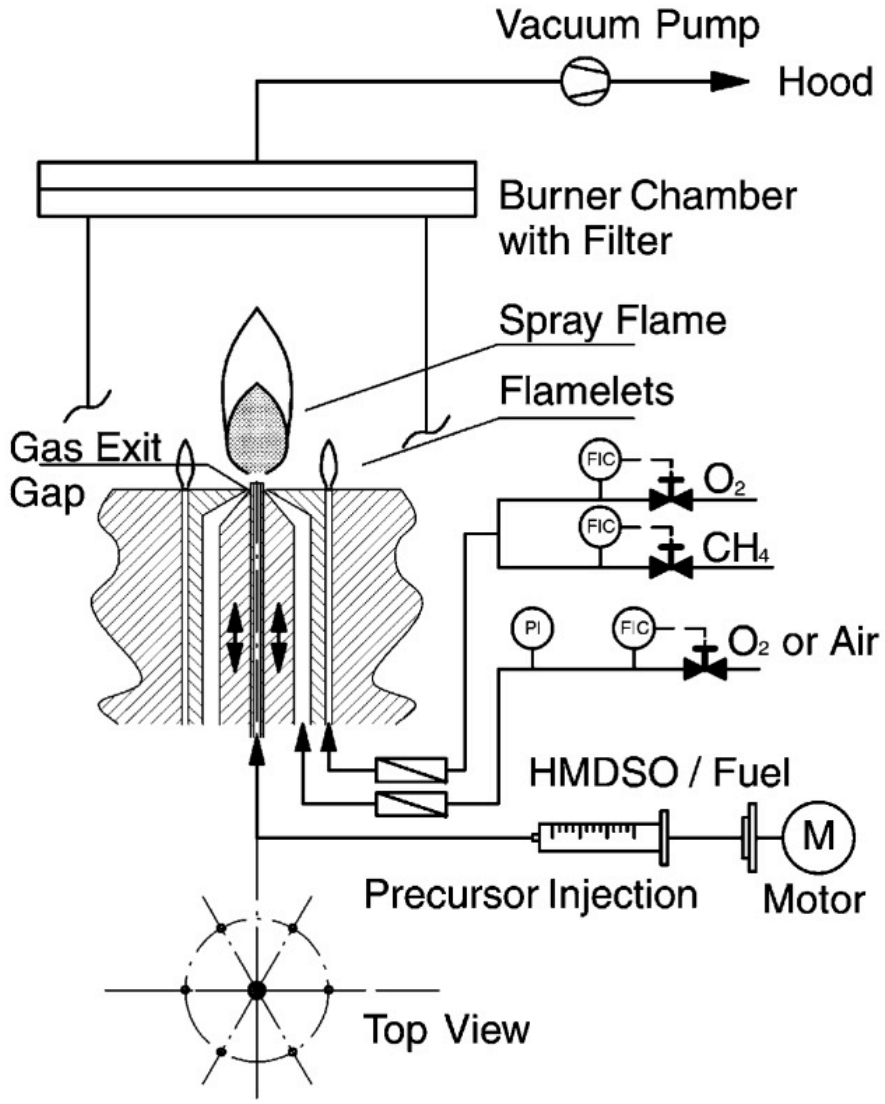

Figure 1.4: Flame spray pyrolysis. Adapted from [33].

loading, and (3) post heat treatment. By using the FSP process, Nb-SnO_2 nanoparticles with uniformly dispersed Pt catalyst were successfully synthesized through gas-to-particle conversion. The FSP-made Nb-SnO_2 nanoparticles had a unique network structure, and Pt catalyst on Nb-SnO_2 exhibited high electrochemical properties.

1.3 PROGRESS ON FLAME AEROSOL SYNTHESIS OF NANOSTRUCTURED PARTICLES AND FUNCTIONAL DEVICES

As described above, flame aerosol synthesis has been used as an industrial synthesis method for various nanoparticle materials. Currently, simple oxide and carbon nanoparticles, as well as various functional nanoparticles are being synthesized. In addition, it has been shown that flame aerosol synthesis can be used not only for the

synthesis of fine particles, but also for the direct fabrication of particle layer films and devices. Recent advances in science and technology have led to the development of in situ analysis of how particles are formed in flames using laser and spectroscopic techniques. This section introduces various kinds of particles and devices prepared using flame aerosol synthesis and their characterization methods.

1.3.1 *Particle synthesis*

Various mechanisms in flame aerosol synthesis produce fine particles. TEM images of typical metal oxide nanoparticles (SnO_2) produced by FSP are shown in Figure 1.5, and agglomerates with a primary particle size of 10–20 nm can be observed. In flame aerosol synthesis, the particle size, specific surface area, and agglomeration can be controlled by adjusting the fuel flow rate, precursor flow rate, and carrier gas flow rate. In addition, fine particles made in flames have a network structure due to the adhesion between the particles. Recently, catalyst supports for fuel cells with conductive paths have been developed using this network structure.

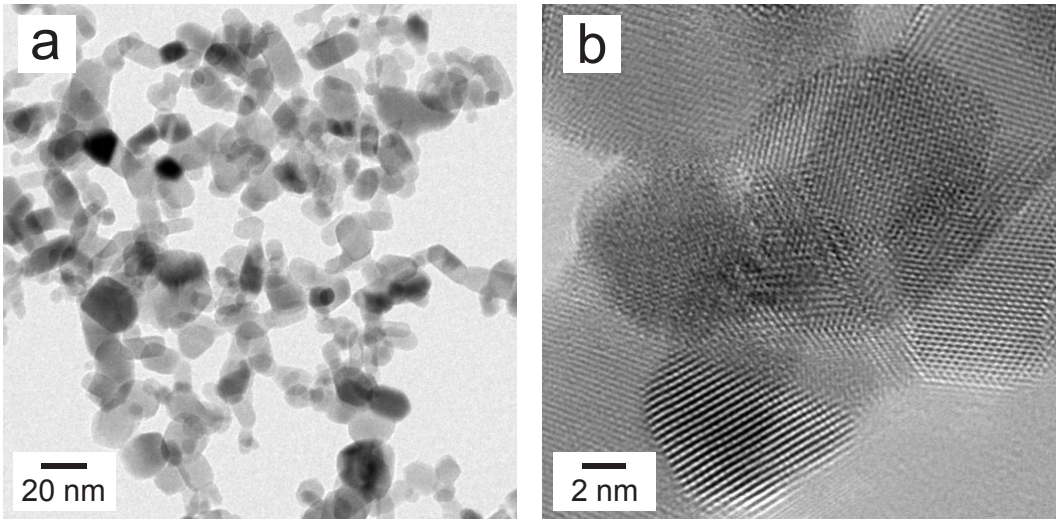

Figure 1.5: (a) TEM and (b) HR-TEM images of flame-made SnO_2 nanoparticles.

Although the flame aerosol synthesis method is based on the combustion (oxidation) reaction of materials, the degree of oxidation can be controlled by the rapid cooling of the generated particles. Blue titania with an oxygen deficiency was synthesized by cooling titanium dioxide produced by rapid quenching of diffusion flames with a flow nozzle placed at various heights above the burner [35]. The defect structures of titanium dioxide could be controlled by adjusting the burner–nozzle distance. Furthermore, it is also possible to synthesize non-oxidic salts and pure metallic nanoparticles using flame combustion in an inert atmosphere under limited oxygen supply. As shown in Figure 1.6, Stark *et al.* synthesized various non-oxidic nanoparticles using modified flame spray pyrolysis carried out in an oxygen-free glove-box filled with nitrogen [36–40]. The inert gas mixture was flowed into the spray flames from a sinter

metal tube surrounding the burner for stable combustion. Carbides and carbon-coated particles could also be synthesized by adding acetylene from the tube to the flame.

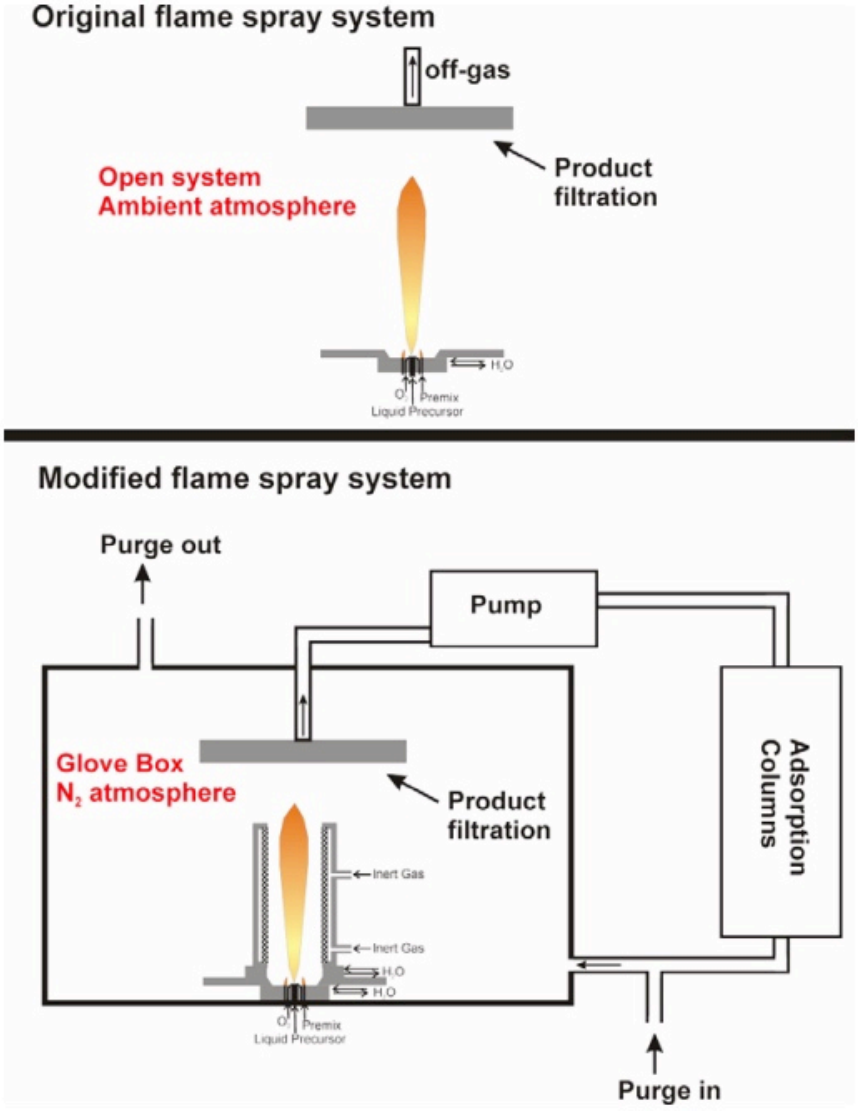

Figure 1.6: Schematic diagram showing both the original flame spray pyrolysis system and the modified reducing flame spray pyrolysis system. Adapted from [38].

By supplying the second component externally to the flame, it is possible to fabricate complex structures. For example, by using two flames, the structure of the supported metal catalyst can be finely controlled [41]. The supported noble metal catalyst comprises fine nanoparticles dispersed on a support particle. However, when synthesizing these materials by flame, it is not easy to control the structure of the support and the structure of the metal catalyst independently. Using a two-nozzle flame as shown in Figure 1.7, a flame with combustion conditions suitable for the support and a flame with combustion conditions suitable for the metal catalyst are achieved. The particles

deposited from each collide in the gas phase to obtain the final product. It is also possible to coat the particles produced by the flame by supplying shell source vapor from a separate channel from the flame [42]. Conventionally, when core-shell particles are synthesized by the gas-phase one-step synthesis method, the difference in the physicochemical properties of the two components—the core material, and the shell material—causes a difference in the precipitation rate, resulting in a core-shell structure. Therefore, the choice of precursors for this method is limited. As shown in Figure 1.8, attempts were therefore made to install a swirler directly above the flame or supply the coating components from outside the multi-tube burner. It was found that supplying the shell material in a separate channel suppressed the formation of composite oxides of the shell and core materials, and efficiently produced core-shell particles. Thus, the open flame reactor can continuously incorporate various post-treatment processes easily, and a wide variety of particle designs are possible.

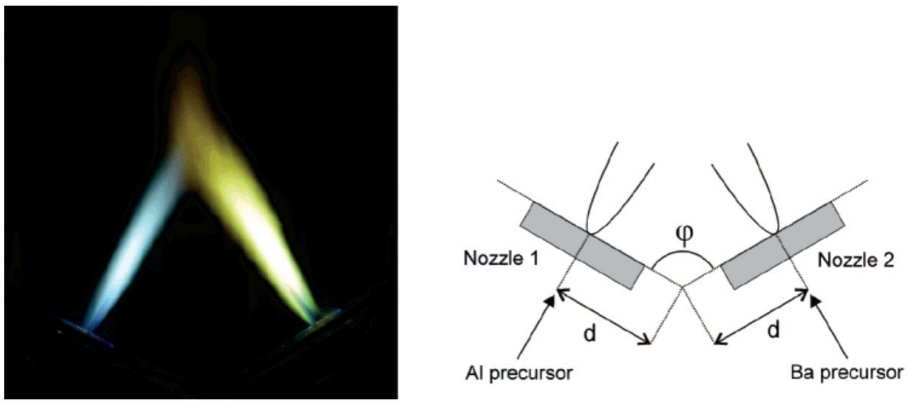

Figure 1.7: Schematic diagram of the flame spray pyrolysis system using two flame spray nozzles to produce $Pt/Ba/Al_2O_3$. Adapted from [41].

In the FASP method, macroporous particles can be synthesized by adding template material to the precursor solution because the particles can be produced in a restricted area of droplets. Osi *et al.* synthesized macroporous WO_3 using the FASP method and evaluated the effect of macropores on photocatalytic properties. As shown in Figure 1.9, the macroporous WO_3 particles synthesized using the FASP method are composed of nanoparticle aggregates, which may contribute to the enhancement of the specific surface area.

1.3.2 *Direct deposition of flame-made particles*

Fine particles are often used as multilayer films when incorporated into functional devices. However, the fabrication of multilayer films requires multiple process steps such as dispersion, coating, and drying, which leads to high costs. Therefore, a direct deposition technique for fabricating multilayer films and functional devices using a flame aerosol process have been developed.

The process of polymer nanocomposite film fabrication using the FSP method is shown in Figure 1.10. Although it is difficult to synthesize the polymer in flames be-

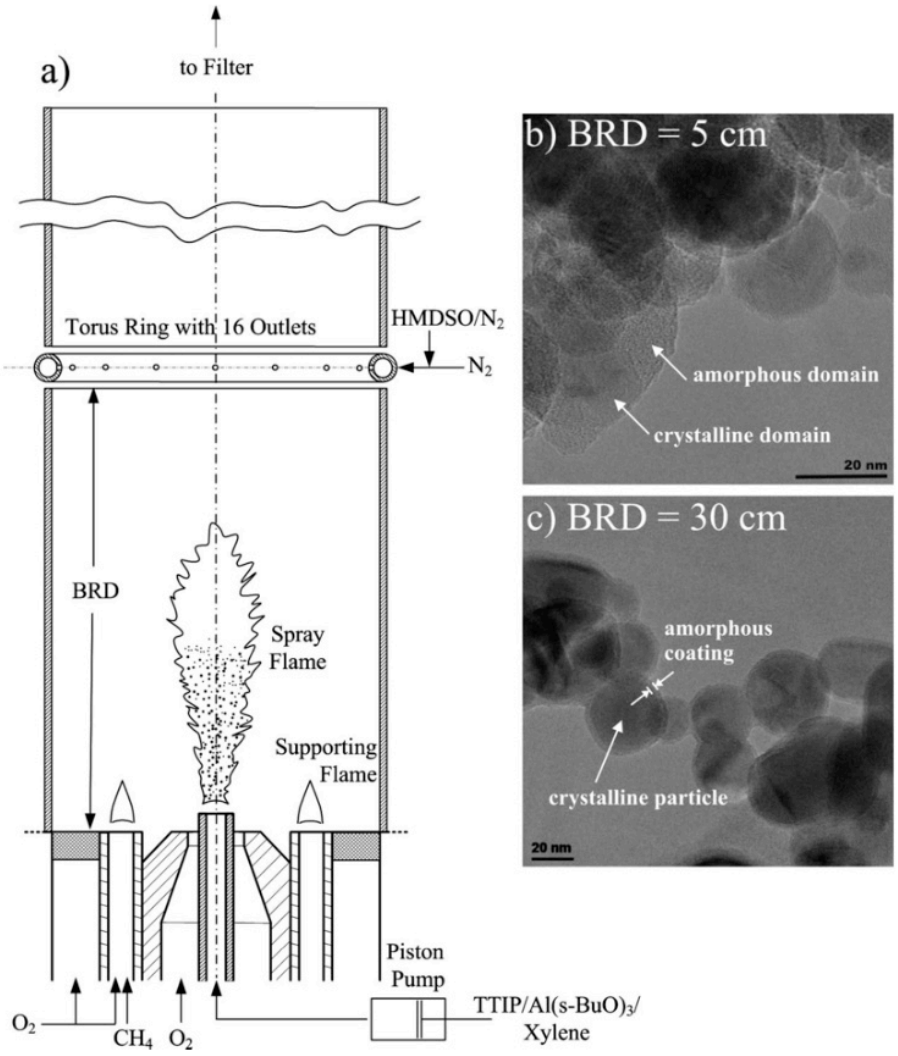

Figure 1.8: (a) flame spray pyrolysis system for in situ SiO_2 coating of flame-made TiO_2 nanoparticles. The systems produced segregated $SiO_2/Al_2O_3/TiO_2$ or SiO_2-coated Al/TiO_2 particles, respectively, at (b) 5 and (c) 30 cm burner-ring distance. Adapted from [42].

cause the flame temperature reaches more than 2000°C, polymer combustion can be prevented by spraying the polymer in the post flame zone. Blattmann and Pratsinis developed a direct deposition method by mixing flame synthesized particles and polymers in the gas phase [43]. The aerosol process is a continuous process, and the particle concentration can be varied over time, making it possible to change the particle concentration in the film. In addition, nanocomposite bridges can be fabricated using a mold. Applying the lithography technique introduces the possibility of adding more delicate functional structures.

It can be seen in Figure 1.11 that the flame synthesized SnO_2 is uniformly deposited on the sensor substrate (made of alumina) [44]. The SnO_2 produced from the spray flame is deposited on the sensor substrate by thermophoresis, forming a uniform par-

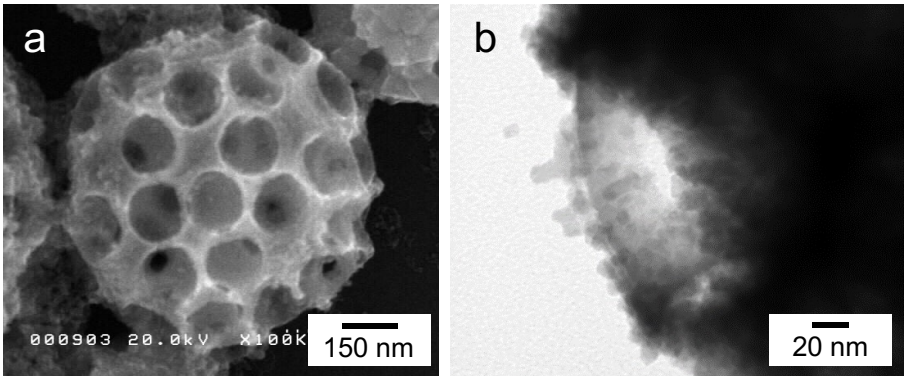

Figure 1.9: (a) SEM and (b) TEM images of FASP-made macroporous WO_3 particles.

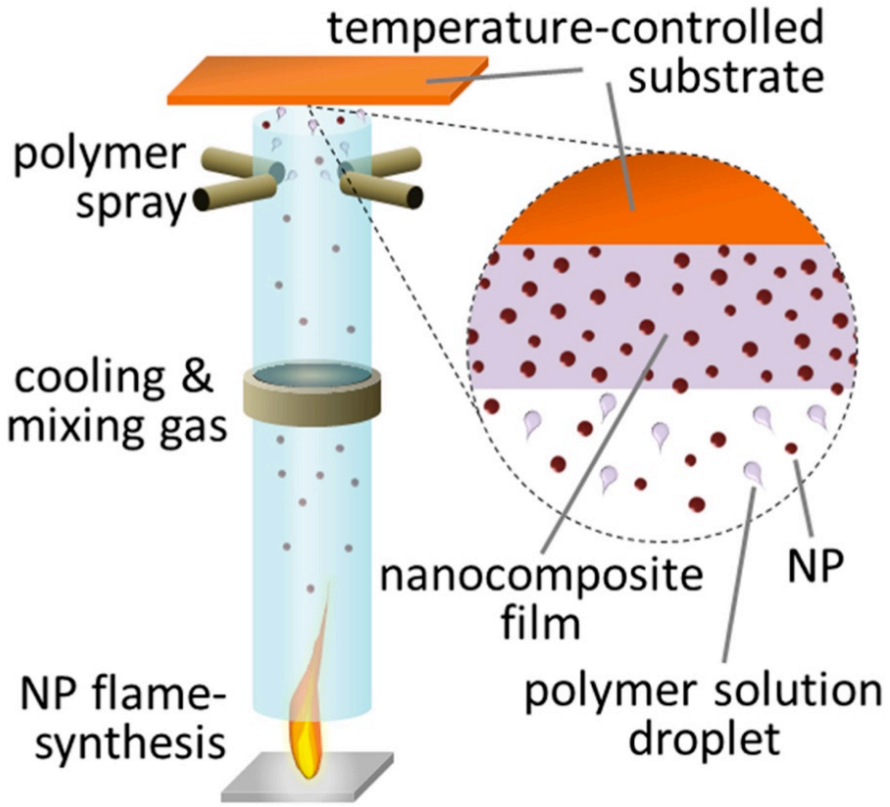

Figure 1.10: Flame spray pyrolysis system with simultaneous injection of a polymer precursor solution for single-step nanocomposite fabrication. Adapted from [43].

ticle layer. The obtained sensor showed high sensing characteristics. The deposited SnO_2 had a fine porous structure, and the film thickness could be controlled by adjusting the deposition time. Flame aerosol synthesis can be easily applied not only for the production of simple oxides such as SnO_2, but also to the doping and loading of secondary elements, making it widely applicable to direct fabrication technology for

various sensor device materials. In addition, direct particle deposition using the flame method can be achieved cleanly in a short timeframe compared with the conventional batch-type sensor fabrication method.

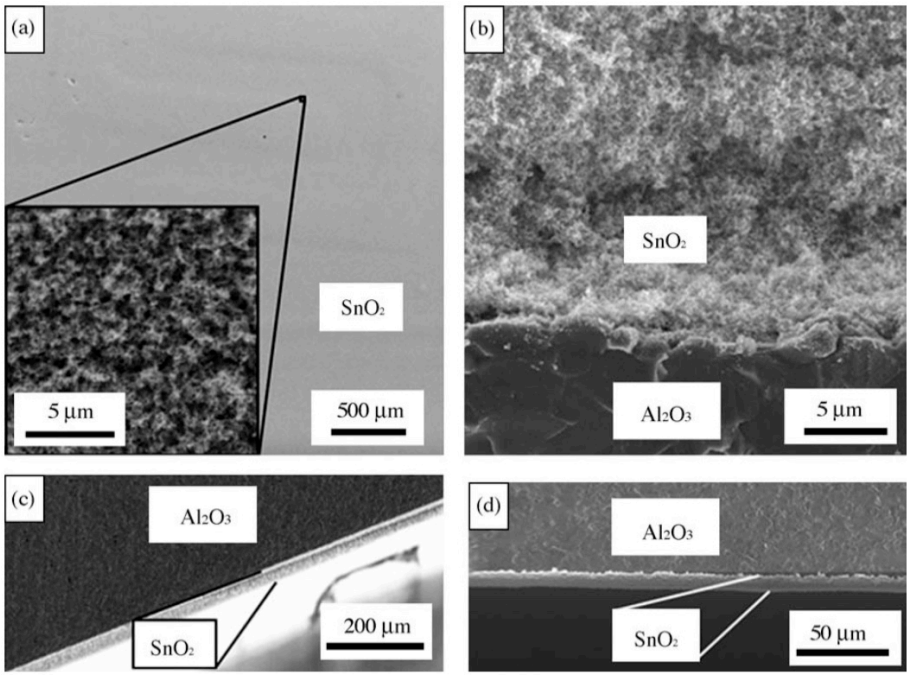

Figure 1.11: SEM images of sensor substrates showing (a) the uniformity of the sensor surface; (b) the cross sectional image; (c) the same sensor from the side; (d) a side view of a film with approximately 1/3 of the thickness. Adapted from [44].

However, one of the problems of particle layers fabricated by the direct deposition process using aerosol technology as described above, is the low mechanical stability. To improve the mechanical strength of the particle film fabricated directly by FSP, the spray flame calcination treatment was investigated without particles. The calcination process, which takes only 30–60 s, improves the mechanical stability while maintaining the porosity. However, flame annealing requires the material to be durable at high temperatures, limiting the substrates that can be used. Therefore, a technique was devised for laminating the flame-made particles deposited on the filter onto various substrates using the two-step process shown in Figure 1.12 [45]. The technique transfers the layers onto the various substrates and applies pressure during the lamination stage, which results in the reconstruction and mechanical stabilization of the nanoparticle layers. Moreover, the porosity can be adjusted according to the application. M. Gockeln *et al.* used this technique to fabricate electrodes $Li_4Ti_5O_{12}/C$ for lithium-ion batteries [21].

1.3.3 *In situ diagnostics of flame synthesis*

Various nanoparticle materials are industrially produced by flame aerosol synthesis and even direct fabrication of particle deposited film, it is therefore important to ana-

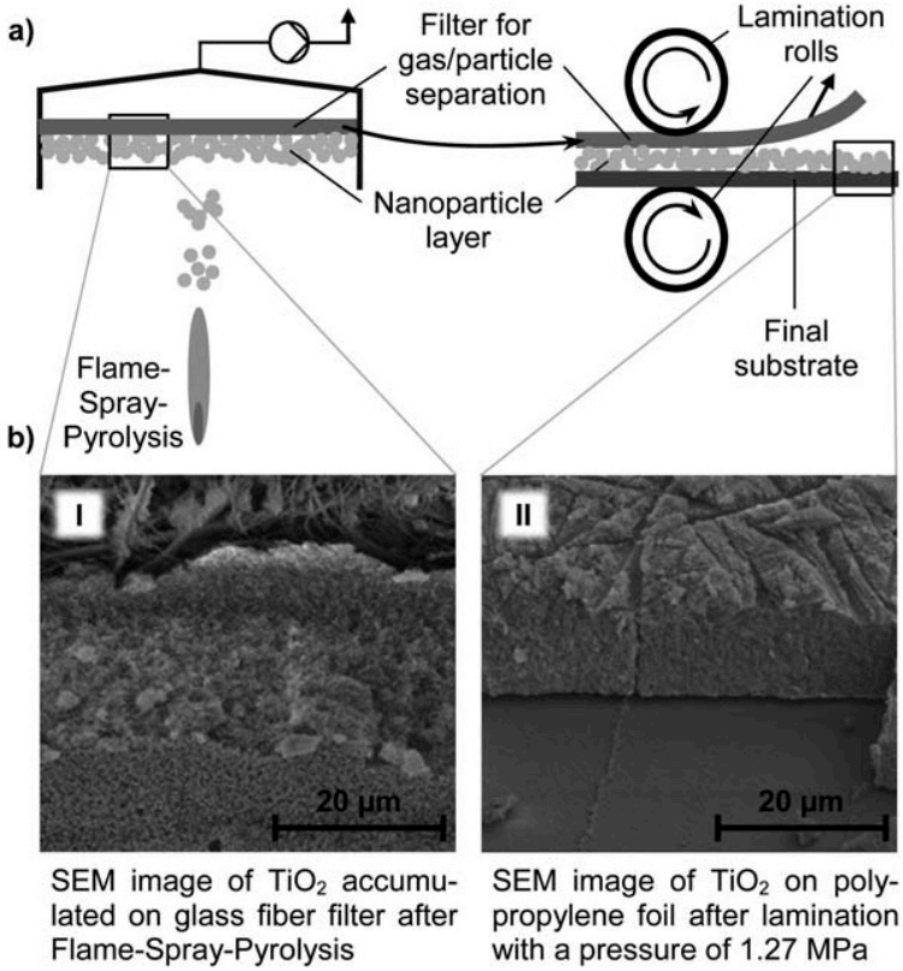

Figure 1.12: System of layer transfer to a substrate. (a) The two process steps; target particle synthesis and deposition (left) and lamination with filter removal (right) and (b) SEM images of a layer of TiO_2 nanoparticles before (I) and after (II) lamination process. Adapted from [45].

lyze the behavior of particles in flames from a scientific point of view. Understanding how the particles are generated in the flame is expected to enable precise control and more sophisticated particle synthesis. In this section, characterization methods for flame aerosol synthesis are described.

To understand the formation of particles in a flame, classical methods have been used to sample and analyze particles placed at each flame position. The most commonly used method is to deposit particles on a grid by thermophoresis and perform TEM/SEM observations. Because the thermophoretic velocity of particles in the free molecular region is independent of the particle size, it is thought that the morphology of the particles in the flame can be confirmed relatively accurately. The results obtained by this method are often used to determine the validity of particle sizes obtained by other methods. However, it should be noted that the size information ob-

tained is average information in the sweep direction of sampling. Similarly, SMPS and DMA methods have been devised for particle analysis by sampling.

The analysis of particles in a flame by sampling is a useful method that is simple and accurate. However, because this method is ex situ, online monitoring and temporal & spatial particle analysis are not possible. Therefore, an optical method for in situ diagnosis of the flame synthesis field has been developed, as shown below.

- Spontaneous Raman scattering
- Coherent anti-Stokes Raman scattering
- Fourier transform infrared emission/transmission spectroscopy
- Laser-induced fluorescence
- PIV/LPD/PDA
- Laser-induced scattering
- Raman
- Laser-induced incandescence
- Laser-induced breakdown spectroscopy

Laser-induced breakdown spectroscopy (LIBS) is a type of atomic emission spectroscopy that enables quantitative temporal and spatial analysis of flame-made particles. When a laser beam is focused on an observation target, the bound electrons in the atoms are given high energy and go through an excited state and then return to the ionized state. The free electrons produced by the ionization collide with the surrounding atoms, and more free electrons are produced, causing a breakdown and generating plasma. Subsequently, when the free electrons transition to their initial activation, each atom (molecule) emits light of a specific wavelength. Y. Zhang *et al.* succeeded in obtaining the two-dimensional distribution of the volume fraction of particles in a flame based on the phase-selective breakdown principle [46]. Using the experimental setup shown in Figure 1.13, they selectively broke down only the nanoparticles produced in the flame without ionizing the gas molecules by using a low-intensity laser and calculated the volume fractions from the emitted atomic spectra. In contrast to the sampling method, this method provides in situ information on nanoparticle formation, diffusion, and thermophores.

1.4 COMBUSTORS FOR FLAME AEROSOL SYNTHESIS

Various types of combustors have been used in the flame aerosol synthesis method. In this section, three types of burner typically used in the gas-phase combustion synthesis method are described.

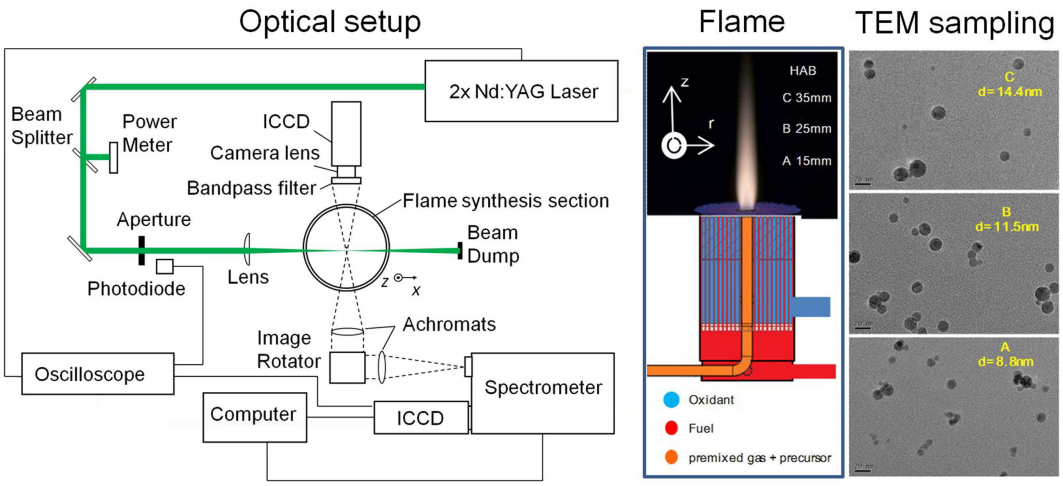

Figure 1.13: Schematic of the experimental setup for in-situ characterization of flame aerosol synthesis by laser-induced breakdown spectroscopy. Adapted from [46].

1.4.1 *Coflow diffusion flame burner*

In the coflow diffusion flame shown in Figure 1.14, the fuel and oxidizer are supplied in separate channels, thus eliminating the risk of backfire and allowing combustion over a wide range of equivalence ratios. In addition, pure oxygen is often used as the oxidizer, resulting in very high-temperature combustion gas compared with combustion in air. However, in this combustion method, the fuel and oxidizer diffuse and form a flame when they reach the combustible range. In other words, the combustion characteristics of the flame are dominated by the transport properties inherent in the material, such as the diffusion coefficients of the fuel and oxidizer. This has the disadvantage that it is challenging to control the combustion characteristics. This burner is often used for VAFS and FASP. The coflow diffusion flame has an extended high-temperature region behind the flame zone, making it difficult to control the particle properties. This combustion method is often used in practical combustors for safety reasons.

1.4.2 *Spray flame burner*

A spray flame, shown in Figure 1.15, is used in the flame spray pyrolysis (FSP) method for the combustion of flammable liquid raw materials. The raw materials are dissolved in an organic solvent, sprayed using a two-fluid nozzle, and continuously ignited using a pilot flame to form a spray flame. The raw materials vaporize and react in the flame and precipitate as particles. Because the spray flame is turbulent, it is challenging to analyze the flow, and unburned hydrocarbons may be deposited on the surface of the synthesized particles. However, the direct combustion of liquid fuel and precursor enables efficient combustion energy use. The two-fluid nozzle can process a

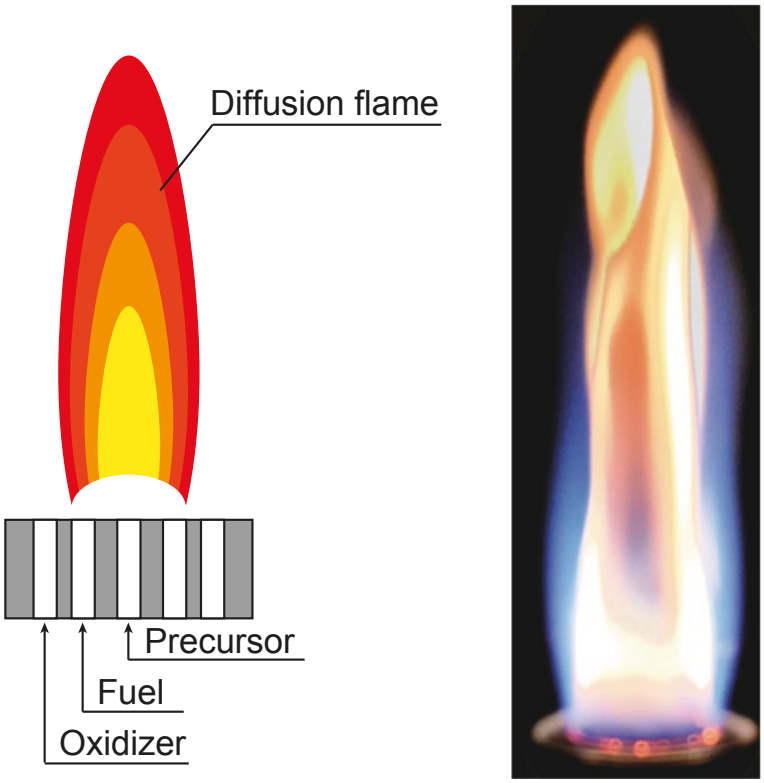

Figure 1.14: Diffusion flame.

relatively large amount of liquid; therefore, it is expected to be a safe, and inexpensive technology for fabricating functional nanoparticles and devices on an industrial scale.

1.4.3 *Flat flame burner*

The flat flame, shown in Figure 1.16, is used in the field of fundamental combustion science to elucidate the flame structure and verify combustion calculations. Diffusion flames and spray flames are used for industrial flame synthesis of fine particles. However, these flames have a large distribution of reactant concentration due to non-premixing or heterogeneity. The velocity distribution also varies greatly because turbulence is used to promote mixing and atomization. In addition, the flame structure shows significant local variation owing to irregular flame stretch in the non-uniform flow distribution, and it is not always convenient to study the chemical species produced by combustion and the effects of flames on particles in the gas phase. Therefore, a flat flame, a laminar one-dimensional flame that does not undergo flame stretch, has been used to elucidate the mechanism of particle formation in the combustion field.

1.5 TUBULAR FLAMES

A tubular flame is established when a combustible mixture is injected from the tangential direction into a cylindrical tube and ignited [47–50]. Because the tubular flame

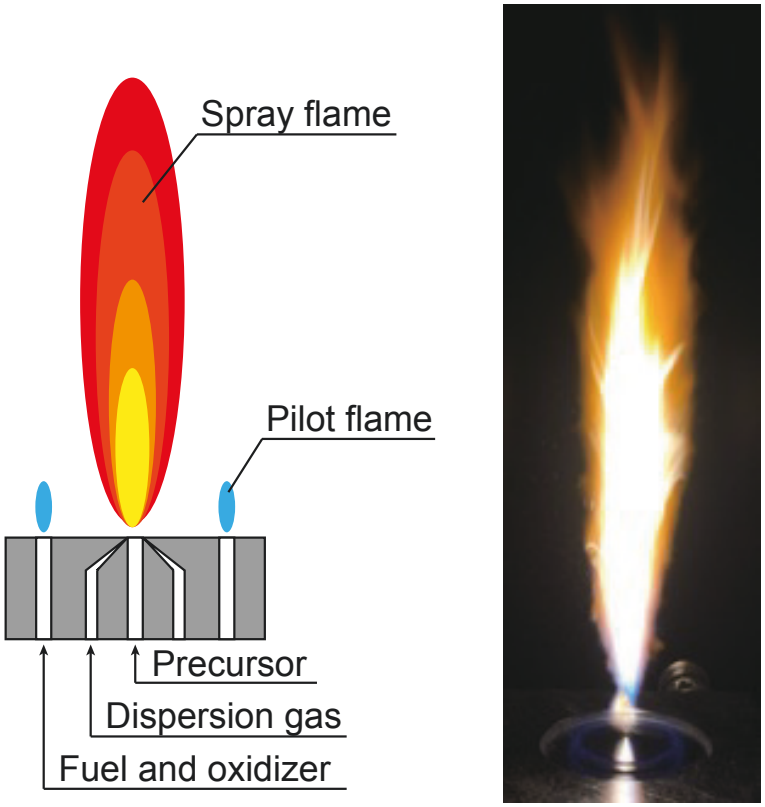

Figure 1.15: Spray flame.

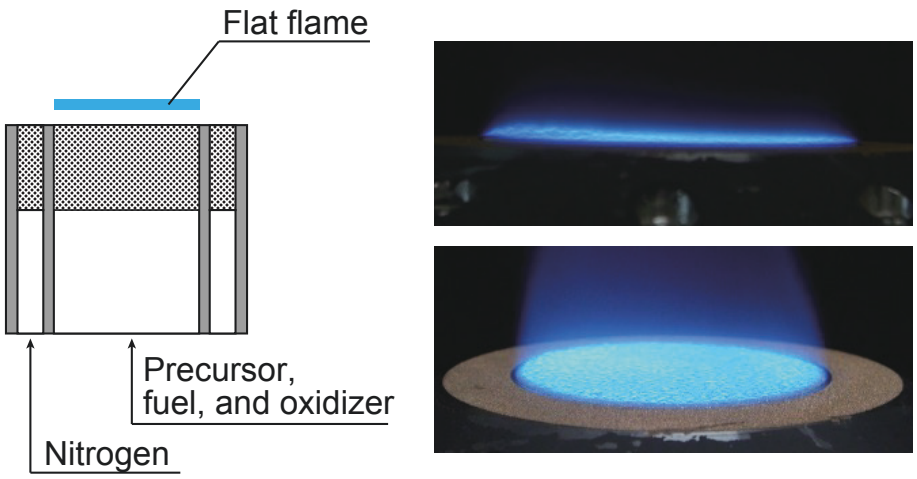

Figure 1.16: Flat flame.

is formed in a rotating stretching flow and is simultaneously affected by flame stretch and flame curvature, many theoretical and experimental studies have been conducted from the standpoint of basic combustion science. However, owing to the adiabaticity and stability achieved by the characteristic flame structure, tubular flame burners have been applied to various practical combustor applications such as fuel cell systems, burners for heating the outer cylinder of Stirling engines, and pilot flames.

The structure of a tubular flame is shown in Figure 1.17. It is aerodynamically stable according to the Rayleigh stability criterion because the flame consists of a low-density inner burnt gas region and a high-density outer unburned gas region. In addition, the unburned gas and the burned gas are laminarly stratified owing to the difference in centrifugal forces acting on them, and a continuous and uniform laminar flame front is stabilized in a tubular shape at the interface between them. The flame stabilization effect of this stratification is exceptionally high, and flame extinction due to stretch has not yet been confirmed in a tubular flame.

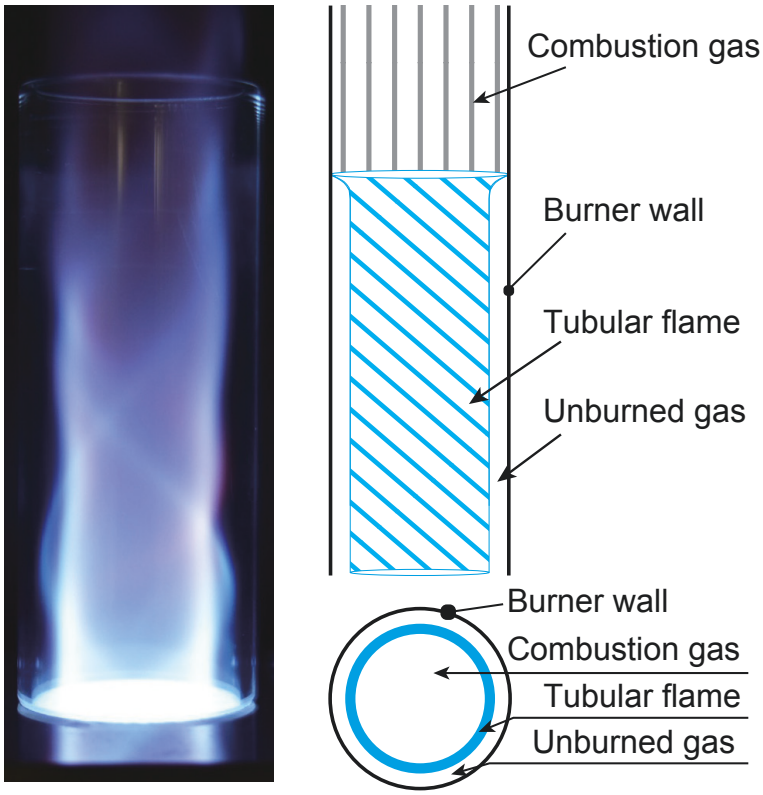

Figure 1.17: The structure of tubular flame. Adapted from [50].

Figure 1.18a shows the temperature distribution of a methane/air tubular flame. r = 0 mm is the center of the tube, and r = 13 mm is the position of the tube wall. Here, the equivalence ratio ϕ is the actual fuel-air ratio normalized by the theoretical fuel-air mixing ratio. In a tubular flame, the temperature gradient at the center of the tube is zero owing to the symmetry of the temperature distribution. The heat loss due to heat conduction can be almost negligible. By considering the radiation loss of the hot gas, the attained temperature in the combustion gas region of the tubular flame can be easily predicted and controlled from the equilibrium calculation of the adiabatic flame temperature. From the stable combustion range shown in Figure 1.18b, it can be seen that tubular flames are formed close to the flammability limit of the methane/air mixture determined by standard methods [51]. The ability to form a tubular flame without it blowing out over a wide range of flow rates and equivalence ratios not only improves the stability of the equipment but also makes it possible to widely adjust

various parameters such as the composition of the combustion gas and the residence time in the burner, which is useful in studying the effects on the synthesized particles.

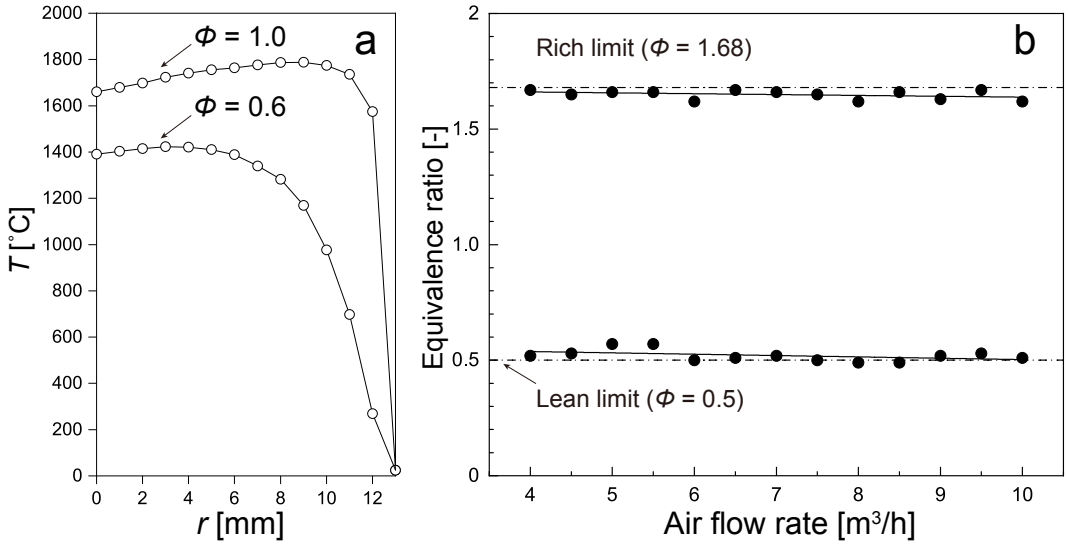

Figure 1.18: The characteristics of tubular flames. Adapted from [50].

1.6 OBJECTIVES AND OUTLINE OF THE DISSERTATION

In this dissertation, we aimed to develop a particle synthesis system with the following features as a next-generation flame aerosol synthesis method, ensuring that the combustion process was strictly controlled and the global environment was considered.

1. Controllable flame temperature
2. Controllable atmosphere
3. High combustion efficiency
4. Fuel diversity
5. Simple structure

A tubular flame burner was designed as a particle synthesis reaction field to fulfill these conditions. The combustion characteristics of the tubular flame burner for particle synthesis were investigated, and the effects of various parameters on the synthesized particles were evaluated. In addition, a tubular flame burner incorporating a two-fluid nozzle was developed for use with a wide variety of raw materials and fuels.

In Chapter 2, the synthesis of tungsten oxide nanoparticles was demonstrated using a newly developed tubular flame burner for particle synthesis. The precursor droplets generated by the ultrasonic atomizer were transported by the carrier gas to the tubular flame formed by methane/air and burned. The tubular flame had high thermal stability, and the heat loss due to heat conduction was almost negligible, so the temperature

achieved was high. Therefore, the tungsten oxide was gasified at the high temperature of the tubular flame, and the nanoparticles were obtained by renucleation from the gaseous state in the gas phase. For comparison, a synthesis test using a conventional Bunsen burner produced coarse tungsten oxide particles, suggesting a lack of energy. It was found that the combustion energy could be used more efficiently by applying tubular flame combustion.

In Chapter 3, the synthesis of metallic tungsten nanoparticles was conducted by controlling the composition of the combustion gas and creating a reducing atmosphere in the reaction field. Because of the high stability of the tubular flame, the stable combustion range was wide, and combustion was enabled in a wide range of fuel concentrations. The concentrations of CO and O_2 at each equivalence ratio were measured. It was found that an extremely low oxygen concentration and a high CO concentration could be achieved by increasing the equivalence ratio above 1, thus providing a reducing atmosphere for the formation of metal particles. When precursor droplets were burned in this reducing atmosphere, it was found that the degree of oxidation of tungsten oxide decreased with an increase in the equivalence ratio, i.e., with an increase in the concentration of reducing gas. It was also found that the tungsten metal crystals were precipitated in a single phase by increasing the residence time of the particles in the flame.

In Chapter 4, a tubular flame burner with a two-fluid nozzle was designed to use flammable liquid solvents as precursors. Ethanol was atomized by the two-fluid nozzle and fed into the tubular flame from the axial direction, enabling stable combustion. The optimum conditions for the tubular flame for liquid fuel spraying were determined by direct observation of the flame and spectral analysis of chemiluminescence.

Chapter 5 presents a summary of all topics and future prospects.

2

TUBULAR FLAME COMBUSTION FOR NANOPARTICLE PRODUCTION

ABSTRACT

Requirements for nanoparticle processing based on energy and cost-effective technologies have increased in recent years. Flame synthesis is widely used on an industrial scale and is superior to gas phase one-step processes for producing nanoparticles; however, further improvements are required from the viewpoint of energy efficiency. In this chapter†, we present a new aerodynamically stable nanoparticle processing method with extremely low energy losses, based on the use of a tubular flame. The developed tubular flame apparatus is inexpensive and simple to set up, allowing for a uniform and high temperature field with a high energy efficiency. Consequently, highly crystalline and uniform WO_3 nanoparticles were successfully synthesized with a high production rate. The simple and energy-effective process proposed in this paper has potential for application to various types of functional nanoparticle production.

† published in part in *Ind. Eng. Chem. Res.*, 58, 7193-7199, 2019.

2.1 INTRODUCTION

Nanomaterials with controlled structures, sizes, and morphologies are widely used as functional materials in many fields [1, 52–54]. Energy efficient and environmentally friendly processes are required for nanoparticle synthesis within a sustainable society.

Routes for manufacturing nanoparticles can be classified into top-down and bottom-up processes. In general, bottom-up processes are used to efficiently produce uniform and homogeneous nanoparticles. Among various bottom-up processes, aerosol processes involve syntheses where the main reactions occur in the gas phase [1, 52]. Such processes are often applied on an industrial scale. Flame (assisted) spray pyrolysis [F(A)SP] is a widely used aerosol process for producing single- and multi-component nanoparticles with high purity in a single step [6, 7] based on various types of flame systems, such as a Bunsen flame [55, 56], co-flow diffusion flame [31, 32, 57–62], spray flame [63, 64], and flat flame [65, 66]. Although the flame types commonly used for F(A)SP are available with inexpensive and simple set ups, the energy efficiency of combustion should also be considered. Owing to the structure of these flames, energy is lost from the system, for example, in the form of radiation. It is also difficult to fully understand the particle formation mechanisms in flames owing to the inhomogeneous temperature distribution and impracticability of obtaining an adiabatic flame temperature.

Tubular flame has been extensively studied from a fundamental viewpoint over the past three decades [47–49]. The structure of this flame gives a symmetrical homogeneous temperature distribution and the conductive heat loss from the flame is negligible. Thus, it is possible to efficiently use its combustion energy, which is intrinsic to the flame, for material production. Furthermore, the flame consists of a low-density inner burnt gas region and a high-density outer unburned gas region (see Figure A.1 in Appendix A). Therefore, according to the Rayleigh stability criterion [67], the flame is aerodynamically stable when it is formed in a rotating vortex flow. Because the shape of a tubular flame is geometrically well controlled, it can be incorporated in-line with various processes.

Figure 2.1 shows a comparison between Bunsen and tubular flames. In a Bunsen flame, the temperature rises near the flame front where the combustion reactions occur, but then decreases upward along the axial direction owing to energy losses. In addition, the temperature inside the flame, through which particles and precursor pass, is low because unburned gas is present. Whereas in the tubular flame, the unburned cold gas covers the outer periphery of the hot burned gas. Hence, the burner wall is maintained at low temperature and undamaged, thus enabling long term operation. This is important for practical applications. Furthermore, owing to its high thermal insulation properties, a high temperature region is maintained homogeneously inside the tubular flame through which the particles and precursor pass through. The flat profile itself affects to the burned gas temperature. The flat profile indicates that heat loss to the downstream region can be neglected and that almost adiabatic condition can be achieved in the burned gas region. In other words, we have the possibility to use combustion energy effectively without any heat losses. As described above, a tubular flame has excellent heat insulating properties, a convenient shape for application

to various process, unique combustion characteristics, and is attractive from the viewpoint of engineering and practical applications. However, there have been no reports on the synthesis of particle materials by tubular flame methods.

We investigated the preparation of tungsten oxide (WO_3) particles using a tubular flame for the first time and developed a new process for nanoparticle production. In the case of WO_3, the flat profile of temperature is indeed important because its oxidation state is very sensitive to temperature. So far, WO_3 particles have been prepared by FSP [68,69], FASP [59], and spray pyrolysis methods [70,71]. Righettoni et al. reported a method to synthesize pure and Si-doped WO_3 nanoparticles films onto Al_2O_3 substrates using a FSP reactor in combination with a water-cooled substrate holder. Osi et al. reported a synthesis process of Pt-loaded submicrometer-sized WO_3 particles by FASP method with methane/oxygen combustion. Although adiabatic flame temperature of this combustion system could attain around 3000 K, nanometer-sized particles could not be produced. It indicates large heat losses behind the flame [62]. Hence, the tubular flame combustion has a potential to enable nanoparticle production with high yield and higher energy efficiency. The as-prepared powders were characterized by X-ray diffraction and scanning electron microscope (SEM) and transmission electron microscope (TEM) imaging to evaluate their sizes, morphologies, and crystal structures.

2.2 EXPERIMENTAL

2.2.1 *Particle synthesis*

The experimental setup used to synthesize particles, based1 on a tubular flame, is shown in Figure 2.2(a). The setup consisted of three sections, namely, a spray generator, tubular flame burner, and particle collector (bag filter). The spray generator section consisted of an ultrasonic spray nebulizer equipped with a 1.75 MHz resonator (NE-U17, Omron Healthcare Co., Ltd., Tokyo, Japan). The droplets were transported into a tubular flame burner by a stream of argon (Ar) gas, and the flow rate (Q_C) was varied from 0.1 to 0.5 m^3/h. Methane (CH_4) was used as the fuel gas (0.1 m^3/h). Compressed air was fed into the tubular flame burner using a compressor. Temperature profiles were observed using a silica-coated Pt/Pt-13% Rh thermocouple with a wire diameter of 0.2 mm. A solution of ammonium tungstate pentahydrate [ATP, $(NH_4)_{10}(W_{12}O_{41})\cdot 5\,H_2O$; purity 88–90%; Kanto Chemical Co., Inc., Tokyo, Japan] in ultrapure water with a concentration of 10 mmol/L was used as the main precursor.

2.2.2 *Tubular flame burner*

Tubular flame can be established when the fuel and oxidizer (or their mixture) is tangentially injected into a cylindrical tube. There is one key parameter called "swirl number", which is the characteristic of swirl intensity [47,72]. The swirl number of the burner is desired to be over 0.6 to form a strong swirl flow in the burner. Figure 2.2(b) shows a tubular flame burner used in this research. The burner, made of duralumin,

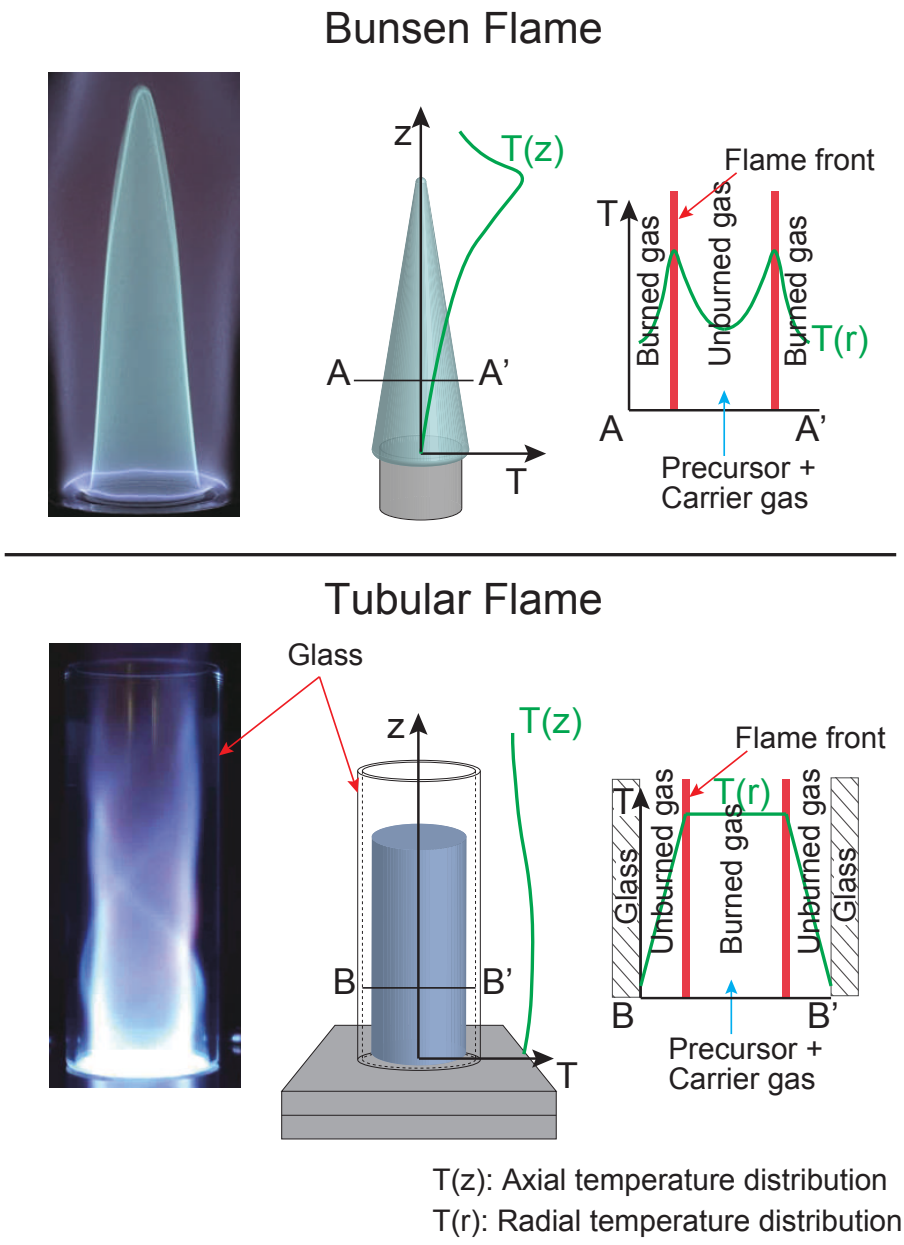

Figure 2.1: Bunsen flame (upper) and tubular flame (lower).

consisted of two tangential inlet slits and a downstream quartz tube (100 mm). A combustible mixture of gases (CH_4/Air) was fed tangentially from the inlet slit into the burner. The precursor droplets were fed into the inner hot gas region of the tubular flame from the bottom by Ar. Detailed information on the tubular flame burner setup (e.g., quartz tube dimensions, mounting details, etc.) is provided in Figure A.2 in Appendix A.

2.2.3 *Characterizations*

The SEM (S-5200, Hitachi, Tokyo, Japan; operated at 20 kV) and TEM (JEM-3000F, JEOL Ltd., Tokyo, Japan; operated at 297 kV) were used to observe the sizes, morphologies, and crystal structures of the as-synthesized particles. The crystal structures of the prepared particles were also investigated using an X-ray diffractometer (XRD; D2 PHASER, 40 kV and 30 mA, Bruker Corp., USA).

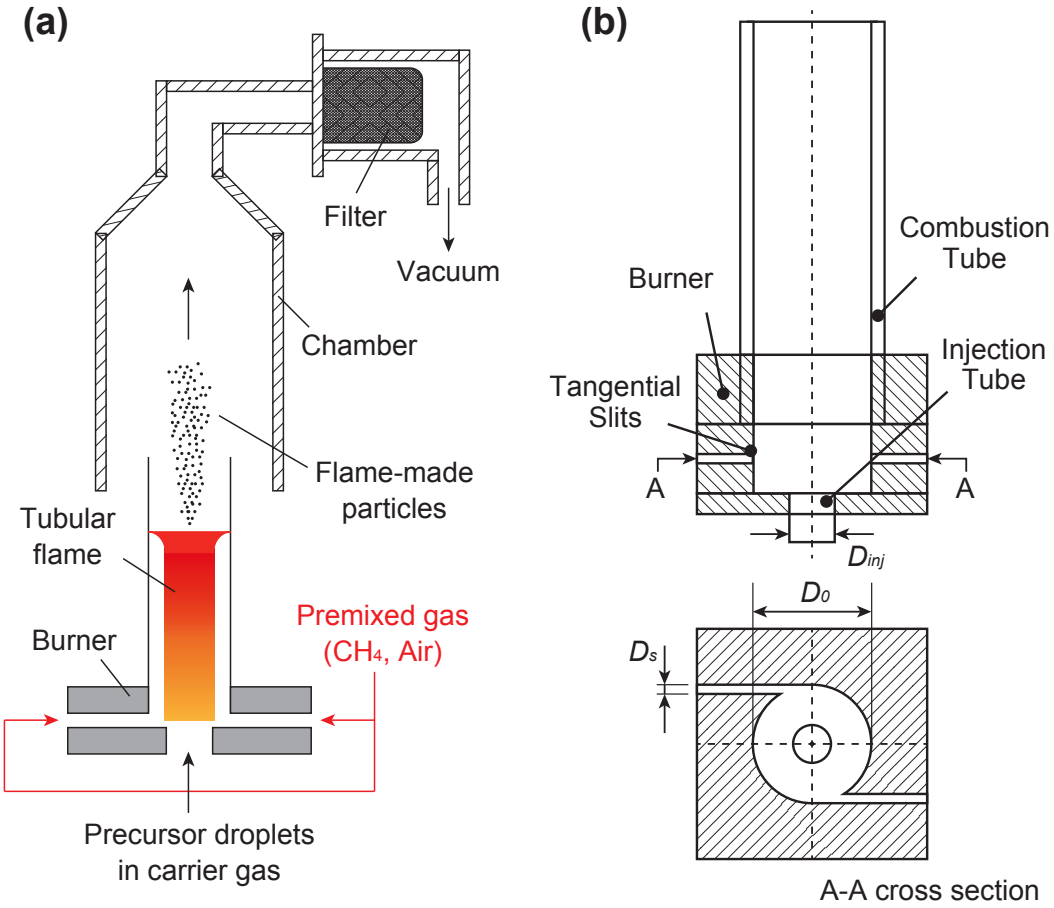

Figure 2.2: Experimental setup (a) and tubular flame burner (b).

2.3 RESULTS AND DISCUSSIONS

There are many parameters in tubular flame combustion that affect the properties of the synthesized particles, for example, the gas flow rates for both the carrier and premixed gases, types of fuel and oxidizer, ratio of fuel/oxidizer, and the diameter of the tubular flame. Here we synthesized WO_3 particles at various carrier gas (Ar) flow rates as a first step towards tubular flame synthesis.

2.3.1 *Effect of carrier gas flow rate on morphology and crystallinity of WO_3 particles*

Figure 2.3 shows XRD patterns of the as-synthesized particles formed at various carrier gas flow rates (Q_C = 0.05–0.5 m^3/h) with a fixed premix gas flow rate. The XRD patterns suggested that the prepared particles had two types of WO_3 crystal structures: monoclinic (COD no. 01-072-0677) and hexagonal (COD no. 01-075-2187). The monoclinic structure was formed when Q_C at 0.05–0.3 m^3/h, whereas particles with both monoclinic and hexagonal structures were formed when Q_C at 0.4 and 0.5 m^3/h. The presence of hexagonal structures indicates that the supplied energy was insufficient to produce stable and pure monoclinic structures. We attribute this result to the low synthesis temperature and short residence time, which resulted because as Q_C was increased, the maximum synthesis temperature decreased (see temperature distribution of tubular flame in Figure A.3 of Appendix A) and the residence time also decreased. To investigate the morphology of the tubular flame-synthesized particles, we conducted SEM observations of WO_3 particles synthesized at Q_C = 0.05–0.5 m^3/h, and the results are shown in Figure 2.4. At Q_C = 0.5 m^3/h, the obtained particles were mainly of sub-micrometer size, over 400 nm with a few nanoparticles less than 50 nm. At Q_C = 0.15–0.4 m^3/h, the proportion of submicrometer-sized particles decreased, and nanoparticles with sizes less than 50 nm started to form. At Q_C = 0.05–0.1 m^3/h, the submicrometer-sized particles disappeared completely and only nanoparticles were obtained. These results show that sufficient energy was supplied to completely segregate submicrometer-sized particles at low carrier gas flow rates.

The morphology of WO_3 nanoparticles synthesized at Q_C = 0.1 m^3/h was observed further through TEM observations, as depicted in Figure 2.5 (TEM images at other flow rates are shown in Figure A.4 in Appendix A). In a low magnification image (Figure 2.5a), nanoparticles with a relatively high dispersion were observed and no submicrometer-sized particles were observed. As shown in Figure 2.5b, necking of the nanoparticles was observed and the primary particle sizes were in the range of 5–20 nm. The corresponding HR-TEM image (Figure 2.5c) confirmed that the prepared nanoparticles had a uniform orientation with a lattice spacing at 0.34 nm. This result is consistent with the d spacing of the (002) planes of the monoclinic WO_3 crystal structure.

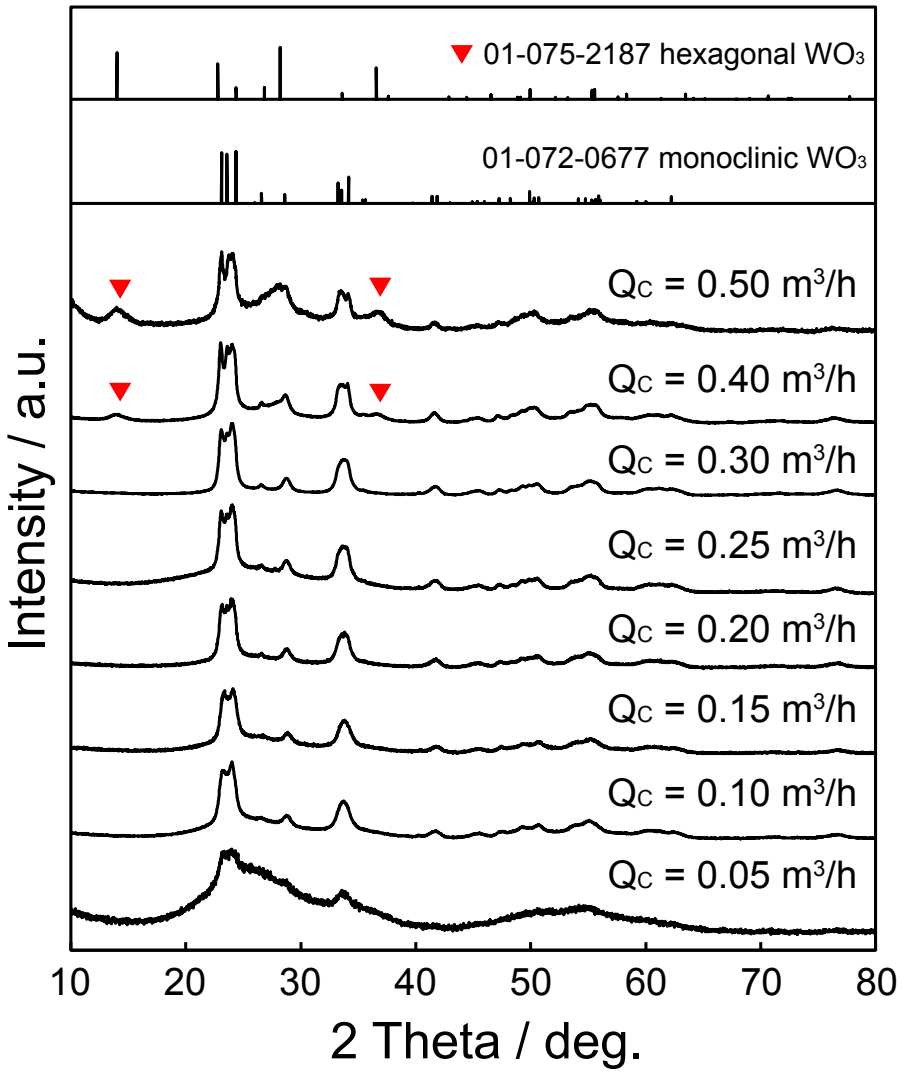

Figure 2.3: XRD patterns of WO_3 particles prepared via the tubular flame method at different carrier gas flow rates.

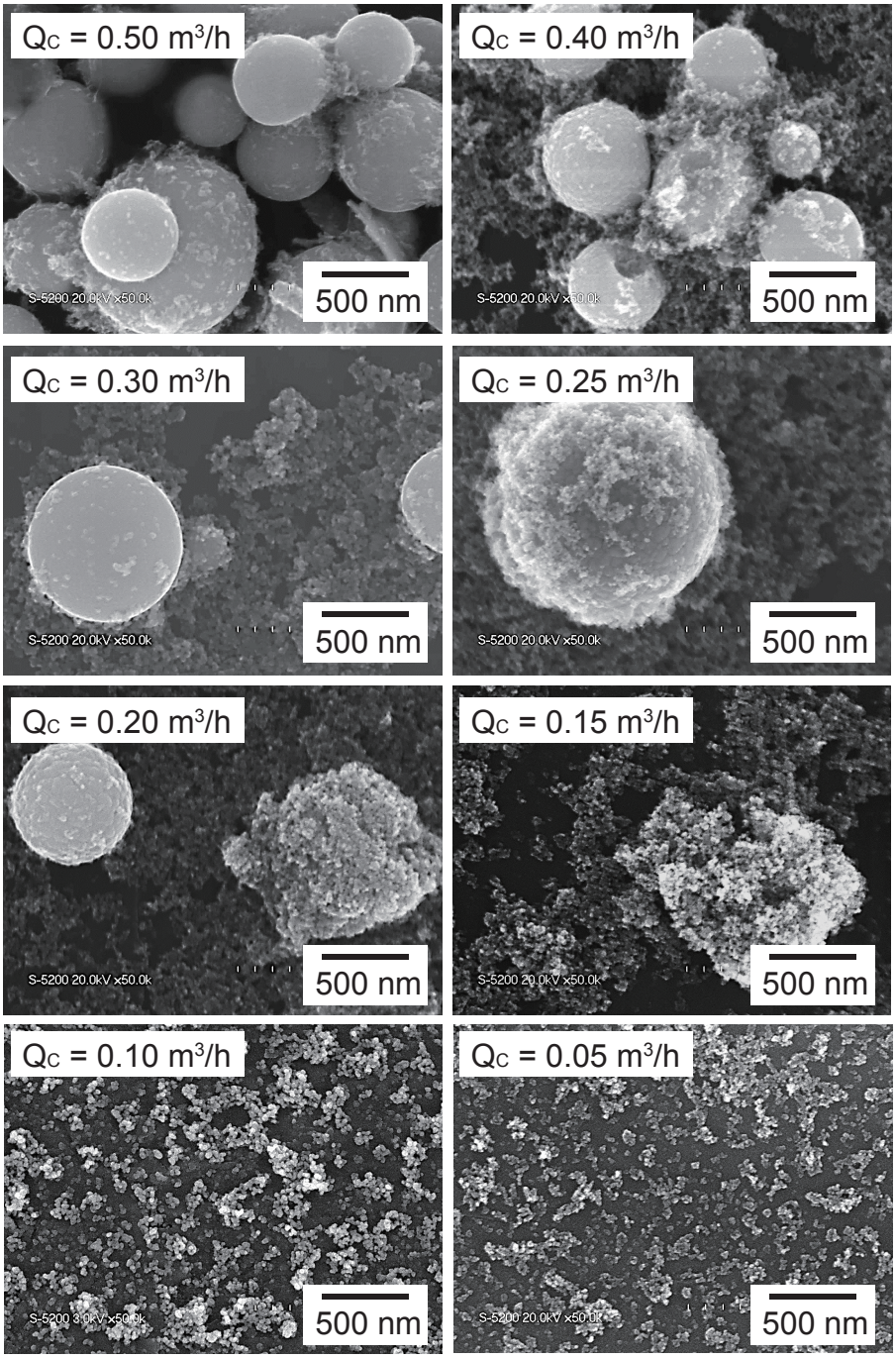

Figure 2.4: SEM images of WO_3 particles prepared in tubular flame at different carrier gas flow rates.

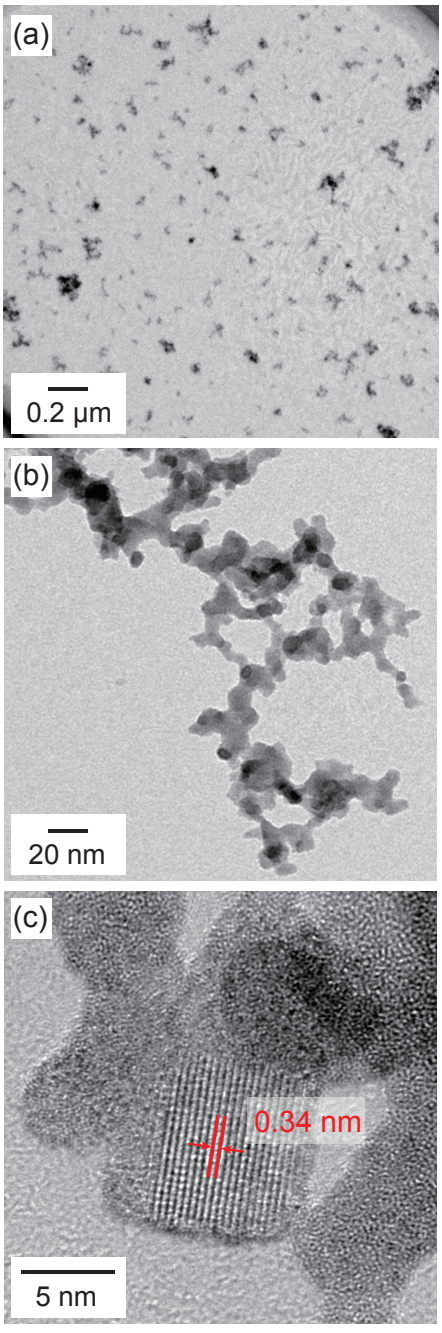

Figure 2.5: TEM images of WO_3 nanoparticles prepared at Q_C = 0.1 m^3/h.

2.3.2 *Formation mechanisms of WO_3 nanoparticles by the tubular flame method*

We propose mechanisms for the WO_3 nanoparticle formation in the tubular flame, as illustrated in Figure 2.6. According to previous studies on the synthesis of WO_3 particles in the gas phase [32,62], droplets containing ATP were sprayed into the tubular flame and underwent reactions to form, in sequence: ATP particles → intermediate WO_3 particles → WO_3 particles after the solvent evaporation. The morphology and crystal phase of the particles changed depending on the Q_C [70,73].

At a high Q_C (0.5 m^3/h), after the nebulized droplets containing the ATP precursor were introduced into the flame zone, solvent evaporation and thermal decomposition occurred instantaneously, and submicrometer-sized WO_3 particles formed. As Q_C decreased (0.4 to 0.15 m^3/h), the particle residence time inside the flame increased, indicating a longer exposure of energy for the submicrometer-sized particles, which subsequently partially vaporized resulting in the formation of WO_3 nuclei. These nuclei grew to form nanoparticles through a crystal growth process as they moved inside the glass flame reactor. As a result, submicrometer-sized WO_3 particles were produced together with nanoparticles. At Q_C = 0.4–0.5 m^3/h, the obtained particles had a hexagonal WO_3 crystal structure, which is a metastable phase, indicating that insufficient energy was supplied. When Q_C was further decreased (0.05–0.1 m^3/h), the submicrometer-sized WO_3 particles completely vaporized. Consequently, the submicrometer-sized particles disappeared and WO_3 nanoparticles were produced [74,75].

The radial temperatures at a point 50 mm from the bottom of the burner for each Q_C are listed in Table 2.1. Detailed information on temperature distribution is available in Figure A.3 (see Appendix A). To minimize the insertion effect, a thin 200 μm silica-coated R-type thermocouple was used for the measurement. Corrections for thermometric errors owing to radiation were applied to the results. The emissivity value was obtained by applying 0.22 [76] for the coated platinum thermocouple value, and the physical property values of the combustion gas were obtained by applying the estimation formula given by the gas molecular kinetics [77]. For the combustion gas velocity, the average axial velocity obtained from the premixed gas flow rate and the burner cross section was used. The temperature at a point where the precursor passed through the tubular flame (r = 0, 1, 2, 3 mm) tended to decrease as Q_C increased. This is simply because when Q_C is high, the amount of gas flowing into the tubular flame increased such that the supplied energy was consumed heating the Ar gas and the precursor droplets. As the temperature in the system decreased, vaporization of submicrometer-sized particles was incomplete, resulting in the formation of both submicrometer- and nanometer-sized particles. Furthermore, for the swirl-type tubular flame used in this research, the carrier gas that was fed from the bottom of the burner swirled along with the surrounding fluid (combustion gas) entering from the sides of the burner. Thus, the hot surrounding fluid without particles mixed rigorously with the cold carrier gas containing the particles, which increased the heat transfer area between these two fluids [78]. In addition, the swirl intensity was high under the operation conditions used in this study. Therefore, not only the heat transfer, but rather the mixing itself was also improved owing to the high turbulence in the tan-

gential direction [78]. When Q_C was low, the residence time and the heat transfer area increased as the carrier gases mixed, and the proportion of combustion gas increased. Thus, a large amount of energy was supplied to the particles, resulting in complete vaporization of the submicrometer-sized particles.

Table 2.1: Temperature in tubular flame at different carrier gas flow rates (Z = 50 mm).

Q_C [m^3/h]	$T_{r=0}$ [°C]	$T_{r=1}$ [°C]	$T_{r=2}$ [°C]	$T_{r=3}$ [°C]
0.1	1276	1314	1335	1339
0.2	1251	1299	1348	1360
0.25	1178	1214	1264	1355
0.4	1032	1057	1065	1076
0.5	878	924	947	963

2.3.3 *Comparison between tubular flame-made WO_3 and premixed Bunsen flame-made WO_3*

To compare the particles synthesized via a tubular flame and premixed conventional burner, WO_3 particles were also synthesized with a premixed Bunsen burner (see Figure A.5 in Appendix A) under the same conditions as the flame burner setup, i.e., a CH_4 flow rate at 0.1 m^3/h, air flow rate of 0.95 m^3/h, and carrier gas flow rate of 0.1 m^3/h. The XRD patterns of both particles indicated monoclinic phase (see Figure A.6 in Appendix A). Figure 2.7 shows SEM images of the Bunsen flame-made WO_3 particles and tubular flame-made WO_3 particles. As shown in Figure 2.7a, the particles range from micrometer- to nanometer size. Because there was no mixing of gases and considerable heat loss from the system, insufficient energy was supplied to the WO_3 particles. Particle size distribution of these particles is shown in Figure 2.7c. It shows that Bunsen flame produced WO_3 particles in a bimodal size distribution. Whereas, tubular flame-made WO_3 particles have a narrow particle size distribution (d_{av} = 25.1 nm, σ_g = 1.21). Table 2.2 summarizes the methane, air, and carrier gas flow rate settings and the corresponding production yields, average particle sizes (d_{av}), geometric standard deviations (σ_g), and crystal structures. The successful production of fine and monodispersed WO_3 nanoparticles indicates that the tubular flame combustion is a promising approach as an energy efficient nanoparticle production. Moreover, several techniques, such as pilot flame, bluff body, opposing jet, and recess walls are commonly used to stabilize flames [78–81], including the Bunsen burner method. However, in the case of a tubular flame burner, it is possible for a large amount of gas to combust without using these stabilizing techniques owing to the inherent stability of the flame. This is a considerable advantage of tubular flame reactors for practical applications in cost and energy effective production of nanoparticles.

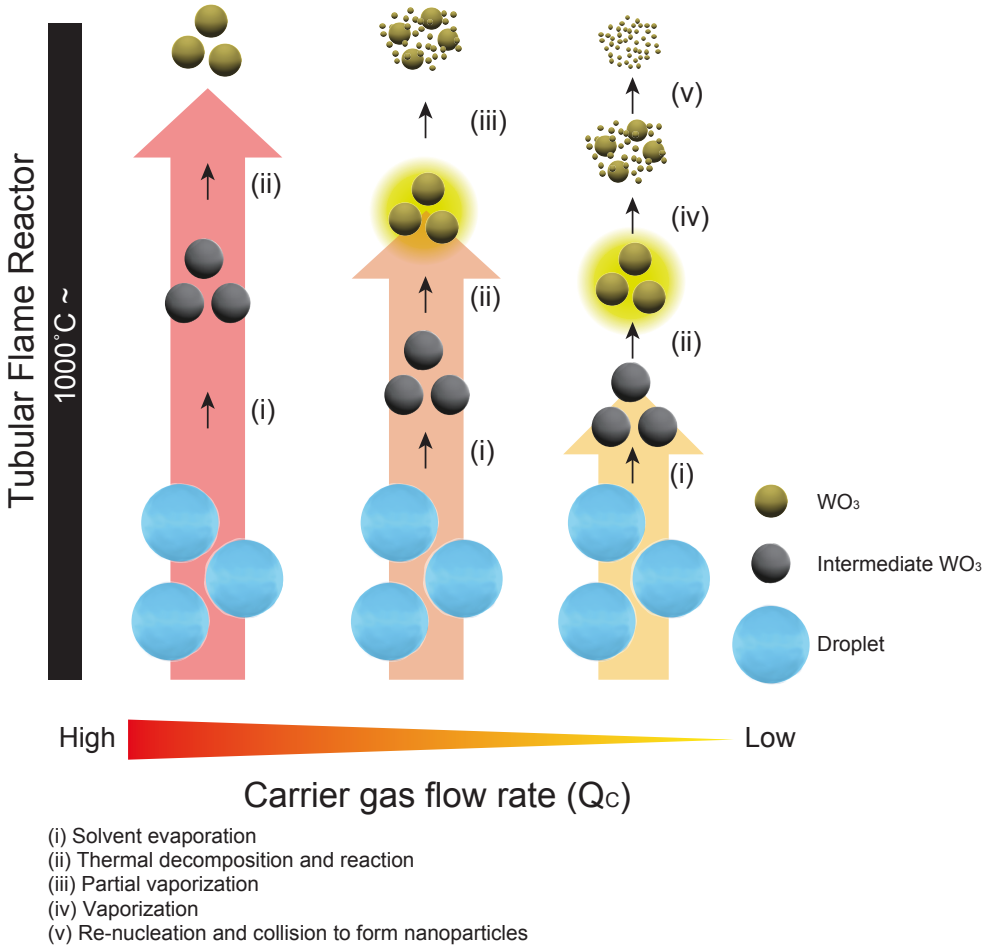

Figure 2.6: Schematic illustration showing mechanisms for formation of WO_3 particles in tubular flame at different carrier gas flow rates.

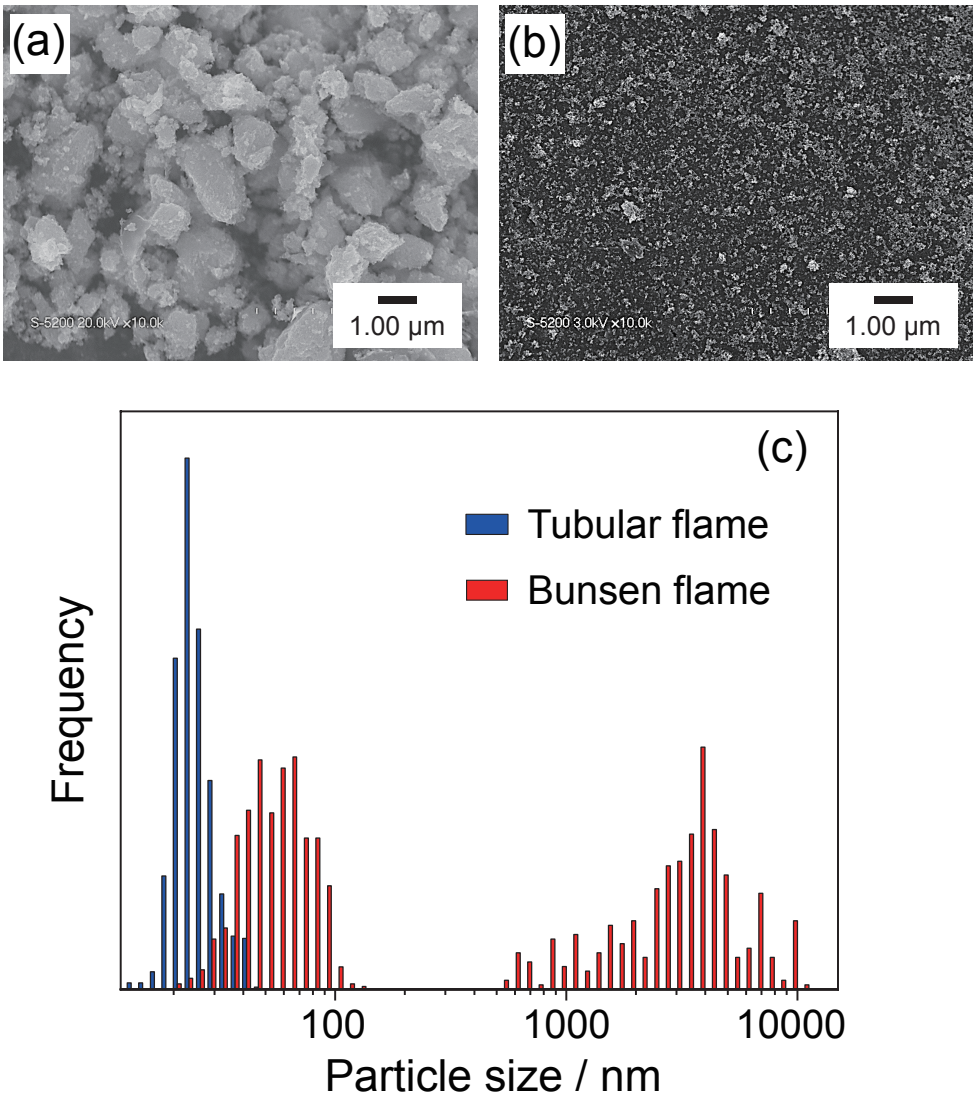

Figure 2.7: SEM images of WO_3 particles prepared with the use of (a) Bunsen flame, (b) tubular flame and (c) particle size distribution of WO_3 particles prepared in tubular and Bunsen flames.

Table 2.2: Production Yields, Average Particle Sizes (d_{av}), Geometric Standard Deviations (σ_g), and Crystal Structure of the Particles Prepared in Tubular- and Bunsen Flame Reactors.

	Gas flow rate [m³/h]							
	CH_4	Air	Carrier (Ar)	Prod. yield [%]	d_{av} [nm]	σ_g [-]	Crystal structure	Size distribution
Tubular flame made	0.1	0.95	0.1	12.14	25.1	1.21	monoclinic	Monodisperse
Bunsen flame made nanometer sized	0.1	0.95	0.1	6.22	55.6	1.39	monoclinic	Bimodal
micrometer sized					2926.5	1.91		

2.4 CONCLUSIONS

A tubular flame was used to synthesize WO_3 nanoparticles at various carrier gas flow rates as the first step in our research toward development of novel nanoparticle processing. The size of the tubular flame-made WO_3 particles increased in proportion to the carrier gas flow rate. Because the conductive heat losses from the tubular flame were negligible and the flame was aerodynamically stable, our new approach to synthesizing nanoparticle shows great promise for practical application to nanoparticle production based on new energy-efficient flame method.

AKNOWLEDGEMENTS

This work was supported by JSPS KAKENHI Grant Number 26709061 and 16K13642. This work was partly supported by the Center for Functional Nano Oxide at Hiroshima University. The authors thank Dr. Makoto Maeda of the Natural Science Center for Basic Research and Development (N-BARD) at Hiroshima University for TEM observations and discussion.

3

UTILIZATION OF INNER REDUCING GAS REGION OF TUBULAR FLAMES

ABSTRACT

Metallic tungsten nanoparticles have attracted considerable attention because of their unique structures and excellent performances. This chapter† describes the synthesis of a mixture of tungsten metal and oxide nanoparticles via a fuel-rich tubular flame process, followed by mild-reduction-based post-heating treatment. The high combustion efficiency of the tubular flame process enables complete consumption of O_2 in the premixture, along with the emission of CO and H_2. The experimental results revealed that the tubular flames produced mixtures of amorphous tungsten oxide and crystalline tungsten nanoparticles with primary particle sizes of 5–10 nm, at a production rate of 4.68 mg/h and yield of 8.64%. These nanoparticles exhibited a sinter-necked structure. The oxygen content of the tubular-flame-synthesized mixtures of tungsten metal and oxide nanoparticles (16.80%) to 5.56% after the additional post-heating treatment, which also retained the particle size.

† published in part in *J. Chem. Eng. Japan.*, 54, 557-565, 2021.

3.1 INTRODUCTION

Metallic tungsten nanoparticles are promising materials because of their various beneficial physical properties, such as melting point, thermal stability, electrical and thermal conductivities, and superior hardness compared to those of other materials. Metallic tungsten has been applied in various fields such as biomedical, energy, electronic, catalytic, and metallurgical industries [82].

Metallic tungsten powder is generally produced by a method involving a reaction with a hydrogen stream [83], which enables the production of a large amount of high-quality tungsten metal. However, this strategy is unsuitable for nanoparticle production because the lengthy duration of the reaction leads to aggregation and crystal growth, which results in the presence of micrometer-sized particles in the final product [82,84–88]. Several approaches have been devised for producing tungsten nanoparticles, including plasma synthesis [89–91], physical vapor deposition [92], laser ablation [93], liquid-ammonia-based synthesis [94], solvothermal synthesis [95], carbothermal reduction [96], molten salt techniques [97], and ball milling [98].

Flame aerosol synthesis is considered to be a rapid nanoparticle-production process [6,99]. Metallic particles have been prepared by using reducing flames or ultralow concentrations of oxygen during combustion, which resulted in the synthesis of bismuth (10–66 g/h) [37], cobalt (>30 g/h) [38], and copper nanoparticles (10 g/h) [100]. A tubular flame reactor that enables the direct synthesis of WO_3 nanoparticles was recently developed by our group [101]. Tubular flames, especially swirl-type tubular flames, are thermally stable because of the negligible conductive heat loss of the flame owing to the symmetrical temperature distribution [47]. The temperature distribution in tubular flames is homogeneous and controllable. The flow field of the flame consists of a low-density inner burned gas region and a high-density outer unburned gas region. The tubular flame is aerodynamically stable even at high injection velocities and over a wide fuel-concentration range.

Figure 3.1 shows a schematic diagrams of the flame structure and reaction atmospheres in flame aerosol processes conducted using a tubular flame. Fuel-rich tubular flame combustion can provide a reducing atmosphere using oxygen-free inner flames. When tubular flames are used for the aerosol synthesis of particles, the precursors and particles do not pass through the unburned fuel and the flame front, but flow through the oxygen-free combustion gas region. This indicates that the effects of oxidation during fuel combustion, and the presence of oxygen in the premixture can be minimized in the process of particle formation, and the reduction of precursors and particles can be promoted by reductive species in the combustion gas. However, in the case of diffusion flames (Figure B.1 in Appendix B), the precursors and particles sequentially pass through the unburned fuel, the flame front, and the oxidizer and combustion gas region. Moreover, the direct synthesis of metal nanoparticles is difficult even in the case of oxygen-deficient combustion because conventional methods cannot use only the reducing gas contained in the combustion gas, and are significantly affected by the fuel, oxidizer, combustion reaction, and atmospheric inflow.

Inspired by the aforementioned specific characteristics of tubular flames, the present study was designed to enable the first proof-of-principle experiment on the synthesis

of metallic tungsten using a fuel-rich tubular flame process. The effects of the equivalence ratio (fuel concentration) and carrier gas flow rate in tubular flame combustion on the chemical composition and morphology of the produced particles were comprehensively investigated in this study. To the best of our knowledge, this is the first study that has examined the reduction of fine particles in tubular flames.

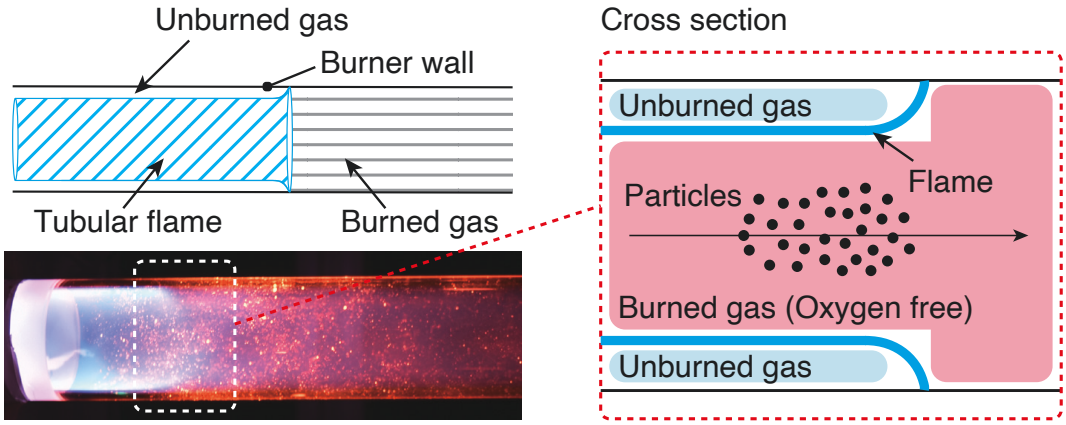

Figure 3.1: Schematic representations of the investigated tubular flame system.

3.2 EXPERIMENTAL

3.2.1 *Materials*

The particles were prepared using an aqueous precursor solution containing ammonium tungstate pentahydrate [ATP, $(NH_4)_{10}(W_{12}O_{41})\cdot 5\,H_2O$; purity 88–90%; Kanto Chemical Co., Inc., Tokyo, Japan]. CH_4, Ar, and dry air were used as the main fuel, carrier, and oxidizer, respectively in the tubular flame combustion. CH_4 and Ar (purity greater than 99.999%) were provided by the Nakamura Sanso Corporation, Hiroshima, Japan.

3.2.2 *Particle synthesis*

The precursor was prepared by dissolving ATP to form an aqueous solution (10 mmol/L), which was stirred at 300 rpm at room temperature, and subsequently placed in a particle production system; a detailed schematic diagram of this system has been presented elsewhere [101]. In the experiment, the precursor was transformed into droplets using an ultrasonic nebulizer (NE-U17, Omron Healthcare Co., Ltd., Tokyo, Japan). The generated droplets were transported into the tubular flame burner through an axial inlet hole with an internal diameter (D_{inj}) of 6.35 mm, assisted by a flow of Ar gas as the carrier gas (Q_C = 0.05–0.2 m^3/h). Detailed information regarding the tubular flame burner used herein has been presented in Figure B.2 in Appendix B. The burner consists of a burner body and combustion chamber. The tubular flame burner (D_o) has an internal diameter of 20 mm, and the two tangential injection holes of the burner have an internal diameter (D_s) of 3 mm. The tube for injecting the precursor was in-

Table 3.1: Parameters of various experimental scenarios, production rates, and yields.

Sample no.	Q_{CH_4} [m³/h]	Q_{Air} [m³/h]	Q_C [m³/h]	ϕ [-]	Prod. Rate [mg/h][a]	Yield [%][b]
1	0.056	0.609	0.2	0.88	100	18
2	0.056	0.537	0.2	1	41.5	7.46
3	0.056	0.477	0.2	1.12	50	8.99
4	0.056	0.428	0.2	1.25	48.7	6.56
5	0.056	0.477	0.1	1.12	48	8.63
6	0.056	0.477	0.08	1.12	20	10.8
7	0.056	0.477	0.05	1.12	4.68	8.64

[a] Error (for sample no. 7): ± 1.5 mg
[b] Error (for sample no. 7): ± 3 %

stalled at one axial end of the burner, and a combustion chamber with an internal diameter of 20 mm was installed at the other end. A tubular flame was formed using CH_4 as the fuel and dry air from a compressor as the oxidizer. These components were mixed in a supply line and tangentially injected into the burner from the tangential injection holes. The tubular flame was generated by igniting the mixture using a torch. The carrier gas (Ar), which contained the precursor material, was fed axially from the tube; the supply line was separated from the fuel/air line. The experiments were performed at various equivalence ratios (ϕ) and carrier gas flow rates (Q_C), as shown in Table 1. The fuel flow rate, Q_{CH_4}, was set to be 0.06 m³/h to enable heat release from the mixture. The equivalence ratio was varied by changing the air flow rate under fixed fuel-flow-rate conditions. ϕ is defined as the ratio of the actual fuel/air ratio to the stoichiometric equivalent (independent of the amount of the carrier gas), and can be expressed as follows:

$$\phi = \frac{m_{Fuel}/m_{Air}}{(m_{Fuel}/m_{Air})_{st}} \tag{1}$$

where m_{Fuel}/m_{Air} are the mass of fuel and air, respectively. The value of $(m_{Fuel}/m_{Air})_{st}$ was fixed at 0.105. $\phi < 1$ and $\phi > 1$ represent processes with excess oxygen and excess fuel, respectively. The value of ϕ was controlled by adjusting the flow of air (Q_{Air}), and fixing the CH_4 flow rate (Q_{CH_4}) at 0.06 m³/h. The swirl numbers (S_W), which are representative of the degree of rotational motion, exceeded 0.6 under all the experimental conditions. This indicates the formation of a strong swirl flow in the burner. Detailed information on S_W information has been provided in Appendix B. The produced particles were collected using a bag filter (HORKOS Corp., Hiroshima, Japan) with a scroll pump (nXDS15i, Edwards GmbH, Germany). The experimental scenarios are listed in Table 1. The decrease in oxygen contents of the flame-synthesized particles was achieved by post-heating under a 5% H_2/Ar atmosphere at 800°C for 3 h.

3.2.3 *Characterizations*

Field-emission scanning electron microscopy (FE-SEM; S-5200, Hitachi High-Tech. Corp., Tokyo, Japan) was employed to examine the shapes and morphologies of the prepared

particles. Powder X-ray diffraction (XRD; D2 PHASER, 40 kV and 30 mA, Bruker Corp., USA) and transmission electron microscopy (TEM; 297 kV, JEM-3000F, JEOL Ltd., Tokyo, Japan) were used to examine the crystal structures and microstructures, respectively, of the prepared particles. The weight percentages of WO_3, $WO_{2.72}$, W, and the amorphous form were determined by Rietveld analysis using Total Pattern Analysis Solutions software (TOPAS version 6; Bruker AXS GmbH, Karlsruhe, Germany) [102, 103]. The oxidation states of tungsten were examined by X-ray photoelectron spectroscopy (XPS; ESCA-3400, Shimadzu Corp., Kyoto, Japan, operated at 10 kV and 20 mA). The C 1s spectrum was used to calibrate the energy dependence, and the Shirley method was used for background subtraction. The C, H, N, and O contents of the particles were measured using a CHN analyzer (CHNS/O 2400 II, PerkinElmer, Inc., Waltham, MA, USA) and an O analyzer (EMGA 930, Horiba, Ltd., Kyoto, Japan). The concentrations of CO and O_2 corresponding to the various ϕ values at the end of the combustion tube were determined using a gas analyzer (CGT-7000 and POT-8000, Shimadzu Corp., Kyoto, Japan) without carrier gas injection during the measurements.

3.3 RESULTS AND DISCUSSIONS

3.3.1 *Flame appearance*

Figure 3.2a and b show the flame appearances corresponding to various equivalence ratios (Figure 3.2a) and carrier gas flow rates (Figure 3.2b). In the experiments depicted in Figure 3.2a, ϕ was varied by changing the flow rate at a fixed fuel-flow-rate (Q_{CH_4}) of 0.06 m^3/h. It is worth noting that the carrier gas was also supplied to the burner in the axial direction to simulate an actual synthetic process under a fixed-flow-rate condition (Q_C = 0.20 m^3/h). In the experiments depicted in Figure 3.2b, ϕ was fixed at 1.12 and the carrier gas flow rate was varied from 0.05 m^3/h to 0.20 m^3/h. The images of the flames in the left column in Figure 3.2b were captured from the axially downstream position of the burner, and the images on the right were obtained through the quartz combustion chamber. The dotted lines in Figure 3.2a and b indicate the walls of the quartz combustion chamber. Clear images of the flame were obtained under dark conditions by mounting the tubular flame burner horizontally, because of spatial limitations. Photographs of the flame without the carrier gas are shown in Figure B-4 in Appendix B. In Figure 3.2a, tubular flames can be recognized in the cross-sectional view (left column) for scenarios in which ϕ = 0.88–1.12. Notably, the flames are short in the axial direction, indicating that only a small portion of the luminous flame zones can be observed in the right column of Figure 3.2a. At ϕ = 1.25, the flame is not visible in the burner, and a diffusion flame is formed at the exit of the combustion tube by the unburned mixture and surrounding air. Although this condition is far from the upper flammability limit of a CH_4/air mixture (ϕ = 1.6), the dilution of the mixture (22%) by the carrier gas (Ar) results in an upper flammability limit of ϕ = 1.26 [104]. For a fuel-rich CH_4/air/Ar mixture, the Lewis number of the deficient reactant (O_2) is larger than unity (Le = 1.03 for the scenario in which ϕ = 1.25 in Figure 3.2a); moreover, the flame is not intensified by the thermodiffusive instability. Therefore, a flame cannot presumably be formed at ϕ = 1.25 (Figure 3.2a). Figure 3.2b shows the appearances of

flames obtained at various carrier gas flow rates. The figure shows that a stable flame is formed at each condition. This indicates that the effects of carrier-based dilution are negligible in the case of the tubular flame obtained at ϕ = 1.12.

3.3.2 *Gas composition*

The composition of the burned gas is the most critical parameter in the flame synthesis of fine particles. The concentrations of CO (a major reductive component) and O_2 in the burned gas at the exit of the tubular flame burner were examined. Figure 3.3 shows plots of the experimentally obtained CO and O_2 concentrations in the burned gas component of the tubular flame. The burned gas was sampled at a radially central position 10-mm upstream of the exit of the combustion tube to avoid the effects of air entrainment. Figure 3.3 indicates that the O_2 fraction of the burned gas region of the tubular flame , which is >2% at for ϕ = 0.9, considerably decreases with increasing ϕ. The O_2 concentrations are 1530 ppm and almost zero at ϕ = 1.0 and ϕ > 1.0 respectively. The CO concentration increases from nearly zero to 3650 ppm at ϕ < 0.8 and ϕ = 0.96, respectively; moreover, it exceeds 25000 ppm under fuel-rich conditions (ϕ > 1.0). These results clearly indicate that a reductive, ultralow O_2 atmosphere can be achieved in the burned gas region during fuel-rich tubular flame combustion. Figure 3.3 shows the equilibrium concentrations of CO and O_2 (single- and double-dotted lines, respectively) calculated using the NASA CEA program [105]. The equilibrium concentrations of other major combustion products as a function of ϕ are shown in Figure B.5 in Appendix B. Figure 3.3 shows that the experimentally obtained CO and O_2 concentrations are in excellent agreement with the equilibrium values. Importantly, this indicates that a high CO concentration and an ultralow O_2 concentration can be achieved in the tubular flame burner, and these concentrations can be conveniently predicted using the chemical equilibrium compositions. These gaseous conditions are considered to be ideal for synthesizing high-quality metal particles. It is worth noting that the equilibrium calculations shown in Figure B.5 indicate that a high concentration of H_2 can also be achieved in the burned gas, which can further contribute to the product reduction.

3.3.3 *Effects of equivalence ratio on particle properties*

Figure 3.4 shows the XRD patterns and optical photographs of particles obtained using ϕ values from 0.88 to 1.25 (Table 3.1, samples 1–4). The particles prepared at ϕ = 0.88 contain monoclinic WO_3 phases. Combustion at ϕ = 0.88 occurs under oxygen-excess conditions, which results in the formation of WO_3 by thermal decomposition of ATP. At ϕ = 1.0–1.12, patterns representing $WO_{2.72}$ and metallic W [the filled circles and triangles in the figure correspond to the (010) pattern of $WO_{2.72}$ and the (110) pattern of metallic W, respectively] appeared in addition to the WO_3 patterns. Assuming that the patterns indicate an enhancement in reduction and the formation of $WO_{2.72}$ and W in the gas phase, the disappearance of the $WO_{2.72}$ and W patterns at ϕ = 1.25 (reducing conditions) is rather curious. As shown in Figure 3.2a, tubular flame combustion is not

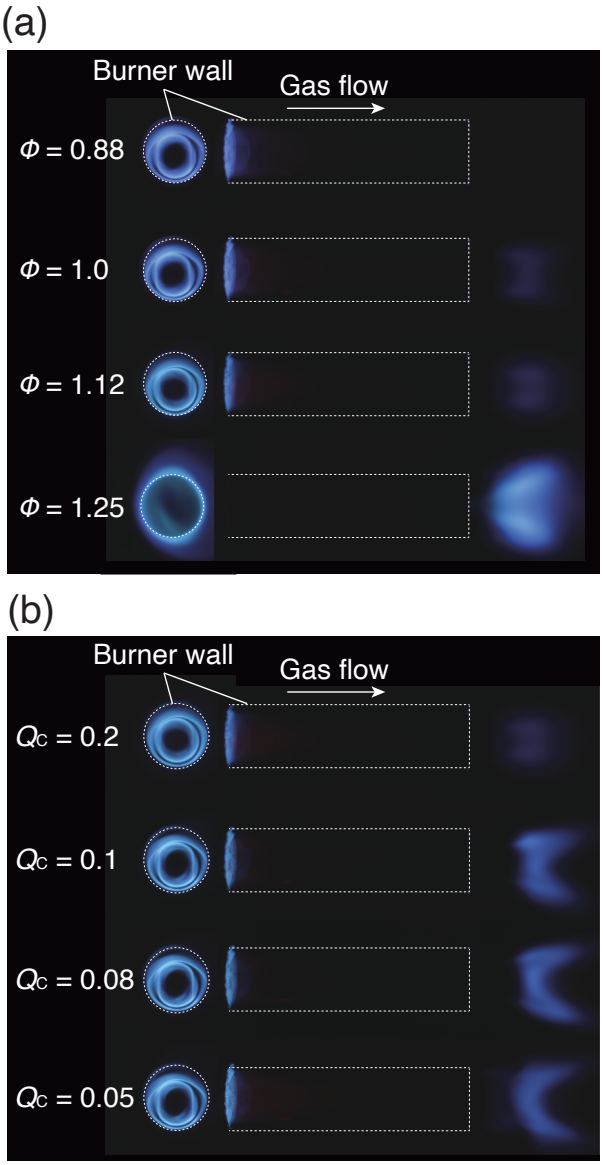

Figure 3.2: Appearances of flames at various (a) equivalence ratios and (b) carrier gas flow rates.

realized at ϕ = 1.25. This suggests that WO_3 was not reduced to a lower oxidation state of tungsten. The reduction of WO_3 was accompanied by a color change of the powder to blue at ϕ = 1.0 and 1.12. The color of tungsten oxide particles is affected by the loss of oxygen in the crystal structure [106, 107]. The particles prepared at various ϕ values were spherical and in the submicron to micron size range (Figure B.6 in Appendix B). This indicates that the particles were precipitated by a typical spray-pyrolysis process in the hot gas region of the flames [73, 108, 109].

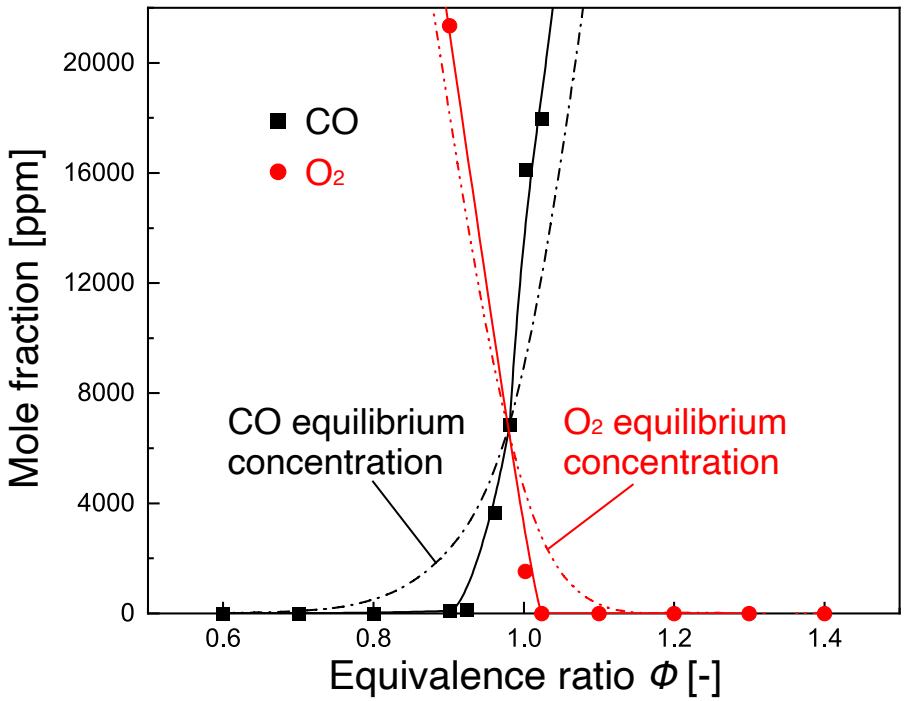

Figure 3.3: Variations in O_2 and CO emissions with the equivalence ratio during tubular flame combustion.

3.3.4 *Effects of carrier gas flow rate on particle properties*

Subsequent experiments were performed at ϕ = 1.12. The effects of the tubular-flame-combustion reducing gas were investigated by preparing blue-colored tungsten oxide (WO_x) particles via combustion at ϕ = 1.12. The carrier gas flow rate (Q_C) was adjusted in the 0.1–0.05 m^3/h range at a constant equilibrium ratio to promote reduction and to obtain tungsten particles (Table 3.1, samples 5–7). The XRD pattern of the particles prepared at Q_C = 0.1 m^3/h indicates the presence of a mixture of WO_3, $WO_{2.72}$, and W phases. Figure 3.5 shows that the intensity of the W pattern increases with a decrease in Q_C to 0.08 m^3/h. A further decrease in Q_C to 0.05 m^3/h results in the disappearance of the WO_3 and $WO_{2.72}$ phases. Rietveld analysis was conducted until the R-weighted pattern (R_{wp}) decreased to below 10 to ensure reliable refinement. These results indicate that the percentages of metallic tungsten and amorphous increase in parallel with the diminution of the tungsten oxide phases (WO_3 and $WO_{2.72}$), as shown in Table 3.2. Therefore, the reduction of the product is presumably promoted by fuel-rich combustion in the tubular flame burner with a low carrier-gas flow rate. Figure 3.6 shows SEM micrographs of the particles synthesized at various carrier-gas flow rates. The particles prepared at a carrier gas flow rate of 0.1 m^3/h are primarily of the submicrometer size. This phenomenon is similar to that in droplet–particle conversion, which produces large particles (not in the nanometer size range) because of precipitation and pyrolysis of precursor droplets in general flame-assisted spray pyrolysis using coflow diffusion flames [32]. A decrease in Q_C to 0.08 m^3/h leads to a decrease in the proportion of sub-

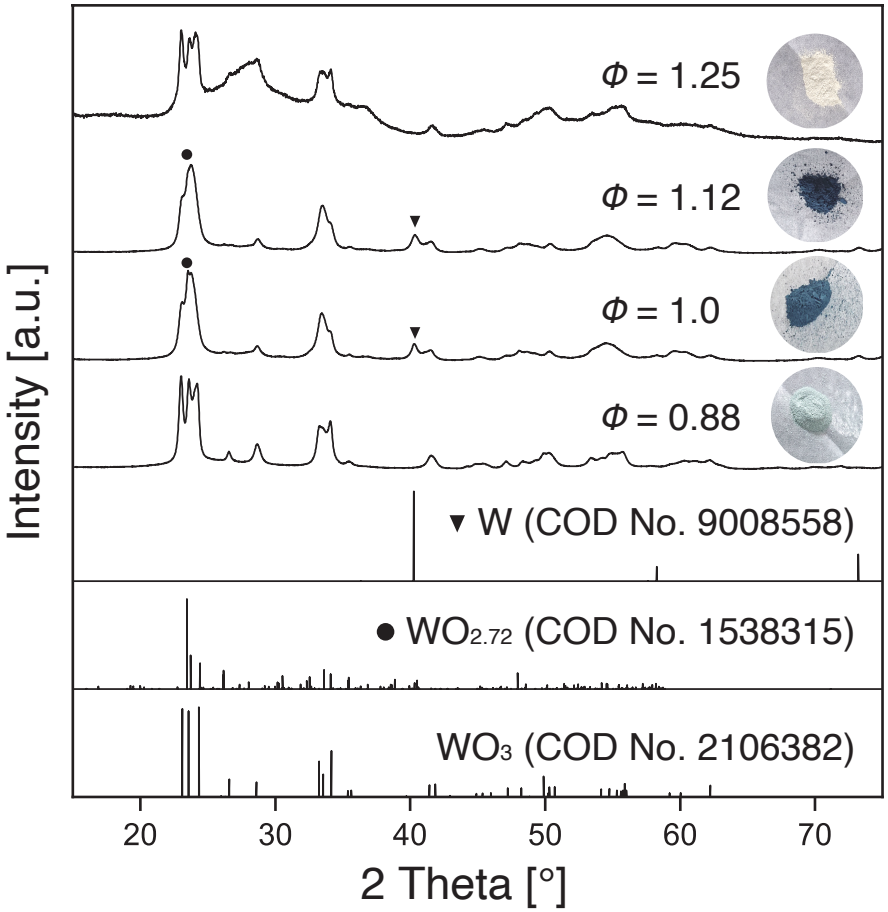

Figure 3.4: XRD patterns of particles produced at various values of ϕ.

micrometer particles, and the initiation of nanoparticle formation. A further decrease in Q_C to 0.05 m^3/h results in the disappearance of the submicrometer particles and the formation of nanoparticles. The decrease in carrier gas flow rate leads to an increase in the residence time in the hot gas region and an increased supply of energy to the precursor. This leads to gasification of the precursor and nucleation of the nanoparticles by gas-to-particle formation [10].

3.3.5 *Characterization of particles formed at carrier gas flow rates of 0.05 m^3/h*

A TEM image of particles formed at a Q_C of 0.05 m^3/h (Table 3.1, sample 7) is shown in Figure 3.7a. The primary particle sizes are in the range of 5–10 nm, with a narrow particle size distribution (Figure B.7 in Appendix B). The high-resolution TEM image in Figure 3.7b shows that the particles exhibit a homogeneous crystal orientation with a lattice spacing of 0.22 nm, which corresponds to the (1 0 0) plane in metallic tungsten. Moreover these nanoparticles have a sinter-necked structure. A possible method for avoiding the sintering of particles involves the introduction of processes such as rapid cooling of the flame-synthesized particles [17]. Figure 3.8 shows XPS profiles

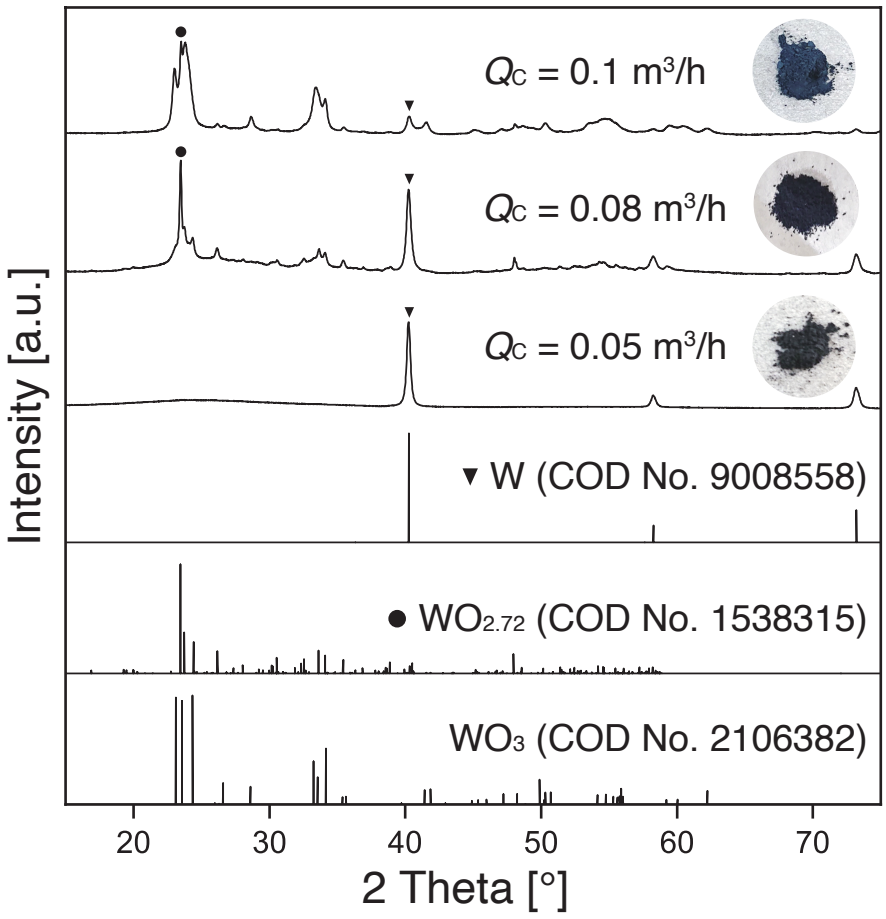

Figure 3.5: XRD patterns of particles produced at various carrier-gas flow rates.

after 1 min of sample etching with Ar^+ ions. Etching with Ar^+ ions is known to induce a decrease in the oxidation state of tungsten [110]. For comparison, the XPS profiles of WO_3 particles produced in the tubular flames were also recorded (Figure 3.8a). The WO_3, spectrum can be deconvoluted into four peaks: WO_3 ($W4f_{7/2}$ at 35.0 eV and $W4f_{5/2}$ at 37.3 eV) and WO_x ($x < 3$; $W4f_{7/2}$ at 33.9 eV and $W4f_{5/2}$ at 36.2 eV). The WO_3 particles are slightly reduced by reductive chemical species present locally in flames. A comparison of the spectrum with that of the sample prior to Ar^+-ion irradiation does not indicate any changes (Figure B.8a in Appendix B); moreover, a chemical shift to a lower energy caused by the reduction of tungsten oxide does not occur. Essentially, the effect of 1-min Ar^+-ion irradiation on the chemical state is negligible, and depth information is considered to have been obtained. In the spectrum of particles formed at a carrier gas flow rate of 0.05 m^3/h (Table 3.1, sample 7), peaks appear at 31 eV and 33 eV; moreover, the spectrum can be deconvoluted into six peaks representing WO_3, WO_x, and metallic tungsten ($W4f_{7/2}$ at 31.0 eV and $W4f_{5/2}$ at 33.2 eV). The absence of metallic tungsten peaks prior to Ar^+-ion irradiation (Figure B.8b in Appendix B) indicates the formation of oxide layers on the top surface of the nanoparticles. This is presumably because of the oxidation of the surfaces of the tungsten nanoparticles

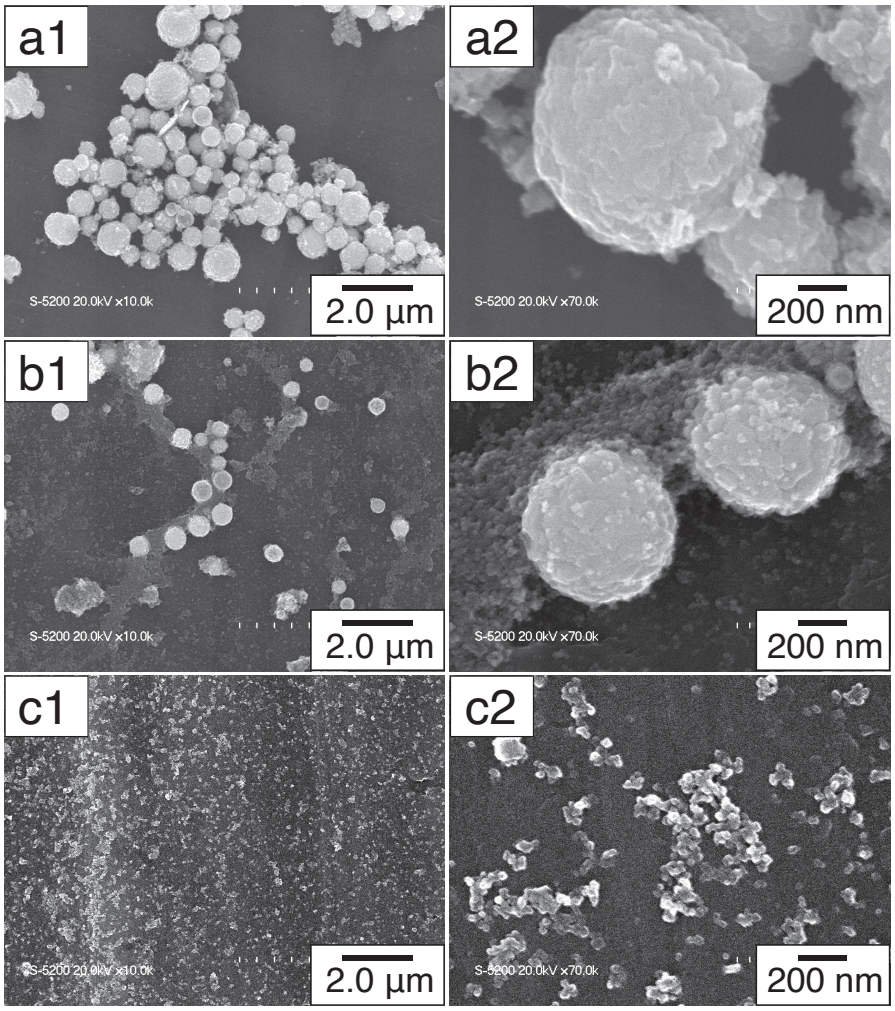

Figure 3.6: SEM images of particles formed at carrier gas flow rates of (a1, a2) 0.1, (b1, b2) 0.08, and (c1, c2) 0.05 m^3/h

during their flow through the flame region at a high temperature or during the exposure of the particles ambient laboratory. This thin oxide layer is expected to prevent the ignition of metallic tungsten particles and facilitate handling.

The XRD results show that 63.11% of the particles formed at a carrier gas flow rate of 0.05 m^3/h are amorphous. The chemical components of the amorphous particles and impurities were evaluated by determining the contents of C, H, N, and O, which are impurities in the particles using a combustion analyzer. The contents of C, H, N, and O were 1.77%, 0.02%, 0.99%, and 16.80%, respectively. Carbon contamination caused by incomplete combustion was confirmed by the broad patterns observed in the low-angle XRD patterns (Figure 3.5). Therefore, the CHN/O analysis indicates that the amorphous form presumably contains W, C, H, N, and O. Although the flame-synthesized nanoparticles contain 16.80% of oxygen, the metallic tungsten phase was confirmed to be the main phase by XRD; moreover, the presence of the tungsten phase was also confirmed by local TEM analysis. Post-treatment of nanopar-

Table 3.2: Weight percentages of particles produced at various carrier-gas flow rates obtained by Rietveld refinement.

Q_C [m³h]	WO_3 phase [%]	$WO_{2.72}$ phase [%]	W phase [%]	Amorphous [%]
0.2	72.32	21.22	3.89	2.67
0.1	72.49	20.73	3.18	3.6
0.08	38.96	36.05	13.34	11.65
0.05	-	-	36.89	63.11

ticles (e.g., reduction or annealing) is typically conducted prior to their application in practical situations. Therefore, mild reduction was performed at 800°C for 3 h under a 5% H_2/Ar atmosphere. The XRD pattern of the particles obtained after reduction (Figure 3.9a) also shows the W phases, whose weight percentage increases to 64.27%. The oxygen content of the particles was estimated using the EMGA analyzer to be 5.56%. In addition, the particle sizes remain within the nanometer range (Figure 3.9b). More intensive conditions (100% hydrogen atmosphere) have been previously used to reduce WO_3 to metallic W. Moreover, the purities of tungsten in commercially available tungsten powders are ≥99.9% (W-H, 0.45–0.59 μm in size, JAPAN NEW METALS CO.,LTD) or ≥99.9% (A20, 0.5–0.6 μm in size, A.L.M.T. Corp). The tungsten percentage purity of the product synthesized herein by tubular flame combustion followed by reduction treatment was 94.44%, indicating that it is not as pure as the commercially available tungsten powders. Therefore, further optimization of the tubular flame combustion and purification process are required. The production rates and yields of the investigated process are listed in Table 3.1. As mentioned earlier, tungsten materials were prepared using ATP. Moreover, the yield of WO_3 was calculated for sample no. 1–6. For sample 7 represents metallic tungsten. Although the yield and productivity of the current system are not as high as those of previously reported large-scale flame processes (e.g., 10 g/h for carbon coated Cu) [22], the present study shows promise for being the first study to explore the possibility of metal particle production using tubular flame combustion.

3.4 CONCLUSIONS

The possibility of metal particle production by the utilization of the internal reducing gas region of tubular flames was investigated herein. The influence of equivalence ratio, ϕ, and carrier gas flow rate on the properties of the obtained particles were experimentally evaluated. The composition of the combustion gas in the tubular flame was precisely controlled by adjusting ϕ, and combustion at ϕ >1.0 resulted in an ultralow oxygen atmosphere with a high CO content (>25000 ppm) in the tubular flame burner. Fuel-rich tubular flame combustion at ϕ = 1.12 resulted in the formation of sinter-necked mixtures of amorphous tungsten oxide and crystalline tungsten nanoparticles with primary particle sizes of 5–10 nm, at a production rate of 4.68 mg/h and yield of 8.64%. The tubular flame-synthesized mixtures of tungsten metal and oxide nanopar-

ticles contained 16.80% of oxygen , which decreased to 5.56% after mild reduction at 800°C for 3 h under a 5% H_2/Ar atmosphere.

AKNOWLEDGEMENTS

This work was supported by JSPS KAKENHI Grant Numbers JP20J20823 (T.H.) and JP19H02500 (T.O.) This work is partly supported by the Center for Functional Nano Oxide at Hiroshima University, International Network on Polyoxometalate Science, JSPS Core-to-Core Program, The Information Center of Particle Technology, Japan, and Hosokawa Powder Technology Foundation, the Foundation for the Promotion of Industrial Explosives Technology, and the Kato Foundation for the Promotion of Science (KS-3229).

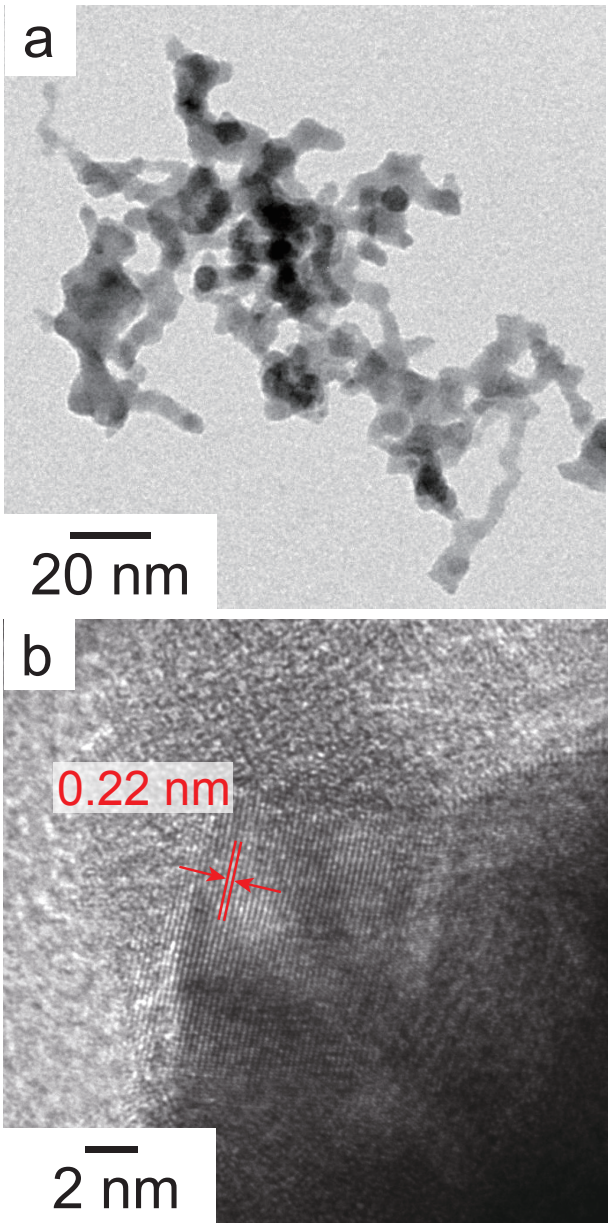

Figure 3.7: (a) TEM image and (b) high-resolution TEM image of particles formed at a carrier gas flow rate of 0.05 m^3/h (sample 7 in Table 3.1)

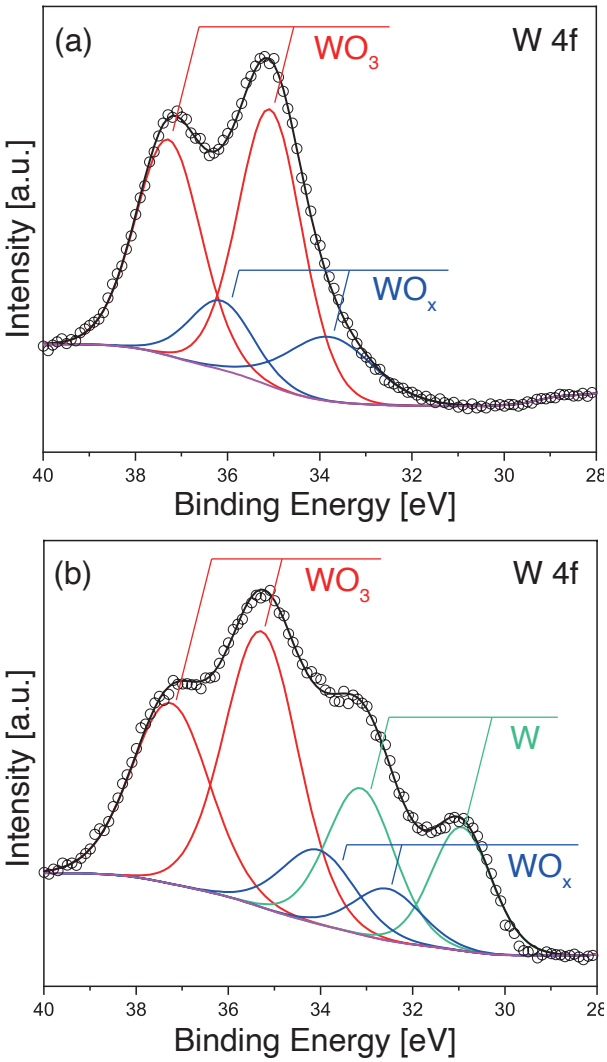

Figure 3.8: XPS profiles of (a) tungsten oxide particles (sample 1) and (b) a mixture of tungsten metal and oxide nanoparticles (sample 7) produced in the tubular flames.

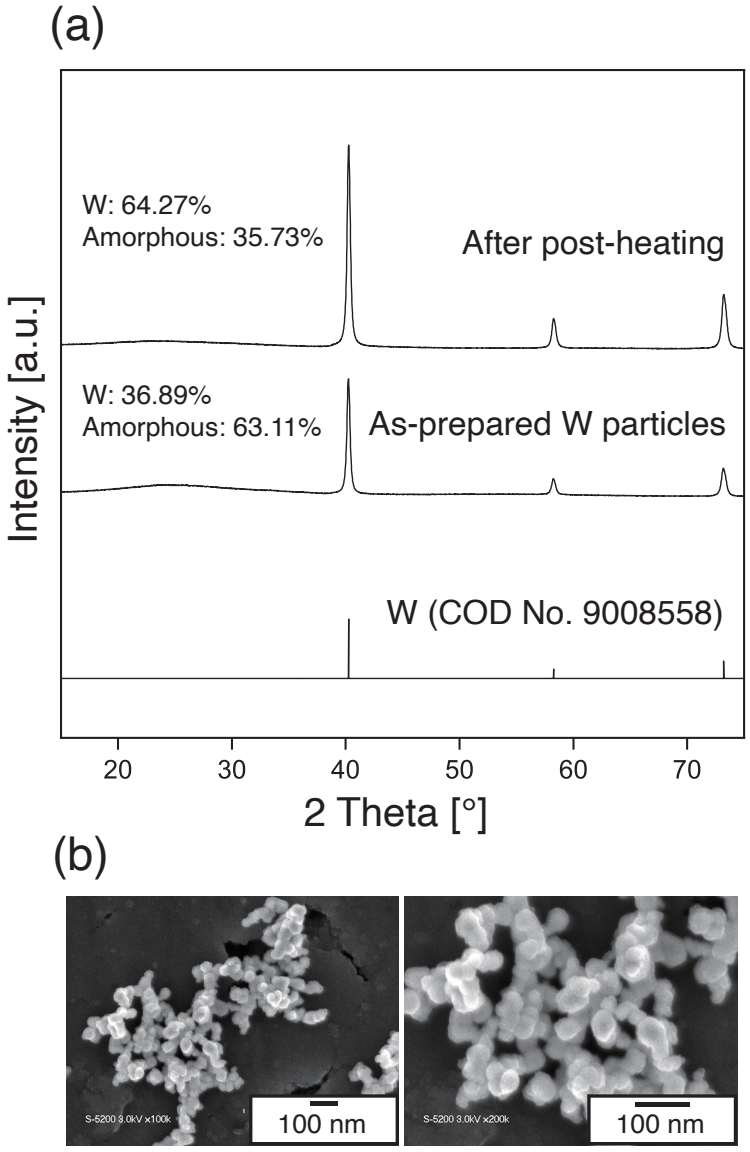

Figure 3.9: (a) XRD patterns and (b) SEM images of the particles obtained after post-heating.

4

DIRECT SPRAY COMBUSTION IN A TUBULAR FLAME BURNER

ABSTRACT

In this chapter†, a tubular flame burner equipped with a two-fluid nozzle for liquid precursor injection was developed and applied to the synthesis of fine particles. A tubular flame was established based on the axial spray of ethanol as a liquid fuel from the two-fluid nozzle. As the axial spray mixture from this nozzle merged with the tangential methane/air mixture from the tubular flame burner, a single flame front was established at the base of the burner. The flame structure was assessed by fabricating an optically accessible burner from quartz and OH^*, CH^* and C_2^* emissions were investigated using a spectrometer and ICCD camera. The results show that a lifted flame was formed when the tubular flame was outside the flammable range, whereas a stabilized flame was obtained with the tubular flame in the flammable range. These results indicate that flame stability was primarily determined by the tubular flame. Optimal particle synthesis also required the tubular flame to be in the flammable range. Gas phase temperature measurements indicated that the main flame could be well-stabilized while maintaining a high-temperature environment by using a fuel-lean tubular flame, even in conjunction with the direct injection of liquid fuels. Using this flame system, both titania (TiO_2) and silica (SiO_2) nanoparticles could be synthesized.

† published in part in *J. Therm. Sci. Technol.*, 16, JTST0035, 2021.

4.1 INTRODUCTION

At present, many functional nanomaterials (including carbon black, fumed silica and TiO_2) are produced on an industrial scale using flame aerosol processes [1, 4, 6, 7, 111]. Recently, it has been recognized that such processes also have the potential to fabricate high-performance catalysts [60, 61, 112], phosphors [31], nanostructured particles [53, 62], non-aggregated particles [16] and electronic devices such as gas sensors and batteries [10, 21, 113]. One of the key aspects of flame aerosol synthesis is the combustion process, and various types of burners have been developed for use as heat sources [8]. It is critical not only to produce high quality materials in such flames but also to understand the phenomena occurring in the combustion field in detail and to use combustion energy efficiently. However, there are still some challenges related to controlling the combustion fields in both diffusion and spray flames, which are generally used in flame aerosol synthesis. Specifically, the flame temperature and combustion gas composition can exhibit considerable spatial and temporal variations due to the complicated combustion process. These non-uniform fields can result in the formation of contaminants such that an additional annealing process is required to remove impurities from the particle surfaces. Based on the above, it is evident that a well-controlled combustion process in conjunction with uniform temperature and composition fields are important to improving this technique.

A tubular flame is a thin laminar flame front established in a stretched rotating flow field, and such flames have been extensively studied over the past three decades [47–49]. A tubular flame can provide a uniform temperature and homogeneous concentrations of various species in the burned gas region because of its axisymmetric structure. This type of flame is also aerodynamically stable because it meets the Rayleigh stability criterion [67, 114], and so will provide a wide stable combustion range. Several unique techniques have been developed based on tubular flames [115], such as flame stabilization [78], non-premixed rapid mixing [116] and liquid film combustion [117–119]. Tubular flames have also been recently applied to the production of nanoparticles [101, 120]. In these systems, the raw materials are typically supplied either as gases or in an ultrasonically atomized state. The use of gas phase precursors is more common but the difficulty in obtaining volatile precursors at reasonable cost limits the use of the vapor-fed aerosol process when producing multicomponent particles. Ultrasonically atomized precursors can be used to provide a homogeneous distribution of precursor droplets [121], but the droplet flow rates and the solvents that can be used are both limited. As an example, high viscosity liquids and certain colloidal solutions (e.g. those containing metal particles) cannot be atomized in an ultrasonic nebulizer.

To overcome these drawbacks, the present work developed a tubular flame burner equipped with a two-fluid nozzle for the injection of liquid precursors. This nozzle was found to provide the high-speed nebulization of various precursor liquids including high-viscosity liquids and particle dispersions. Although the combustion characteristics of a variety of fuel/oxidizer combinations with various burner geometries have been previously researched, the direct injection of liquid fuels into a tubular flame has rarely been examined in detail. Thus, the present study investigated the combustion

characteristics of such flames over a wide range of conditions and also examined the fabrication of nanoparticles using a direct injection tubular flame.

4.2 EXPERIMENTAL

Figure 4.1 presents a diagram of the tubular flame burner with axial liquid fuel injection employed in this research. Using this apparatus, a tubular flame was established based on the tangential injection of a methane/air premixture, after which a liquid fuel containing the precursor material was directly sprayed into the combustion chamber from the two-fluid nozzle in the axial direction. The tubular flame burner had an inner diameter of 26 mm and a height of 15 mm, with two tangential holes that were 3 mm in diameter. Using a previously reported calculation [72], the swirl number of the burner, which is a measure of the degree of rotational motion, was determined to be 40. A two-fluid nozzle (AM6S-IDVL, ATOMAX Co., Ltd.) was located at one axial end of the burner and was used to provide the liquid fuel containing the precursor, while a quartz tube with an inner diameter of 26 mm and a length of 300 mm was attached to the other end of the burner as a combustion tube. This tube contained holes with diameters of 2 mm to allow for temperature measurements, located at Z = 55 and 125 mm, where Z is the axial distance from the base of the combustion tube. The gas temperature was monitored using a silica-coated Pt/Pt-13%Rh thermocouple having a wire diameter of 0.2 mm. The temperatures were corrected for thermometric errors resulting from radiation effects [76].

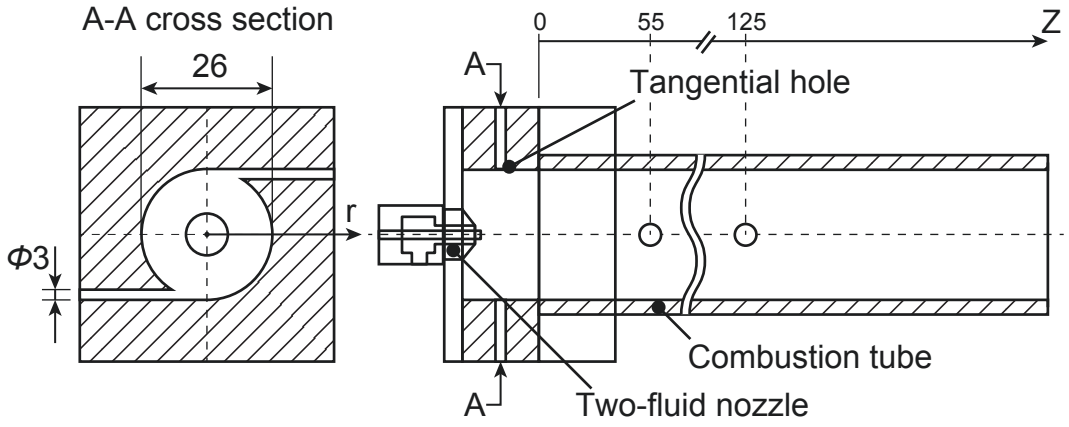

Figure 4.1: The tubular flame burner used in the present work.

Figure 4.2(a) presents a diagram of the experimental apparatus. The tubular flame was established using methane as the fuel and air as the oxidizer, both of which were dispensed using calibrated flow meters, mixed in-line and supplied to the burner. The main spray flame was produced using ethanol (Japan Alcohol Corporation, Tokyo; 99.8%) as the fuel, injected into the burner with air using the two-fluid nozzle. The ethanol flow rate was controlled by a syringe pump (PHD 2000, Harvard Apparatus, Holliston, MA). The flame appearance was monitored using a video camera (Sony, HDR-CX700). Using this system, TiO_2 or SiO_2 nanoparticles were synthesized by dis-

solving 0.1 mol/L of a precursor (TTIP; $Ti[OCH(CH_3)_2]_4$; Kanto Chemical Co. Inc., USA; purity ≥ 97% or HMDSO; $(CH_3)_3SiOSi(CH_3)_3$; Sigma-Aldrich Co., USA; purity ≥ 98.5%) in ethanol. The resulting nanoparticles were collected on a glass fiber filter installed downstream of the burner and subsequently characterized by scanning electron microscopy (SEM; S-5200, Hitachi, Tokyo, Japan) to assess both size and morphology. The crystal structures of the prepared particles were also investigated by X-ray diffraction (XRD; D2 PHASER, 40 kV and 30 mA, Bruker Corp., U.S.A.).

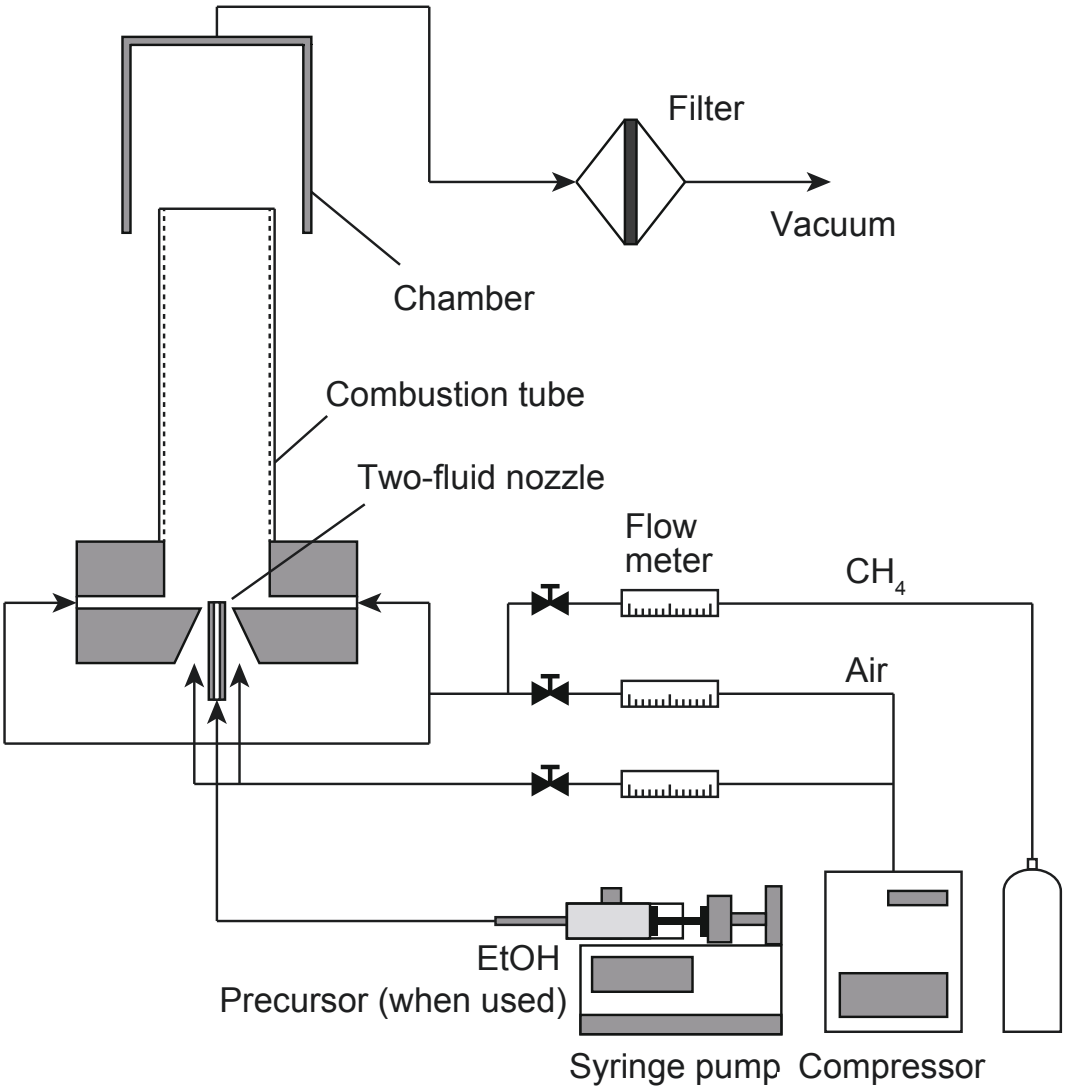

Figure 4.2: The experimental setup.

4.3 RESULTS AND DISCUSSIONS

4.3.1 *Appearance and stable combustion range of flames*

Table 4.1 provides the details of the experimental conditions. Included here are the methane and air flow rates used to generate the tubular flame (Q_{CH_4} and Q_{air}), the equivalence ratio in the tubular flame (ϕ_{TF}), the ethanol flow rate used to generate the main spray flame ($Q_{ethanol}$) and the total equivalence ratio (ϕ_{total}). In these trials, the air flow rate for the tubular flame was fixed at 4.0 m^3/h for all conditions while the air flow rate for the two-fluid nozzle was limited to 0.18 m^3/h. Thus, the main spray flame operated solely under super rich conditions in all trials ($5 < \phi < 17$).

In initial trials, only the tubular flame was observed (case [I] in Table 4.1), after which experiments were conducted using spray combustion assisted by the tubular flame. The effects of employing the tubular flame were investigated by changing the tubular flame conditions. In these trials, the spray flame was assisted by a stoichiometric tubular flame (case [II-i]) or a fuel-lean tubular flame (case [II-ii]) in conjunction with fixed spray conditions. A spray flame combined only with tangential air (case [III]) was also examined to ascertain the effects of a swirling air flow on the spray combustion. It should also be noted that ϕ_{total} was greater than unity for case [II-i] during which the process was assisted by a stoichiometric tubular flame.

Table 4.1: Experimental conditions.

ID	Condition	Tubular flame		Spray flame	ϕ_{TF}	ϕ_{Spray}	ϕ_{total}	Figure #
		Q_{CH_4} [m^3/h]	Q_{air} [m^3/h]	$Q_{ehtanol}$ [mL/min]	[-]	[-]	[-]	(appearance of flames)
1	[I] Tubular flame	0.42	4	0	1	-	1	3(a)
2		0.25	4	0	0.59	-	0.59	3(b)
3	[II-i] Spray flame assisted by stoichiometric TF	0.42	4	3	1	5.12	1.19	5(a)
4		0.42	4	4	1	6.83	1.27	5(b)
5		0.42	4	6	1	10.25	1.43	5(c)
6		0.42	4	8	1	13.66	1.59	5(d)
7		0.42	4	10	1	17.08	1.74	5(e)
8	[II-ii] Spray flame assisted by fuel lean TF	0.25	4	3	0.59	5.12	0.81	7(a)
9		0.25	4	4	0.59	6.83	0.88	7(b)
10		0.25	4	6	0.59	10.25	1.04	7(c)
11		0.25	4	8	0.59	13.66	1.2	7(d)
12		0.25	4	10	0.59	17.08	1.36	7(e)
13	[III] Spray flame with tangential air	0	4	3	-	5.12	0.24	8(a)
14		0	4	4	-	6.83	0.31	8(b)
15		0	4	6	-	10.25	0.47	8(c)
16		0	4	8	-	13.66	0.63	8(d)
17		0	4	10	-	17.08	0.79	8(e)

4.3.1.1 *Tubular flame*

Initially, the characteristics of the tubular flame without the axial injection of liquid fuel were investigated (case [I]), and Figure 4.3 provides photographic images of the methane/air tubular flames formed by the burner for different ϕ values. It is evident from Figure 4.3a that a smooth laminar tubular flame was obtained using Q_{CH_4} = 0.42 m^3/h and Q_{air} = 4.0 m^3/h (ϕ = 1.0). Decreasing Q_{CH_4} to 0.25 m^3/h while maintaining a fixed air flow rate (Figure 4.3b, ϕ = 0.59) increased the flame length while decreasing the flame diameter as a result of the decreased laminar burning velocity. The stable combustion range of the tubular flame was assessed by applying various air flow rates. The results are shown in Figure 4.4, together with the flammability limits of methane/air mixtures [122]. It is apparent that a tubular flame could be formed over a wide range of equivalence ratios close to the upper and lower flammability limits of methane/air mixtures. Thus, this apparatus was expected to allow stable spray combustion based on the effect of a stable tubular flame.

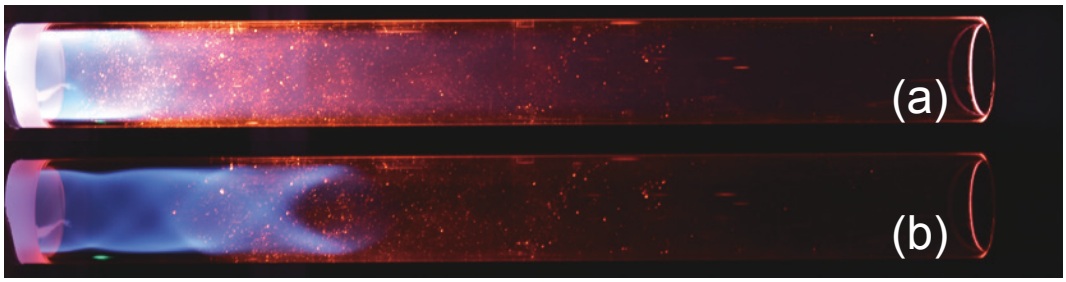

Figure 4.3: Photographic images of the tubular flames obtained using ϕ values of (a) 1.0 and (b) 0.59.

4.3.1.2 *Spray flame assisted by a stoichiometric tubular flame*

Figure 4.5 presents photographic images of flames obtained at various $Q_{ethanol}$ values in the range of 3–10 mL/min, assisted by a stoichiometric tubular flame. Because the tubular flame mixture was fixed, the total equivalence ratio, ϕ_{total}, varied with the ethanol flow rate such that ϕ_{total} was 1.19, 1.27, 1.43, 1.59 and 1.74 for $Q_{ethanol}$ values of 3, 4, 6, 8 and 10 mL/min, respectively. In all cases, regardless of the axial spray of ethanol, a tubular shape was established. The flame also became longer while its diameter was reduced with increases in the ethanol flow rate as the laminar burning velocity monotonically decreased with changes in $Q_{ethanol}$ under the fuel-rich conditions. The flame structure was further examined by assessing the appearance of the flame inside the tubular flame burner from an oblique angle at ϕ_{total} = 1.27 (ID 4 in Table 4.1). The image in Figure 4.6 shows that just a single flame front appeared. This result indicates that the axial spray mixture merged with the tangential CH_4/air mixture from the tubular flame burner to produce a single flame front at the base of the burner.

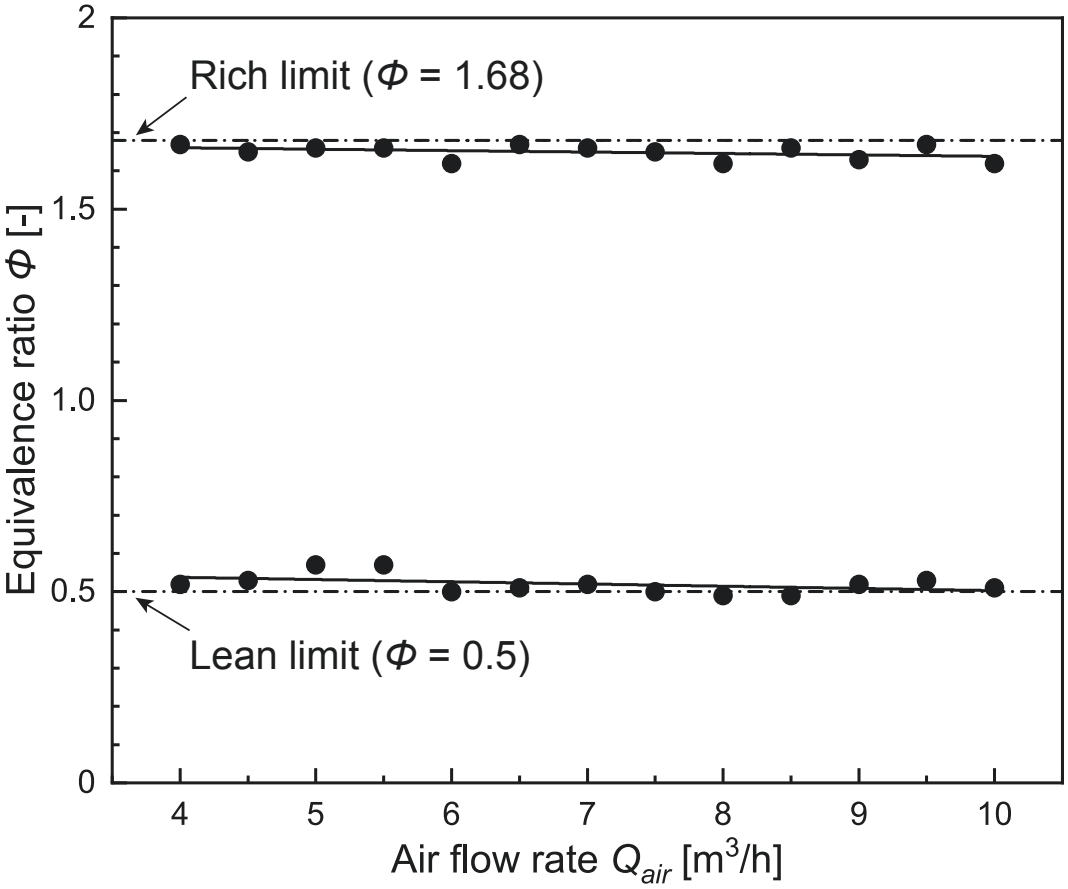

Figure 4.4: Extinction limits of the tubular flame.

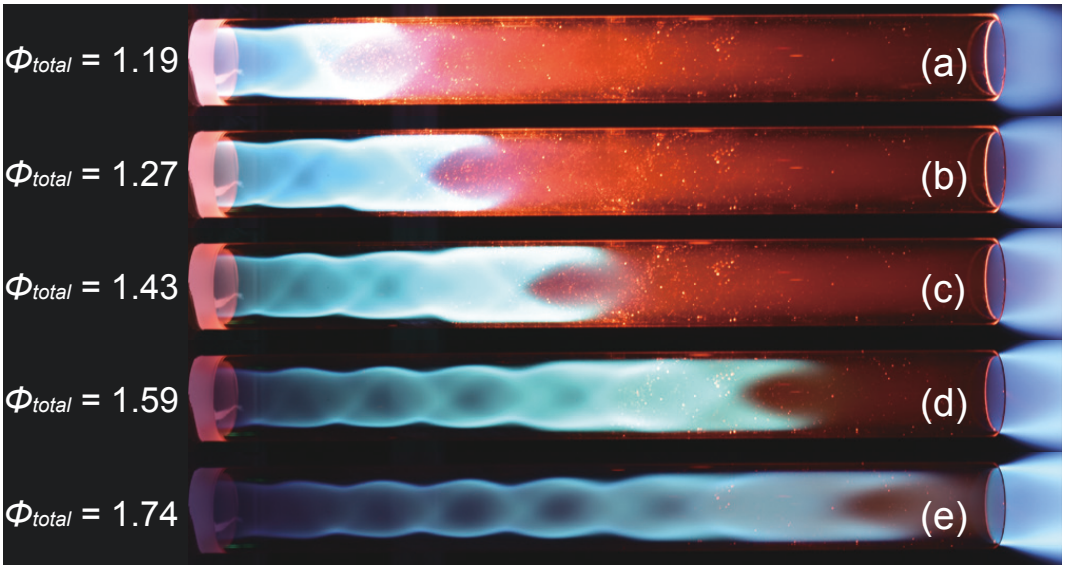

Figure 4.5: Photographic images of flames generated at Q_{CH_4} = 0.40 m³/h and ϕ_{TF} = 1.0 using various ϕ_{total}.

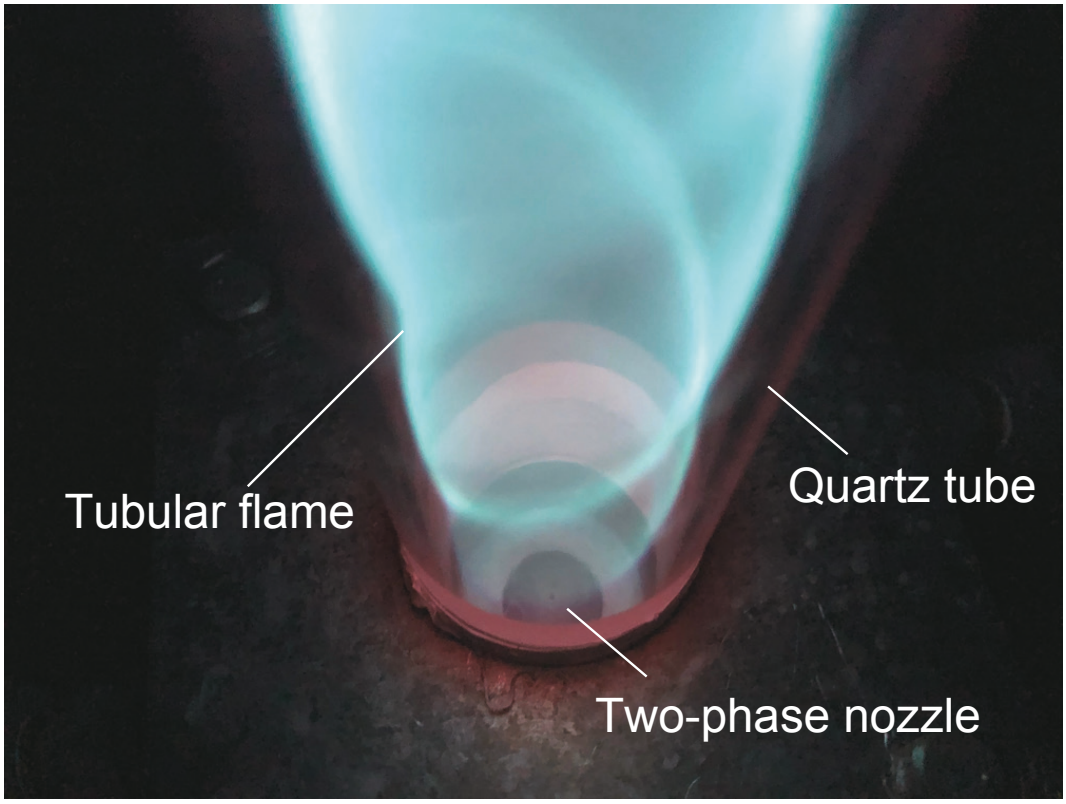

Figure 4.6: Photographic image of the flame base (ID 4 in Table 4.1).

4.3.1.3 *Spray flame assisted by a fuel lean tubular flame*

Figure 4.7 shows the appearance of the spray combustion obtained with the assistance of a fuel lean tubular flame (case [II-ii] in Table 4.1). The equivalence ratio of the mixture supplied to the tubular flame, ϕ_{TF}, during these trials was 0.59 and the associated ϕ_{total} values were 0.81, 0.88, 1.04, 1.20 and 1.36. In Figure 4.7, it can be seen that a shorter flame was obtained at ϕ_{total} = 0.88 and 1.04, and that decreasing ϕ_{total} to 0.81 or increasing the value to 1.36 gave longer flames. These results demonstrate that the length, and thus the structure, of the direct spray combustion obtained with the support of the tubular flame can be qualitatively predicted by the total equivalence ratio.

4.3.1.4 *Spray flame with tangential air (ϕ_{TF} = 0.0)*

The flame appearance was also investigated during spray combustion with tangential air but without methane, as shown in Figure 4.8. From these images, it is apparent that a flame could be formed even under super lean conditions with ϕ_{total} values of 0.24, 0.31 and 0.47, which were below the lower flammability limit of methane/air and ethanol/air mixtures. The corresponding flames were conical and exhibited weak luminosity along with yellow light emission at the flame tips. These characteristics suggest that an ethanol/air diffusion flame formed around the fuel spray. However, increasing the total equivalence ratio to 0.63 established a tube-shaped flame. This change likely

originated from the rapid mixing of the ethanol spray and the surrounding air based on the swirling flow, indicating that the swirling air provided rapid mixing of the fuel spray with air.

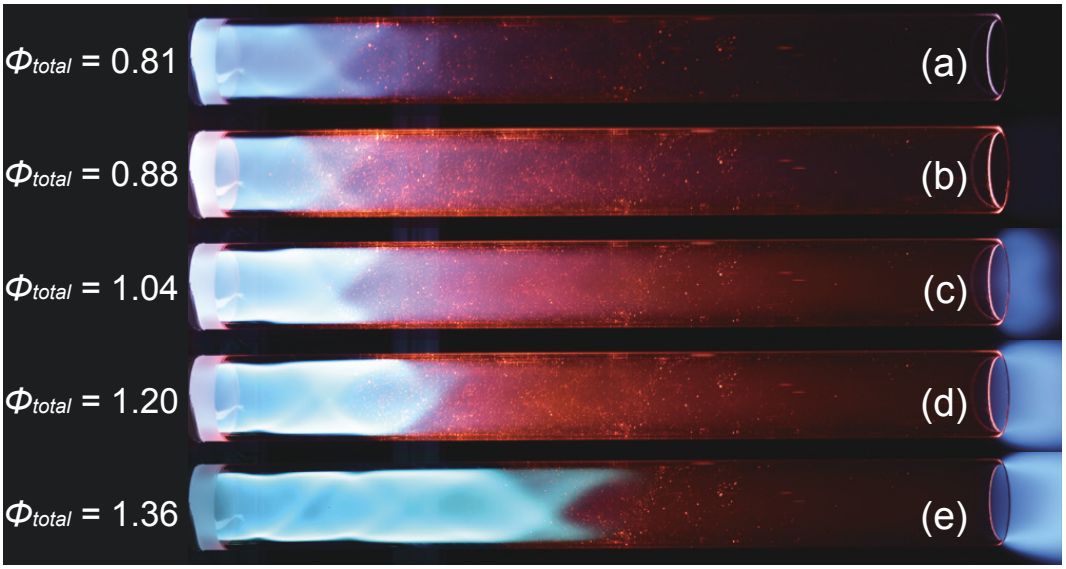

Figure 4.7: Photographic images of flames generated at Q_{CH_4} = 0.25 m^3/h and ϕ_{TF} = 0.59 using various ϕ_{total}.

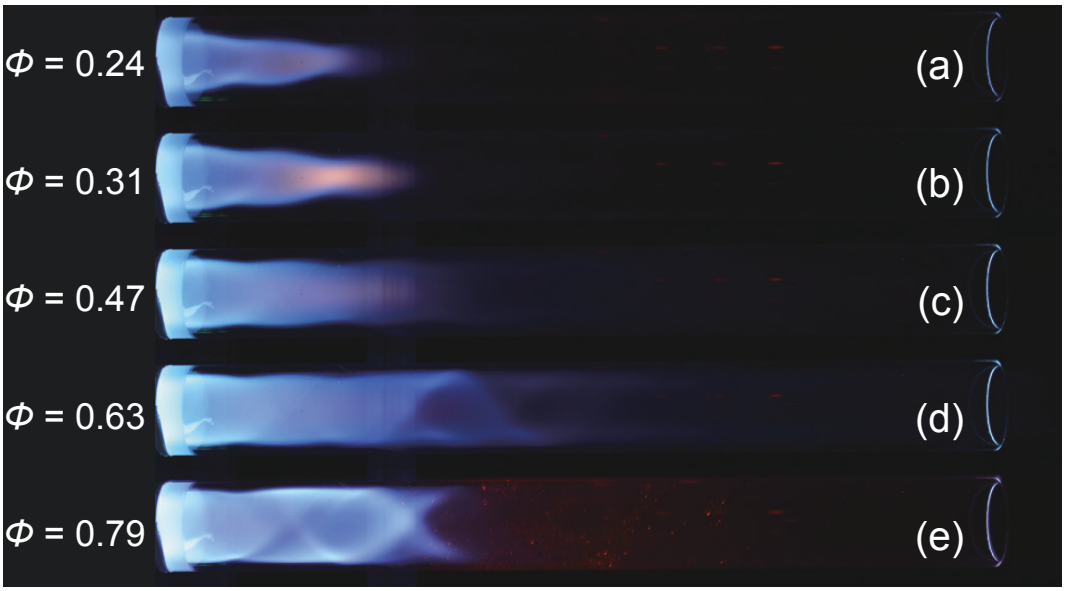

Figure 4.8: Photographic images of flames obtained by the tubular flame burner using swirl air but not methane/air mixture.

4.3.2 *Flame chemiluminescence*

To better understand the flame structure, the flame base (which primarily determines flame stability and global flame behavior) was observed during operation of the optically accessible tubular flame burner. Figure 4.9 provides a schematic of this burner, which was constructed of quartz and had the same dimensions as the burner shown in Figure 4.1, including an inner diameter of 26 mm and tangential injection hole diameter of 3 mm. The burner had a length of 72 mm and so was longer than that shown in Figure 4.1, to allow better observation of the flame base. Ethanol was sprayed directly into the tubular flame burner by the two-fluid nozzle installed at the bottom of the burner and the total length of the burner and combustion chamber was approximately 315 mm. This length was also almost equal to that of the burner shown in Figure 4.1. Flames were observed using an ICCD camera (Andor, i-star DH734) through a spectrometer (Andor, Shamrock SR-303i) incorporating a 300 lines/mm grating and using a slit width of 100 μm and gate width of less than 500 μs. A total of 100 images were acquired during each experimental run and then averaged.

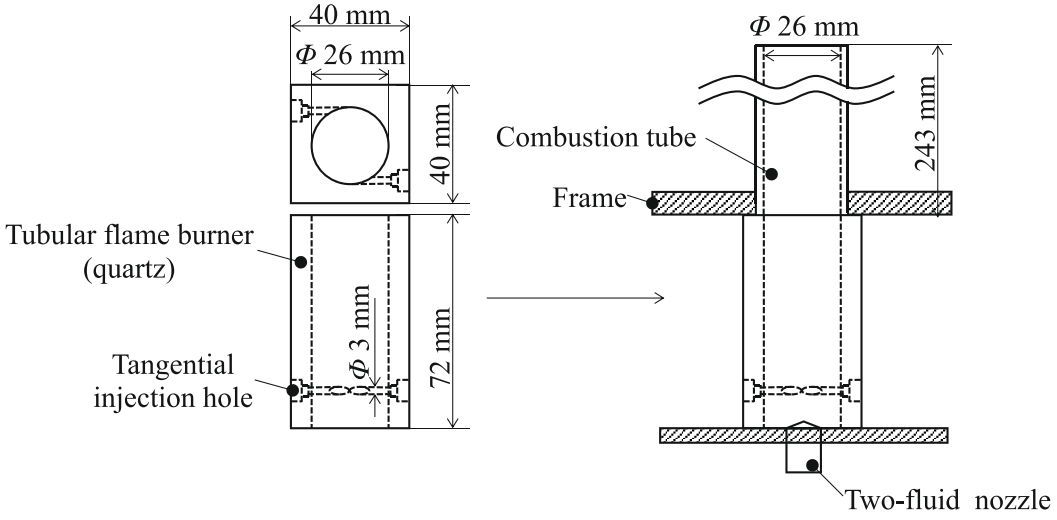

Figure 4.9: A diagram of the optically accessible tubular flame burner.

As shown in Section 3.1.4, a tube-shaped flame was established even without methane. Therefore, the effects of the tubular flame and its conditions on the flame base behavior were examined using three ϕ_{TF} values with almost the same ϕ_{total} value of 0.83. Because of the insufficient thermal resistance of the optically accessible burner, observations were made only for the three sets of conditions summarized in Table 4.2. These trials were: [i] ϕ_{TF} = 0 (without a tubular flame), [ii] ϕ_{TF} = 0.45 (with a methane/air mixture but outside the flammable range) and [iii] ϕ_{TF} = 0.55 (with a tubular flame). Although ϕ_{total} was approximately 0.83 in all cases, the spray flame was assisted by the tubular flame only for case [iii].

Table 4.2: Conditions for flame base observation with the optically accessible burner.

Condition		Tubular flame		Spray flame	ϕ_{TF}	ϕ_{Spray}	ϕ_{total}
		Q_{CH_4} [m³/h]	Q_{air} [m³/h]	$Q_{ethanol}$ [mL/min]	[-]	[-]	[-]
Spray combustion with	[i] tangential air	0	4	10.8	0	18.44	0.83
	[ii] tangential CH_4/Air mixture (out of the flammable range)	0.19	4	5	0.45	8.54	0.83
	[iii] tangential CH_4/Air mixture (in the flammable range)	0.23	4	3.5	0.55	5.98	0.82

Photographic images of the resulting flames are shown in Figure 4.10, and demonstrate that the flame base in the burner could be clearly observed. In trial [i] (Figure 4.10a), the flame base was lifted and so the sprayed fuel was evidently mixed with the tangential air in the lifted region such that the flame was stabilized by the swirling gas flow. This scenario is undesirable because the resulting flame position and structure are determined by the mixture formed in the lifted region and so cannot be controlled. During trial [ii], the flame exhibited unstable motion and the flame base propagated either upstream (toward the spray nozzle) or downstream intermittently. Figures 10b and b′ illustrate the instantaneous appearance of lifted (b) and anchored (b′) flames. The formation of a lifted flame was not unexpected in the case of trial [ii] because the ϕ_{TF} value of 0.45 was outside the flammable range. However, because this value was close to the lean flammability limit of a methane/air mixture, the addition of a small amount of ethanol from the axial spray may have resulted in the transient formation of a tubular flame (Figure 4.10b′), followed by intermittent motion of the flame base. Upon further increasing ϕ_{TF} to 0.55, unstable flame motion was no longer observed because of the assistance of the tubular flame. These results clearly indicate that the base of the spray flame, which dominated the global flame behavior, was strongly stabilized when the mixture for the tubular flame was in the flammable range.

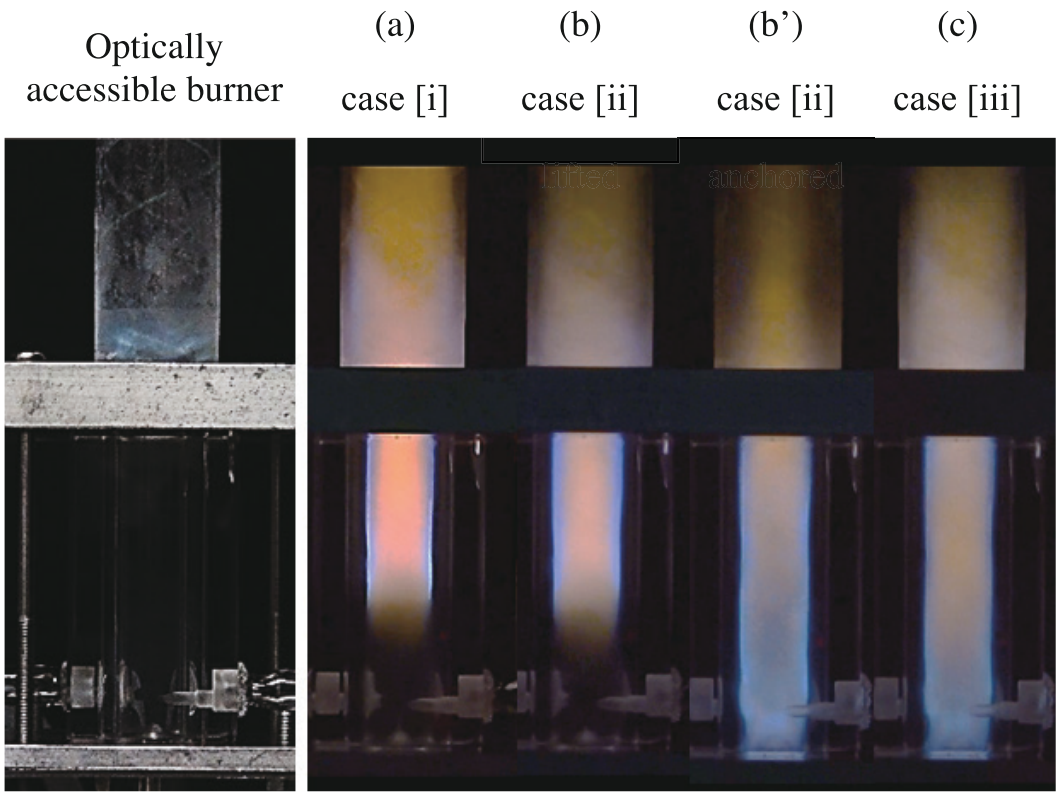

Figure 4.10: Appearance of the burner (left) and flames for (a) case [i], case [ii], (b) lifted and (b′) anchored, and (c) case [iii].

To permit a quantitative evaluation of flame position and structure, the axial distributions of OH^*, CH^* and C_2^* luminescence along the center axis of the burner (at the radial center position r = 0) are shown in Figure 4.11. Because the flame showed markedly unstable behavior for case [ii], the results for case [i] (Figure 4.11a) and [iii] (Figure 4.11b) are shown. Note that, in this figure, the relative chemiluminescent intensity normalized by each maximum value is plotted against axial distance, x, where x = 0 is the bottom of the burner and the tip of spray nozzle is at x = 10 mm. In trial [i] (Figure 4.11a), it is clear that the flame luminosity (that is, the intensity) was quite low for x = 0 to 40 mm, and that the flame base was lifted from the burner base. The intensities of OH^*, CH^* and C_2^* chemiluminescence increased gradually beginning at x = 40 mm and were maximized in the range of 55 to 60 mm. In addition, the C_2^* chemiluminescence increased earlier than the OH^* and CH^* emissions. This result indicates that the base of the lifted flame experienced fuel rich conditions even at ϕ_{total} = 0.83, because c luminescence tends to be intense when the mixture is oxygen deficient and carbon rich. In such a situation, precise control of the particle properties by changing the equivalence ratio is difficult in the lifted flame. For case [iii] (Figure 4.11b), the intensities of the OH^*, CH^* and C_2^* chemiluminescence outputs increased sharply from x = 10 mm (corresponding to the spray nozzle tip) and peaked in the range of x = 20 to 30 mm. Further downstream, the OH^* chemiluminescence was higher than those associated with CH^* and C_2^*, possibly because considerable heat was released from the fuel spray assisted by the tubular flame in this region. In the downstream region, a fuel lean flame was formed, as shown by the more intense OH^* emission compared with the CH^* chemiluminescence. These data clearly demonstrate that a well-controlled flame base could be formed with the assistance of a tubular flame even in conjunction with the direct axial spray of a liquid fuel.

4.3.3 *Temperature profile*

The flame temperature is one of the dominant factors during flame aerosol synthesis. Consequently, the radial distributions of gas temperature were assessed through the measurement holes (see Figure 4.1) under the conditions for ID 9 in Table 4.1 (ϕ_{total} = 0.88) that were used to generate nanoparticles as described in Section 3.4. From the results in Section 3.2, the conditions for ID 9 (ϕ_{TF} = 0.59) could also establish a well-controlled flame base because the mixture for the tubular flame was in the flammable range. Furthermore, the total equivalent ratio of 0.88 is the fuel-lean condition, which can provide an oxidizing atmosphere for formation of oxide particles. In an additional trial, the temperature used for ID 10 (ϕ_{total} = 1.04) was also employed for comparison purposes. Note that the appearance of these flames has already been shown in Figure 4.7b and c. Figure 4.12 provides images of the resulting flames with Z = 55 and 125 mm indicated (see also Figure 4.7b and c). Z = 55 mm corresponded to the middle of the flame while 125 mm was in the burned gas region for both ϕ_{total} = 0.88 and 1.04.

The radial distributions of gas temperatures are shown in Figure 4.13 for Z = 55 and 125 mm. Here, the temperature at each measurement point is plotted against the radial distance from the burner wall, where r = 0 is the center axis while 13 mm is

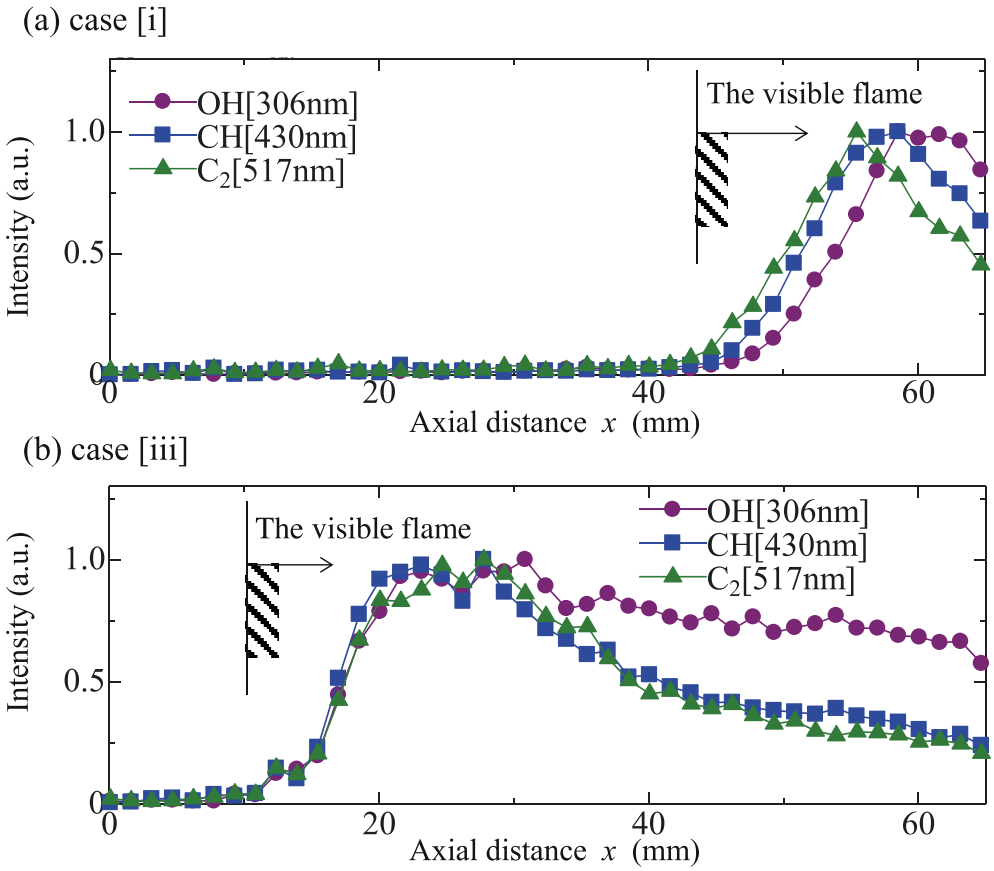

Figure 4.11: Spectral intensity distributions of OH^*, CH^*, and C_2^*.

the burner wall. In Figure 4.13a, it can be seen that the temperature for ϕ_{total} = 0.88 at Z = 55 mm was quite low (less than 200°C near the burner wall in the range of r = 10–13 mm). This finding indicates that a stable tubular flame was formed that also stabilized the inner region of the tangentially injected cold unburned gas. The gas temperature drastically increased beginning at r = 9 mm and exceeded 1600°C at r = 5 mm. After reaching a maximum of 1720°C at r = 4 mm, the temperature slightly decreased on going toward the center axis. As indicated in Figure 4.13a, the adiabatic gas temperature for the ID 9 trial was calculated to be 1844°C using the NASA CEA chemical equilibrium program. This value is close to the adiabatic temperature even with the direct injection of ethanol. It should also be noted that the mixture based solely on the ethanol spray was super fuel-rich (ϕ = 6.8). Even so, the temperature was sufficient for the synthesis of nanoparticles using the tubular flame. In the axial downstream direction (Figure 4.13b, Z = 125 mm), the gas temperature for ϕ_{total} = 0.88 exceeded 1000°C at almost all measurement points because the cross-section was filled with hot burned gas. The maximum temperature of 1610°C was less than that at Z = 55 mm as a result of heat loss to the combustor wall. Figures 13a and b also present the gas temperatures for ϕ_{total} = 1.04, which exhibit a similar trend to the data for ϕ_{total} = 0.88. The maximum temperature at Z = 55 mm is low, possibly because of the exceedingly fuel-rich main spray flow (ϕ = 10 for the ethanol spray mixture), although

a temperature of 1790°C was obtained at Z = 125 mm. These results indicate that a highly stable main flame was obtained together with a high temperature environment when using a fuel-lean tubular flame, even during the direct injection of liquid fuels into the burner.

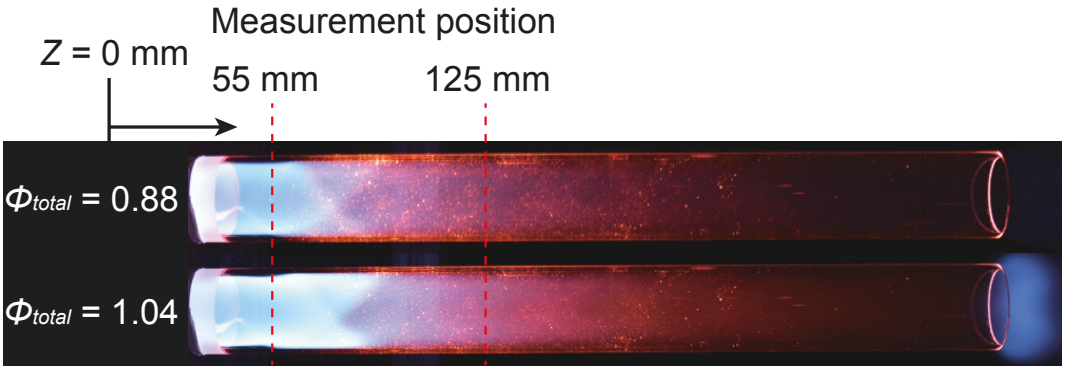

Figure 4.12: Flame appearance and temperature measurement positions for ϕ_{total} = 0.88 and 1.04.

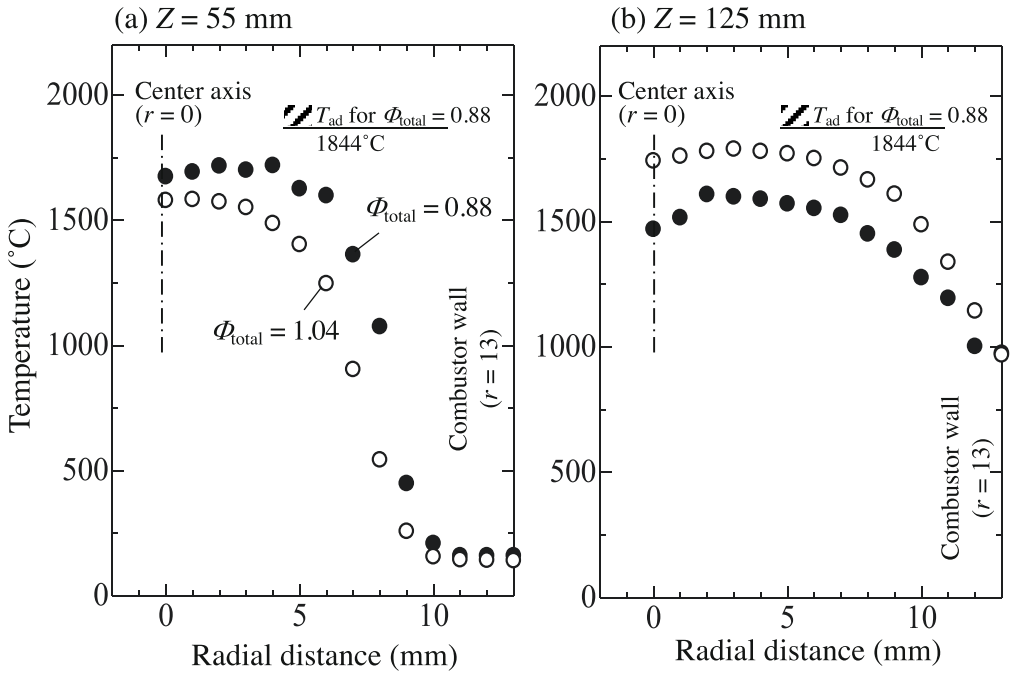

Figure 4.13: Radial distributions of gas temperatures at Z = (a) 55 and (b) 125 mm.

4.3.4 *Particle synthesis*

The TTIP or HMDSO precursors were dissolved in ethanol and subsequently sprayed into the tubular flame burner to produce TiO_2 or SiO_2 particles via flame aerosol syn-

thesis using the newly developed burner. Specifically, a 4 mL/min flow of the precursor solution was sprayed through the two-fluid nozzle and ignited. The combustion of this flow was sustained by the premixed tubular methane/air flame, under the conditions comprising Q_{CH_4} = 0.25 m³/h and Q_{air} = 4.0 m³/h (ID 9 in Table 4.1). When fine particles are produced using tubular flames, the equivalent ratio influences the chemical composition of the synthesized particles [123]. Under fuel-lean combustion conditions, the presence of excess oxygen accelerates the oxidation reaction, resulting in formation of oxide particles. In the case of fuel-rich combustion conditions, an ultralow O_2 atmosphere can be achieved in the combustion gas region, and the reduction reaction of fine particles is promoted by the presence of reducing gases such as CO and H_2. In this study, the total equivalent ratio was set to the fuel-lean condition because the aim was to synthesize oxide particles.

Both the precursor droplets using TTIP and HMDSO were processed into dry fine particles using the high-temperature field (above 1700°C, see Section 3.3) of stable spray combustion with the assistance of a tubular flame. The morphologies of the resulting particles were examined by SEM. Figure 4.14a shows an image of the TiO_2 particles, which were spherical and primarily had sub-micrometer sizes. In contrast, the SiO_2 particles shown in Figure 4.14a were aggregated, although the primary particle sizes were in the range of 20–30 nm. During liquid-fed aerosol synthesis, the formation of particles proceeds by both droplet-to-particle and gas-to-particle conversion processes [7, 32, 73]. Gas-to-particle conversion leads to the production of nanoparticles via nucleation and growth by coagulation and coalescence in the gas phase, while droplet-to-particle conversion forms submicron-sized particles by precursor precipitation inside the droplets in conjunction with various reactions. Figure 4.14b shows the XRD patterns of the obtained particles. The pattern of flame-made TiO_2 indicates that these particles had two TiO_2 crystal structures: rutile (COD no. 9007531) and anatase (COD no. 9009086). By contrast, the broad diffuse halo in the XRD pattern of the SiO_2 particles indicates the presence of a mostly amorphous material.

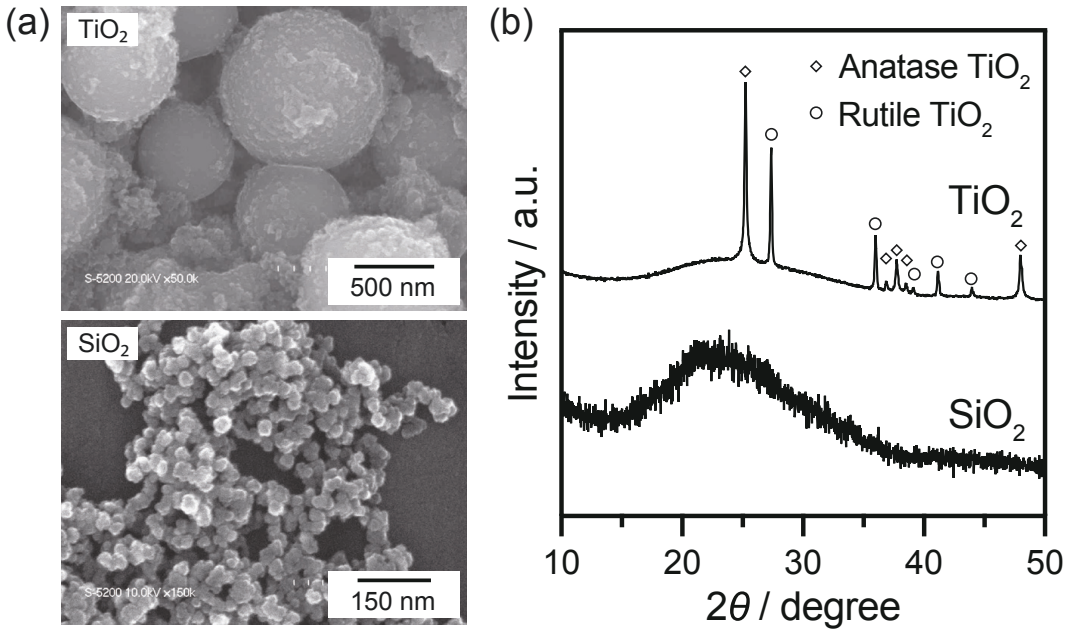

Figure 4.14: SEM images (a) and XRD patterns (b) of TiO_2 and SiO_2 particles generated in the flame.

4.4 CONCLUSIONS

A novel spray combustion process was developed, assisted by a tubular flame with a liquid fuel axially injected by a two-fluid nozzle and mixed with subsequent combustion in a tubular flame burner. This technique was employed to synthesize TiO_2 and SiO_2 particles. The following conclusions were made based on the present results.

1. A stable, homogeneous flame can be established using an axially sprayed liquid fuel and a tangentially injected pilot fuel and air mixture over a wide range of total equivalence ratios.

2. A spray flame can be obtained without a pilot fuel. However, the flame shape is not tubular but rather becomes conical as ϕ_{total} is decreased from 1.0. Nevertheless, stable combustion can be obtained when using a strong swirl flow.

3. The base of the main flame is greatly stabilized when the mixture used to produce the tubular flame is in the flammable range.

4. The radial temperature distribution of the flame established in the newly developed burner has an M shape during the combustion of premixed gases and the temperature near the burner wall is maintained at a low temperature because of the self-cooling effect of unburned gases.

5. TiO_2 or SiO_2 particles can be successfully synthesized in this burner and the XRD patterns of the as-prepared TiO_2 particles indicate rutile and anatase phases.

AKNOWLEDGEMENTS

This work was supported by JSPS KAKENHI grants (nos. JP20J20823 (T.H.) and JP19H02500 (T.O.)). This work is partly supported by the Center for Functional Nano Oxide at Hiroshima University, International Network on Polyoxometalate Science, JSPS Core-to-Core Program, The Information Center of Particle Technology, Japan, Hosokawa Powder Technology Foundation, the Foundation for the Promotion of Industrial Explosives Technology, and the Kato Foundation for the Promotion of Science (grant no. KS-3229). The SEM observations were performed at the Natural Science Center for Basic Research and Development (N-BARD), Hiroshima University.

5

CONCLUSIONS AND FUTURE PERSPECTIVES

Combustion-based particle synthesis is not only a method for industrial mass production of nanoparticle materials such as carbon black and titanium dioxide, but has significant potential as a fabrication technique for various functional particles and nanodevices. Tubular flame combustion allows precise control of the flame temperature and combustion gas composition owing to its thermal and aerodynamic advantages. In this dissertation, we evaluated the effect of the combustion characteristics of the tubular flame on particle properties, aiming to demonstrate the first application of tubular flames as a reaction field for particle synthesis. A summary of this study is given below.

1. For the first time, WO_3 nanoparticles were synthesized using tubular flame combustion. To synthesize WO_3 nanoparticles using a flame method, the gasification of WO_3 must be induced. Therefore, a high calorific value, i.e., a high flow rate of fuel gas, must be used for combustion. For tubular flames, the conductive heat loss is negligible, and an almost adiabatic flame temperature can be achieved. We successfully synthesized WO_3 nanoparticles by introducing an aerosol of ammonium tungstate solution generated by ultrasonic atomization into a tubular flame combustor and burning it. The particle size of WO_3 could be controlled in the nano to submicron range by adjusting the residence time in the tubular flame. A comparison test using a Bunsen flame was conducted, and it was found that the tubular flame had a high thermal advantage.

2. Metal tungsten nanoparticles were synthesized using fuel-rich tubular flame combustion. Because the flame aerosol process uses the combustion reaction (oxidation reaction) of materials, oxide particles are generally obtained. The tubular flame can precisely control the combustion gas composition because of its high combustion efficiency. Here, we successfully synthesized tungsten metal nanoparticles using tubular flame combustion with excess fuel to achieve a high concentration of reducing gas and a non-oxygen atmosphere. The oxygen and CO concentrations in the combustion gas were directly measured, and the optimum equivalence ratio conditions were determined. It was shown that the synthesis atmosphere could be controlled by adjusting the equivalence ratio, and the degree of tungsten oxidation could be controlled.

3. A tubular flame burner for particle synthesis that can combust liquid fuels was fabricated. The synthesis process that can use various states of raw materials enriches the variety of the materials synthesized and contributes to reducing the cost of the prepared particles. Here, we fabricated a new tubular flame burner that can supply flammable liquid from the axial direction of the tubular flame and determined the characteristics of the flame formed. The tubular flame

had high stability, which enabled stable combustion and particle synthesis, even when the liquid was sprayed from the axial direction. In addition, the detailed flame structure was revealed by the direct observation of flames and spectral analysis of chemiluminescence, and the optimum conditions for the formation of the tubular flame were determined.

Since its discovery in 1984 [47], the tubular flame has not only been used as a new flame element in cylindrical systems for fundamental combustion studies, but has also been applied to various practical combustors. However, its application to the field of particle synthesis is still in the early stages, and further development is required experimentally, theoretically, and computationally. The development of particle synthesis using tubular flame combustion requires focus on the following points.

1. Particle Spheroidization:

   Powder materials widely used in industry are required to have spherical morphology to improve fluidity, reduce equipment damage during transportation, and improve packing efficiency. For this reason, a flame or plasma process is used for the spheroidization of particles. However, the temperatures of flames and plasmas are difficult to control, and the molten materials coalesce in the high-temperature gas phase to form spherical particles of micron size or larger. Tubular flames allow precise control of the flame temperature so that spheroidization can be performed at a temperature that matches the melting point of the material, and the properties of the spherical particles can be controlled.

2. Two-stage Combustion in a Tubular Flame Burner:

   The tubular flame can be easily incorporated into various processes because of its tubular shape and high stability. By incorporating the tubular flame downstream of various continuous gas-phase synthesis processes, such as spray pyrolysis, CVD, plasma, and flame processes, it is possible to functionalize particles in the vapor phase. Specifically, synthesis of core-shell particles, reduction, spheroidization, and exhaust gas cleaning are expected to be possible. Furthermore, because the tubular flame is formed in a swirling flow, the particles in the flame are mixed with the gas, and uniform target particles can be obtained.

3. Tubular Flame Annealing:

   Recently, flame annealing and its combination with liquid-phase synthesis (sol-flame synthesis) have been developed [124–130]. Particles and films obtained by various synthesis methods are often subjected to calcination in an electric furnace to improve purity and sintering. However, sintering in an electric furnace requires a long calcination time, which leads to higher costs. The flame can instantly provide a high temperature to supply high energy to the material in a short time. By applying a tubular flame to the flame annealing process, the flame temperature and combustion gas composition, which are difficult to control, can be managed, and the material properties can be more closely controlled.

A

SUPPORTING INFORMATION: TUBULAR FLAME COMBUSTION FOR NANOPARTICLE PRODUCTION

A.1 STRUCTURE OF A TUBULAR FLAME FOR NANOPARTICLE PRODUCTION

Figure A.1 shows detail of the tubular flame used for nanoparticle synthesis. As shown in Figure A.1 left, a laminar tubular flame front can be established in the burner, in which the inner region is filled by combusted gas and the outer region is surrounded by non-combusted gas. In Figure A.1 right, an image of the tubular flame established inside the burner is illustrated. A tubular flame front is established near the tangential inlets (Tubular flame; Figure A.1, right); however, the visible tubular flame front ends when the whole unburned mixture is consumed (End of the visible flame; Figure A.1, right), and the axially downstream region of the flame is filled with combusted gas.

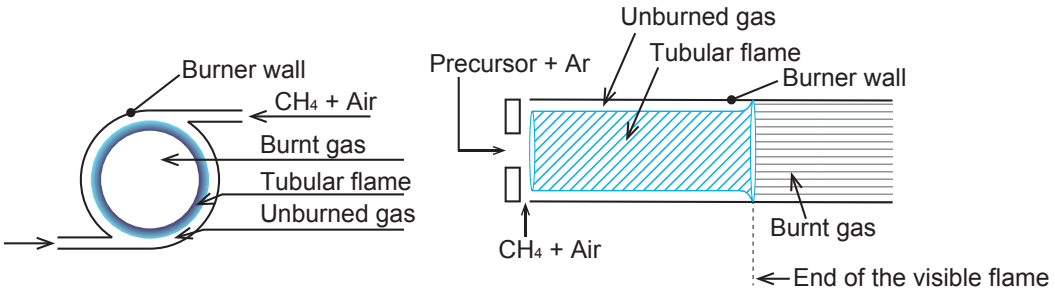

Figure A.1: Schematic diagram of the structure of a tubular flame for nanoparticle production.

A.2 STRUCTURE OF A TUBULAR FLAME BURNER

Figure A.2 shows detail of a tubular flame burner used in this study.

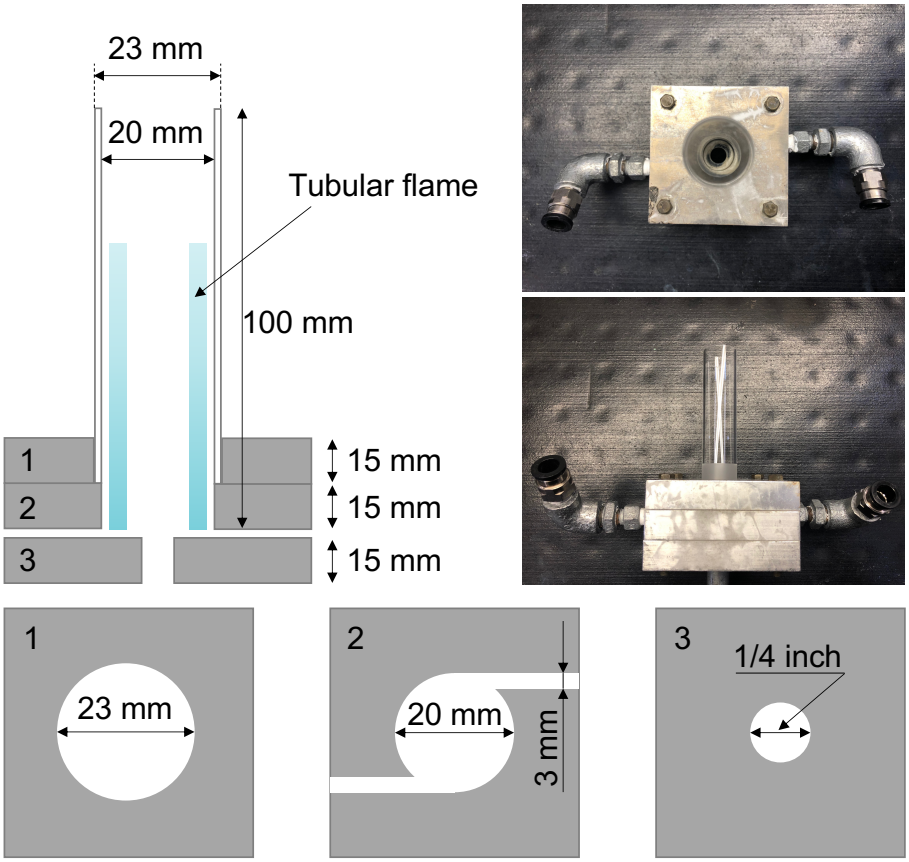

Figure A.2: Structure of a tubular flame burner.

A.3 TEMPERATURE DISTRIBUTION OF TUBULAR FLAME

The temperature distribution of tubular flame was directly measured using a thermocouple. As shown in Figure A.3, the maximum temperature of 1623°C were obtained when the Qc = 0.1 m^3/h at Z = 20 mm. When Ar (carrier) gas of 0.1 m^3/h at 20°C is heated by combustion gas (CH_4 flow rate: 0.1 m^3/h, Air flow rate: 0.95, adiabatic flame temperature: 1954°C), the mean temperature is 1888°C. The measured temperature and its correction were reasonable considering heat losses to quartz glass tube and burner exit. The temperature at the point where the precursor passes through the tubular flame (r = 0, 1, 2, 3 mm) tended to decrease as Q_C increased.

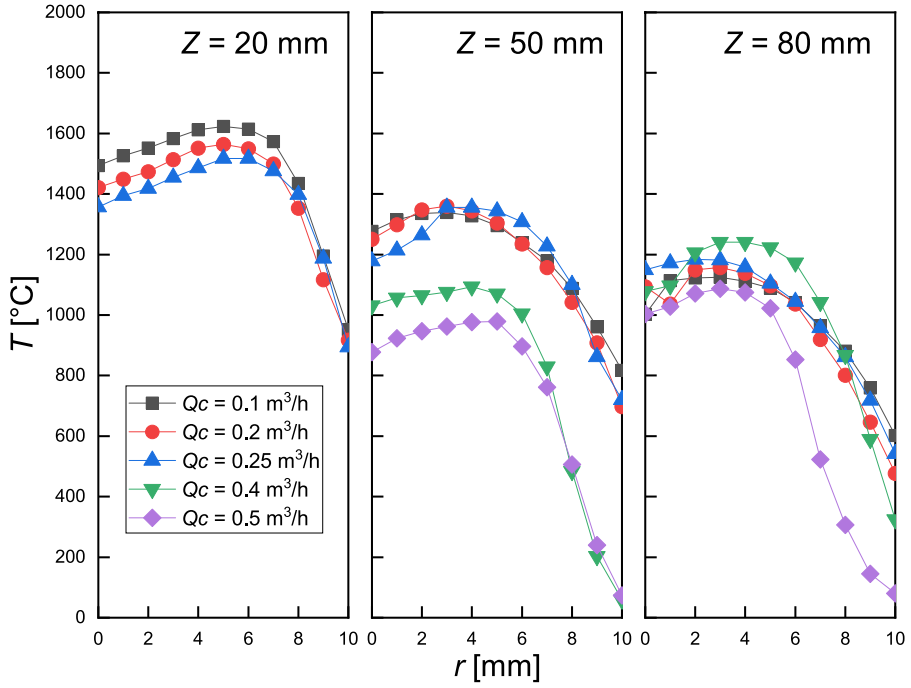

Figure A.3: Temperature distribution of tubular flame at various carrier gas flow rates.

A.4 TEM IMAGES OF TUBULAR FLAME-MADE WO_3 PARTICLES

TEM images of WO_3 particles made in tubular flame at different Q_C are depicted in Figure A.4.

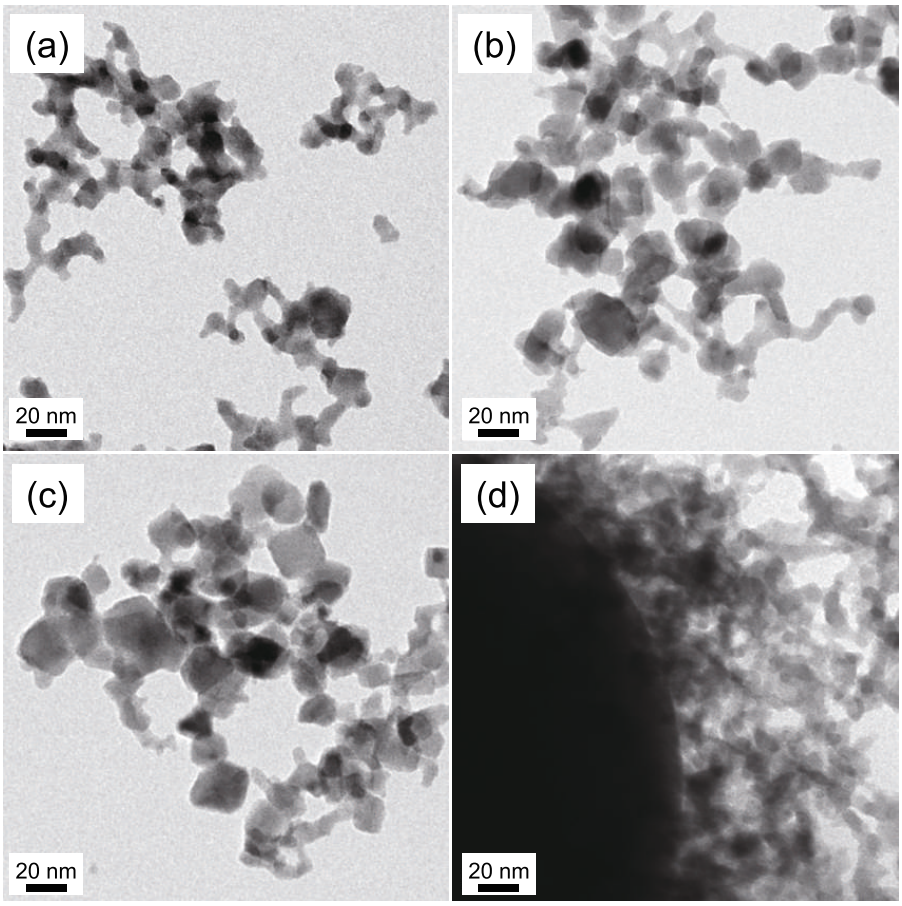

Figure A.4: TEM images of tubular flame-made WO_3 particles at Q_C = (a) 0.1, (b) 0.2, (c) 0.3, (d) 0.5 m^3/h.

A.5 STRUCTURE OF A BUNSEN BURNER

Figure A.5 shows detail of a Bunsen burner used in this study for comparison of tubular flame.

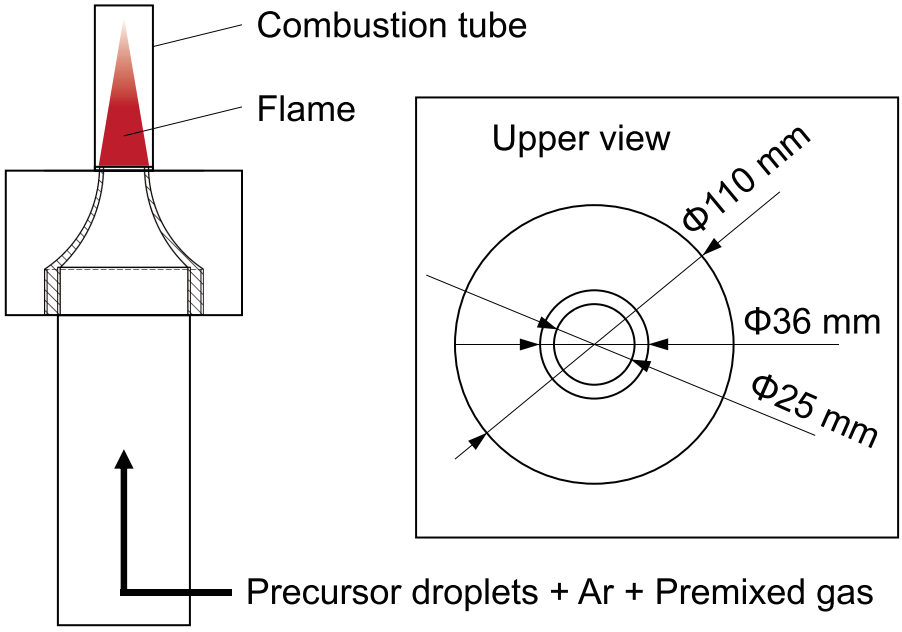

Figure A.5: Structure of a Bunsen burner.

A.6 XRD PATTERNS OF BUNSEN AND TUBULAR FLAME-MADE WO_3 PARTICLES

The XRD patterns of Bunsen and tubular flame-made WO_3 particles are depicted in Figure A.6.

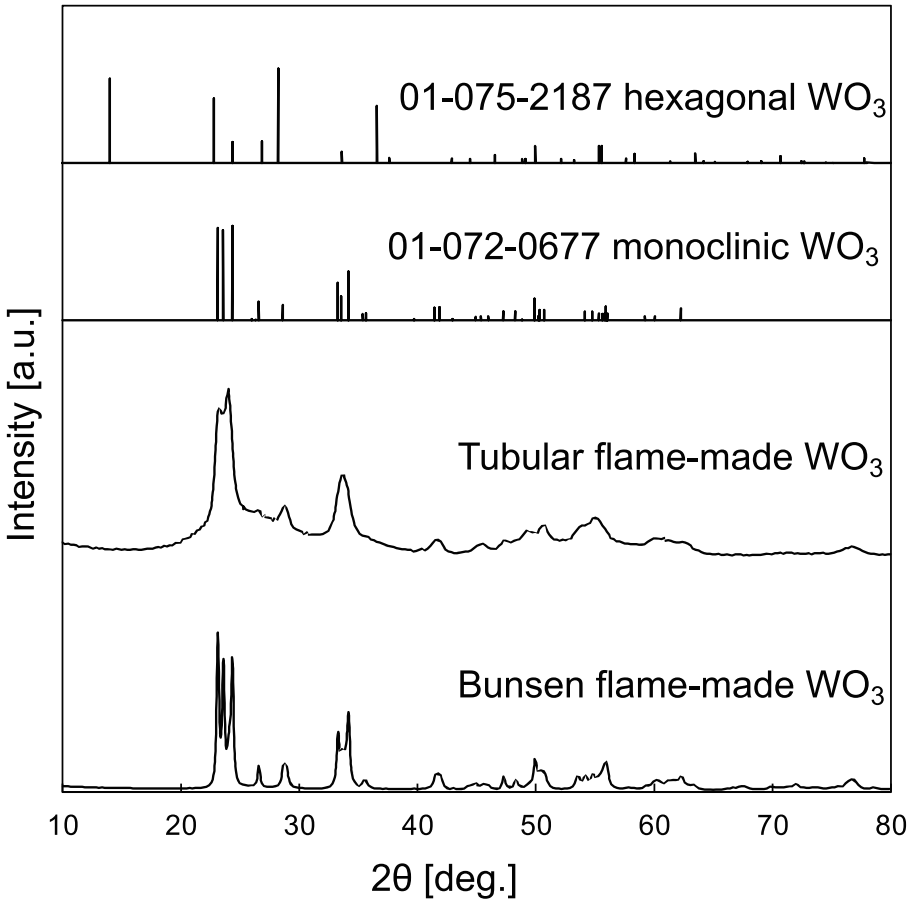

Figure A.6: XRD patterns of Bunsen and tubular flame-made WO_3 particles.

B

SUPPORTING INFORMATION: UTILIZATION OF INNER REDUCING GAS REGION OF TUBULAR FLAMES

B.1 CONVENTIONAL FLAME-ASSISTED SPRAY PYROLYSIS SYSTEM

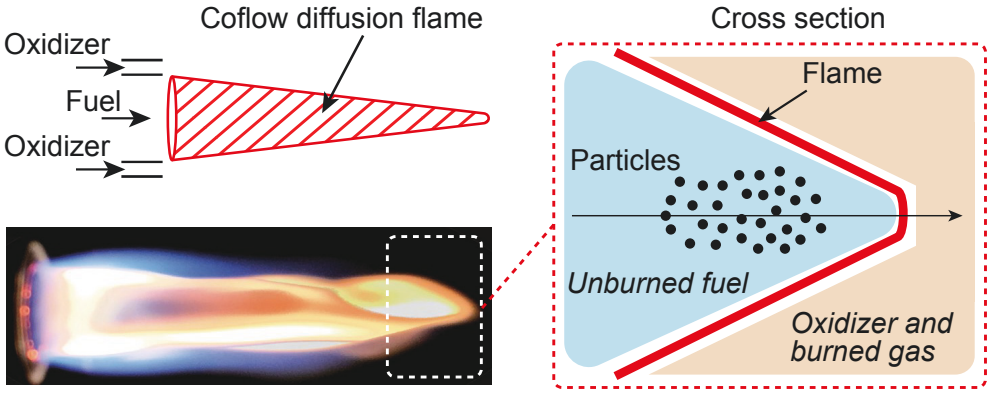

Figure B.1: Schemes illustrating conventional flame-assisted spray pyrolysis system.

B.2 TUBULAR FLAME BURNER

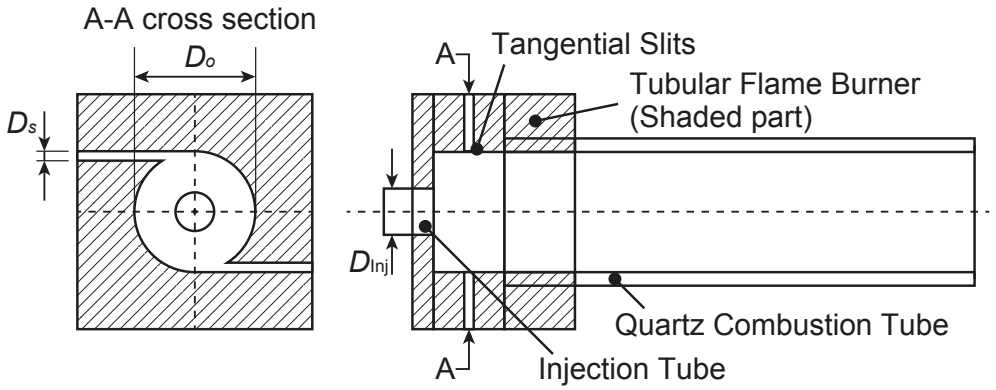

Figure B.2: Schematic diagram of tubular flame burner used in this study.

B.3 SWIRL NUMBERS

An important parameter that can affect flame characteristics, and hence the synthesis of tungsten nanoparticles, is the swirl intensity. Swirl flow enhances the flame stability, and creates uniform distributions of gaseous temperature and concentration. The swirl number, which is defined by the following equation, is a measure of the swirl intensity:

$$\begin{aligned} S_W &= \frac{Angular\ momentum}{Translational\ motion \times R_b} \\ &= \frac{\left(\rho_{CH_4} Q_{CH_4} w_{CH_4} + \rho_{Air} Q_{Air} w_{Air}\right) A_b}{\left(\rho_{CH_4} Q_{CH_4} + \rho_{Air} Q_{Air} + \rho_C Q_C\right)\left(Q_{CH_4} + Q_{Air} + Q_C\right)} \end{aligned} \tag{2}$$

where R_b is the burner radius [m], ρ is the density [kg/m^3], Q is the volumetric flow rate [m^3/h], w is the velocity [m/h], and A_b is the cross-sectional area of the combustion tube [m^2]. The parameter S_W corresponds to the intensity of the swirl flow and is derived from the angular momentum to translational momentum ratio. Increases in the flow rates of tangential air and CH_4 increase S_W, whereas an increase in the axially supplied carrier gas flow rate decreases S_W. Figure B-3a and b show that S_W exceeded 0.60 under all the experimental conditions used. This indicates that a strong swirl flow formed inside the tubular flame burner. Figure A.3b shows that an increase in the carrier gas flow rate from 0.05 to 0.20 greatly decreased S_W, from 30 to 17, i.e., when Q_C = 0.20, the mixture was highly diluted and the swirl intensity was weak. Even under such conditions, a stable tubular flame can be formed inside the burner, as shown in Figure B.3b. The tubular flame is therefore stable enough for tungsten nanoparticle synthesis, even when the inert carrier gas flow rate is high.

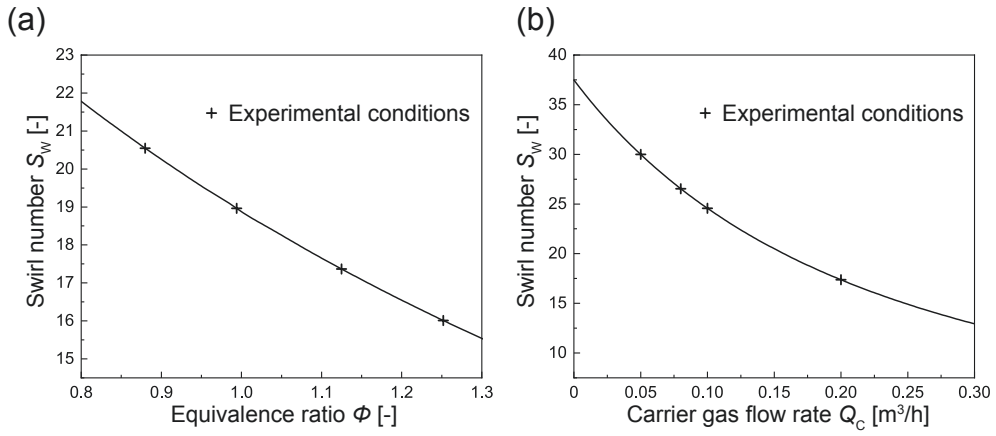

Figure B.3: Swirl numbers for various equivalence ratios (a) and carrier gas flow rates (b).

B.4 FLAME APPEARANCES WITHOUT CARRIER GAS

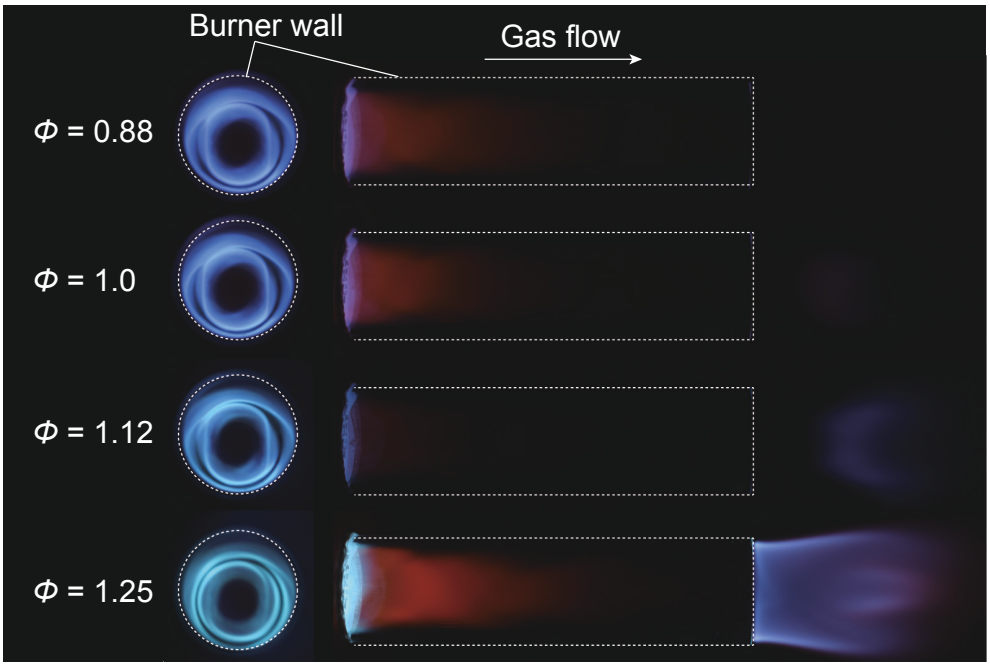

Figure B.4: Flame appearances at various equivalence ratios without carrier gas. Tubular flames can be established under all conditions.

B.5 EQUILIBRIUM CONCENTRATIONS OF COMBUSTION GAS

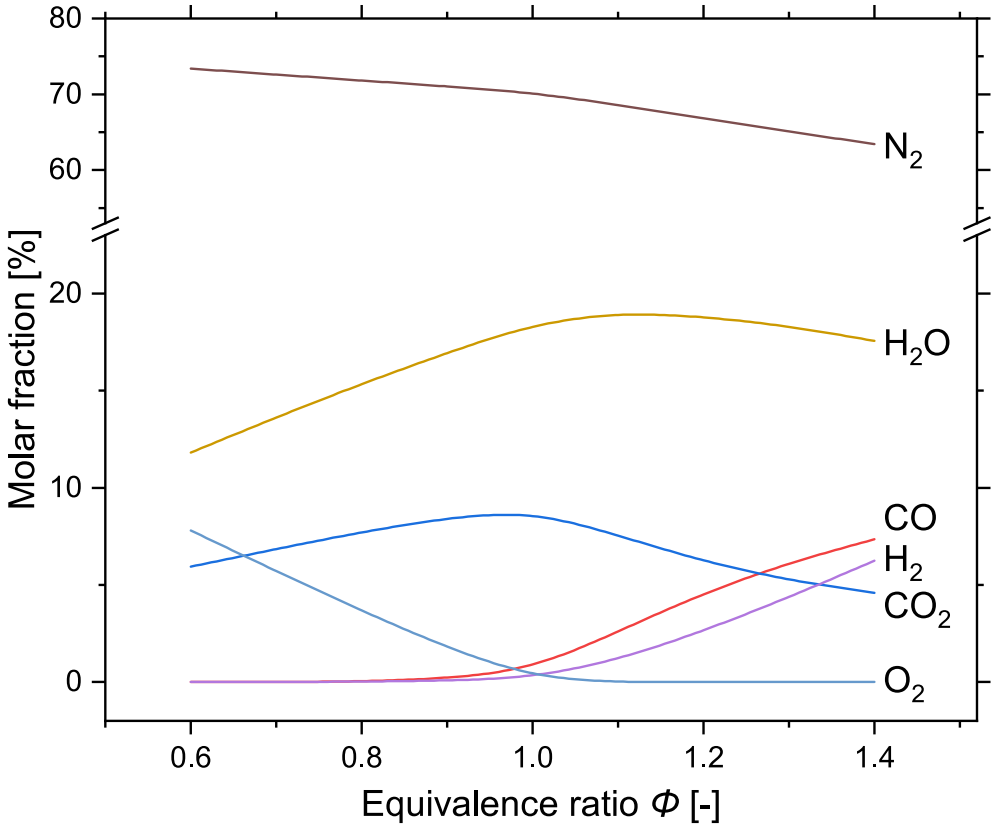

Figure B.5: Equilibrium concentrations of major gaseous combustion products. At $\phi > 1$, hydrogen is considered to be present in the combustion gas as a reducing gas in addition to CO.

B.6 SEM IMAGES OF PARTICLES PRODUCED AT VARIOUS EQUIVALENCE RATIOS

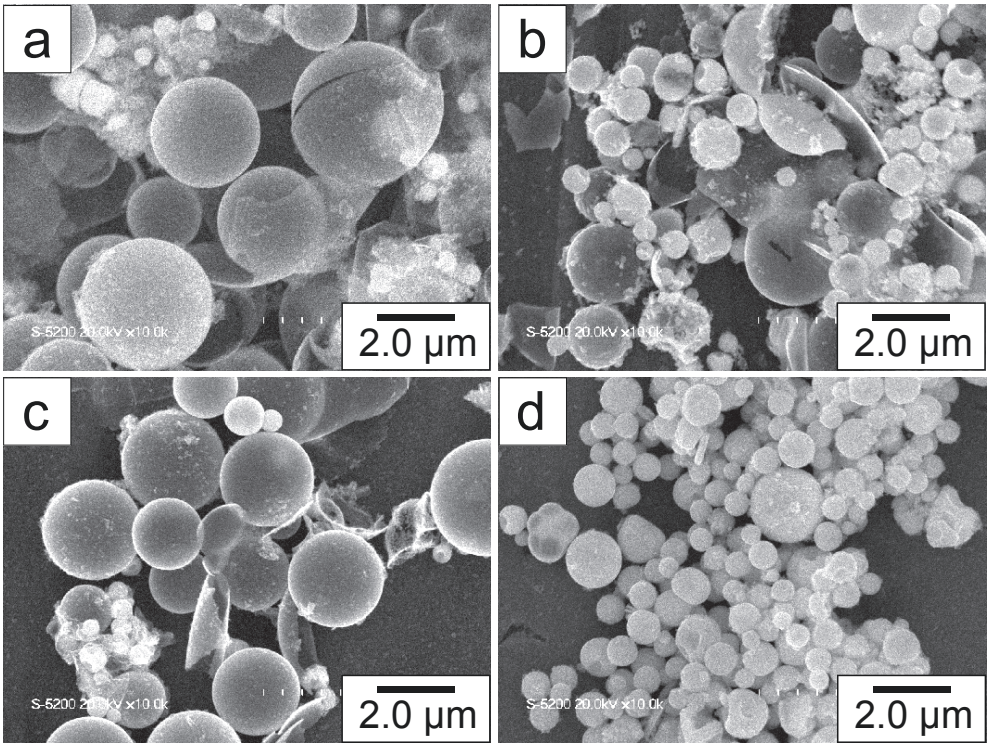

Figure B.6: SEM images of particles produced at various equivalence ratios: ϕ = (a) 1.25, (b) 1.12, (c) 1.0, and (d) 0.9.

B.7 TEM IMAGES AND PARTICLE SIZE DISTRIBUTION

Additional TEM images of sample no. 7 are shown in Figure B.7. The size distribution was determined by counting 310 particles. The geometric mean diameter and geometric standard deviation are 9.24 nm and 1.30, respectively.

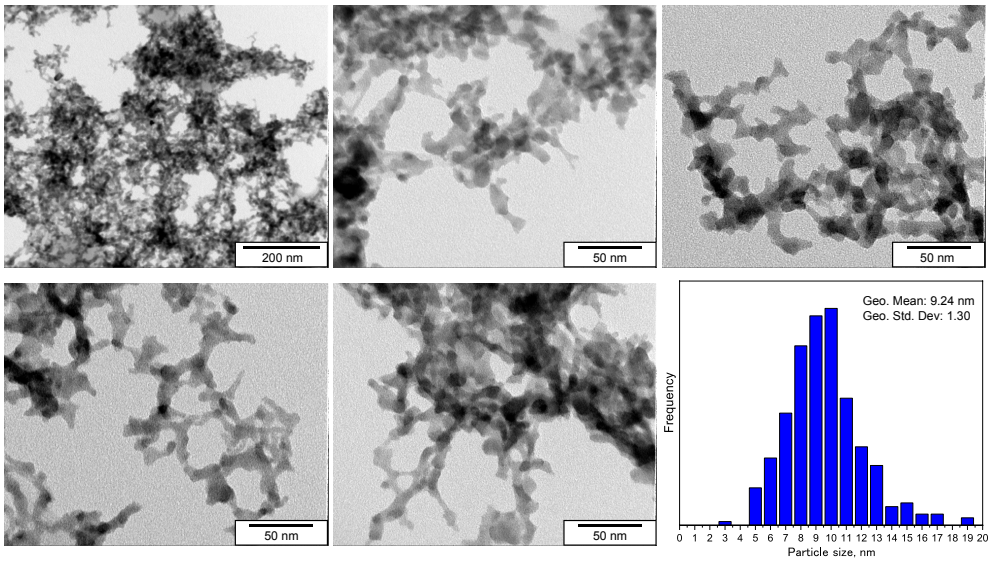

Figure B.7: TEM images and particle size distribution of sample no. 7.

B.8 XPS SPECTRA WITHOUT AR^+ ETCHING

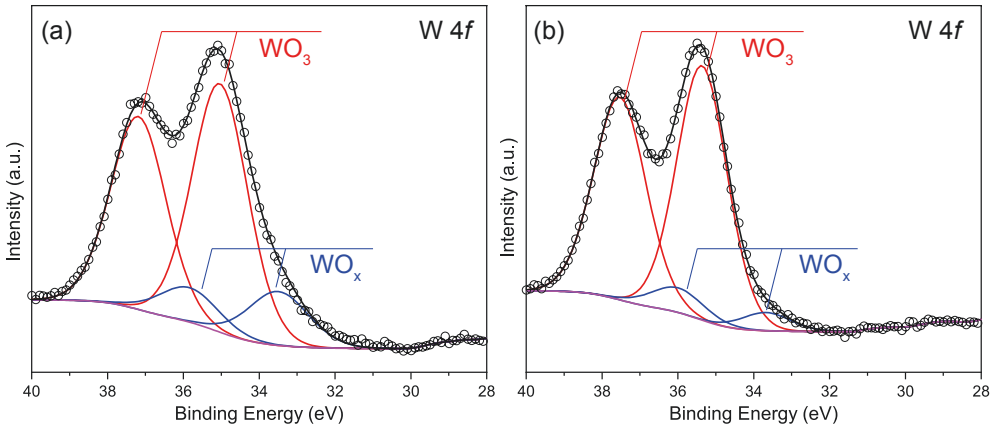

Figure B.8: XPS spectra of (a) tungsten oxide particles (sample no. 1) and (b) mixtures of tungsten metal and oxide nanoparticles (sample no. 7) produced in tubular flames without Ar^+ etching.

BIBLIOGRAPHY

[1] Pratsinis SE. Flame aerosol synthesis of ceramic powders. *Progress in Energy and Combustion Science*. 1998;24(3):197–219.

[2] Kammler HK, Madler L, Pratsinis SE. Flame synthesis of nanoparticles. *Chemical Engineering and Technology*. 2001;24(6):583–596.

[3] Stark WJ, Pratsinis SE. Aerosol flame reactors for manufacture of nanoparticles. *Powder Technology*. 2002;126(2):103–108.

[4] Strobel R, Pratsinis SE. Flame aerosol synthesis of smart nanostructured materials. *Journal of Materials Chemistry*. 2007;17(45):4743–4756.

[5] Athanassiou EK, Grass RN, Stark WJ. Chemical Aerosol Engineering as a Novel Tool for Material Science: From Oxides to Salt and Metal Nanoparticles. *Aerosol Science and Technology*. 2010;44(2):161–172.

[6] Teoh WY, Amal R, Madler L. Flame spray pyrolysis: An enabling technology for nanoparticles design and fabrication. *Nanoscale*. 2010;2(8):1324–47.

[7] Koirala R, Pratsinis SE, Baiker A. Synthesis of catalytic materials in flames: opportunities and challenges. *Chem Soc Rev*. 2016;45(11):3053–68.

[8] Li S, Ren Y, Biswas P, Tse SD. Flame aerosol synthesis of nanostructured materials and functional devices: Processing, modeling, and diagnostics. *Progress in Energy and Combustion Science*. 2016;55:1–59.

[9] Salameh S, Gómez-Hernández J, Goulas A, Van Bui H, van Ommen JR. Advances in scalable gas-phase manufacturing and processing of nanostructured solids: A review. *Particuology*. 2017;30:15–39.

[10] Pokhrel S, Madler L. Flame-made Particles for Sensors, Catalysis, and Energy Storage Applications. *Energy Fuels*. 2020;34(11):13209–13224.

[11] Ding S, Chen HA, Mekasuwandumrong O, Hülsey MJ, Fu X, He Q, Panpranot J, Yang CM, Yan N. High-temperature flame spray pyrolysis induced stabilization of Pt single-atom catalysts. *Applied Catalysis B: Environmental*. 2021;281:119471.

[12] Jiang J, Lei J, Hu Y, Bi W, Xu N, Li Y, Chen X, Jiang H, Li C. Electron transfer effect from Au to Pt in Au-Pt/TiO_2 towards efficient catalytic activity in CO oxidation at low temperature. *Applied Surface Science*. 2020;521:146447.

[13] Saito K, Yi E, Laine RM, Sugahara Y. Preparation of Nb-doped TiO_2 nanopowder by liquid-feed spray pyrolysis followed by ammonia annealing for tunable visible-light absorption and inhibition of photocatalytic activity. *Ceramics International*. 2020;46(2):1314–1322.

[14] Tada S, Larmier K, Büchel R, Copéret C. Methanol synthesis via CO_2 hydrogenation over CuO–ZrO_2 prepared by two-nozzle flame spray pyrolysis. *Catalysis Science & Technology*. 2018;8(8):2056–2060.

[15] Fujiwara K, Deligiannakis Y, Skoutelis CG, Pratsinis SE. Visible-light active black TiO_2-Ag/TiO_x particles. *Applied Catalysis B: Environmental*. 2014;154:9–15.

[16] Okada Y, Mizutori A, Yamaoka D. Formation of Non-Aggregated $Li_4Ti_5O_{12}$ Particles in a Flame Reactor. *Earozoru Kenkyu*. 2017;32(1):52–57.

[17] Okada Y, Kawamura H, Ozaki H. Formation of Non-Agglomerated Titania Nanoparticles in a Flame Reactor. *Journal of Chemical Engineering of Japan*. 2011; 44(1):7–13.

[18] Van den Broek J, Abegg S, Pratsinis SE, Güntner A. Highly selective detection of methanol over ethanol by a handheld gas sensor. *Nature communications*. 2019; 10(1):1–8.

[19] Kemmler JA, Pokhrel S, Madler L, Weimar U, Barsan N. Flame spray pyrolysis for sensing at the nanoscale. *Nanotechnology*. 2013;24(44):442001.

[20] Gockeln M, Glenneberg J, Busse M, Pokhrel S, Mädler L, Kun R. Flame aerosol deposited $Li_4Ti_5O_{12}$ layers for flexible, thin film all-solid-state Li-ion batteries. *Nano Energy*. 2018;49:564–573.

[21] Gockeln M, Pokhrel S, Meierhofer F, Glenneberg J, Schowalter M, Rosenauer A, Fritsching U, Busse M, Mädler L, Kun R. Fabrication and performance of $Li_4Ti_5O_{12}$/C Li-ion battery electrodes using combined double flame spray pyrolysis and pressure-based lamination technique. *Journal of Power Sources*. 2018; 374:97–106.

[22] Yuan Y, Li S, Yao Q. Dynamic behavior of sodium release from pulverized coal combustion by phase-selective laser-induced breakdown spectroscopy. *Proceedings of the Combustion Institute*. 2015;35(2):2339–2346.

[23] Ren Y, Zhang Y, Li S, Law CK. Doping mechanism of Vanadia/Titania nanoparticles in flame synthesis by a novel optical spectroscopy technique. *Proceedings of the Combustion Institute*. 2015;35(2):2283–2289.

[24] Zhang Y, Xiong G, Li S, Dong Z, Buckley SG, Tse SD. Novel low-intensity phase-selective laser-induced breakdown spectroscopy of TiO_2 nanoparticle aerosols during flame synthesis. *Combustion and Flame*. 2013;160(3):725–733.

[25] Gröhn AJ, Pratsinis SE, Wegner K. Fluid-particle dynamics during combustion spray aerosol synthesis of ZrO_2. *Chemical Engineering Journal*. 2012;191:491–502.

[26] Zhang Y, Li S, Ren Y, Yao Q, Law CK. Two-dimensional imaging of gas-to-particle transition in flames by laser-induced nanoplasmas. *Applied Physics Letters*. 2014;104(2):023115.

[27] Cignoli F, Bellomunno C, Maffi S, Zizak G. Laser-induced incandescence of titania nanoparticles synthesized in a flame. *Applied Physics B*. 2009;96(4):593–599.

[28] Camenzind A, Schulz H, Teleki A, Beaucage G, Narayanan T, Pratsinis SE. Nanostructure Evolution: From Aggregated to Spherical SiO_2 Particles Made in Diffusion Flames. *European Journal of Inorganic Chemistry*. 2008;2008(6):911–918.

[29] Engel SR, Koegler AF, Gao Y, Kilian D, Voigt M, Seeger T, Peukert W, Leipertz A. Gas phase temperature measurements in the liquid and particle regime of a flame spray pyrolysis process using O_2-based pure rotational coherent anti-Stokes Raman scattering. *Appl Opt*. 2012;51(25):6063–75.

[30] Sokolowski M, Sokolowska A, Michalski A, Gokieli B. The "in-flame-reaction" method for Al_2O_3 aerosol formation. *Journal of Aerosol Science*. 1977;8(4):219–230.

[31] Purwanto A, Wang WN, Ogi T, Lenggoro IW, Tanabe E, Okuyama K. High luminance YAG:Ce nanoparticles fabricated from urea added aqueous precursor by flame process. *Journal of Alloys and Compounds*. 2008;463(1-2):350–357.

[32] Hirano T, Nakakura S, Rinaldi FG, Tanabe E, Wang WN, Ogi T. Synthesis of highly crystalline hexagonal cesium tungsten bronze nanoparticles by flame-assisted spray pyrolysis. *Advanced Powder Technology*. 2018;29(10):2512–2520.

[33] Mädler L, Kammler H, Mueller R, Pratsinis SE. Controlled synthesis of nanostructured particles by flame spray pyrolysis. *Journal of Aerosol Science*. 2002;33(2):369–389.

[34] Hirano T, Tsuboi T, Tanabe E, Ogi T. In-situ flame deposition of Pt catalysts on Nb-doped SnO_2 nanoparticles. *Journal of Alloys and Compounds*. 2021;p. 162749.

[35] Teleki A, Pratsinis SE. Blue nano titania made in diffusion flames. *Physical Chemistry Chemical Physics*. 2009;11(19):3742–3747.

[36] Grass RN, Stark WJ. Flame synthesis of calcium-, strontium-, barium fluoride nanoparticles and sodium chloride. *Chemical Communications*. 2005;(13):1767–1769.

[37] Grass RN, Stark WJ. Flame spray synthesis under a non-oxidizing atmosphere: Preparation of metallic bismuth nanoparticles and nanocrystalline bulk bismuth metal. *Journal of Nanoparticle Research*. 2006;8(5):729–736.

[38] Grass RN, Stark WJ. Gas phase synthesis of fcc-cobalt nanoparticles. *Journal of Materials Chemistry*. 2006;16(19):1825–1830.

[39] Herrmann IK, Grass RN, Mazunin D, Stark WJ. Synthesis and Covalent Surface Functionalization of Nonoxidic Iron Core-Shell Nanomagnets. *Chemistry of Materials*. 2009;21(14):3275–3281.

[40] Döbelin N, Brunner TJ, Stark WJ, Fisch M, Conforto E, Bohner M. Thermal treatment of flame-synthesized amorphous tricalcium phosphate nanoparticles. *Journal of the American Ceramic Society*. 2010;93(10):3455–3463.

[41] Strobel R, Mädler L, Piacentini M, Maciejewski M, Baiker A, Pratsinis SE. Two-Nozzle Flame Synthesis of $Pt/Ba/Al_2O_3$ for NO_x Storage. *Chemistry of materials*. 2006;18(10):2532–2537.

[42] Teleki A, Heine MC, Krumeich F, Akhtar MK, Pratsinis SE. In situ coating of flame-made TiO_2 particles with nanothin SiO_2 films. *Langmuir*. 2008; 24(21):12553–12558.

[43] Blattmann CO, Pratsinis SE. Single-step fabrication of polymer nanocomposite films. *Materials*. 2018;11(7):1177.

[44] Mädler L, Roessler A, Pratsinis SE, Sahm T, Gurlo A, Barsan N, Weimar U. Direct formation of highly porous gas-sensing films by in situ thermophoretic deposition of flame-made Pt/SnO_2 nanoparticles. *Sensors and Actuators B: Chemical*. 2006;114(1):283–295.

[45] Schopf SO, Salameh S, Mädler L. Transfer of highly porous nanoparticle layers to various substrates through mechanical compression. *Nanoscale*. 2013;5(9):3764–3772.

[46] Zhang Y, Li S, Ren Y, Yao Q, Stephen DT. A new diagnostic for volume fraction measurement of metal-oxide nanoparticles in flames using phase-selective laser-induced breakdown spectroscopy. *Proceedings of the Combustion Institute*. 2015; 35(3):3681–3688.

[47] Ishizuka S. On the behavior of premixed flames in a rotating flow field: Establishment of tubular flames. *Symposium (International) on Combustion*. 1984; 20(1):287–294.

[48] Ishizuka S. Characteristics of tubular flames. *Progress in Energy and Combustion Science*. 1993;19(3):187–226.

[49] Ishizuka S, Dunn-Rankin D. *Tubular combustion*. Momentum Press. 2013.

[50] Hirano T, Ogi T. Tubular Flame Synthesis of Fine Particles. *Earozoru Kenkyu*. 2020;35(4):265–271.

[51] Zabetakis MG. Flammability characteristics of combustible gases and vapors. *Tech. rep.*, Bureau of Mines Washington DC. 1965.

[52] Okuyama K, Wuled Lenggoro I. Preparation of nanoparticles via spray route. *Chemical Engineering Science*. 2003;58(3-6):537–547.

[53] Ogi T, Nandiyanto ABD, Okuyama K. Nanostructuring strategies in functional fine-particle synthesis towards resource and energy saving applications. *Advanced Powder Technology*. 2014;25(1):3–17.

[54] Ogi T, Zulhijah R, Iwaki T, Okuyama K. Recent Progress in Nanoparticle Dispersion Using Bead Mill. *KONA Powder and Particle Journal*. 2017;34(0):3–23.

[55] McMillin BK, Biswas P, Zachariah MR. In situ characterization of vapor phase growth of iron oxide-silica nanocomposites: Part I. 2-D planar laser-induced fluorescence and Mie imaging. *Journal of Materials Research*. 1996;11(6):1552–1561.

[56] Guo B, Yim H, Khasanov A, Stevens J. Formation of magnetic Fe_xO_y/silica core-shell particles in a one-step flame aerosol process. *Aerosol Science and Technology*. 2010;44(4):281–291.

[57] Pratsinis SE, Zhu WH, Vemury S. The role of gas mixing in flame synthesis of titania powders. *Powder Technology*. 1996;86(1):87–93.

[58] Johannessen T, Pratsinis SE, Livbjerg H. Computational analysis of coagulation and coalescence in the flame synthesis of titania particles. *Powder Technology*. 2001;118(3):242–250.

[59] Hidayat D, Purwanto A, Wang WN, Okuyama K. Preparation of size-controlled tungsten oxide nanoparticles and evaluation of their adsorption performance. *Materials Research Bulletin*. 2010;45(2):165–173.

[60] Widiyandari H, Purwanto A, Balgis R, Ogi T, Okuyama K. CuO/WO_3 and Pt/WO_3 nanocatalysts for efficient pollutant degradation using visible light irradiation. *Chemical Engineering Journal*. 2012;180:323–329.

[61] Arutanti O, Nandiyanto ABD, Ogi T, Iskandar F, Kim TO, Okuyama K. Synthesis of composite WO_3/TiO_2 nanoparticles by flame-assisted spray pyrolysis and their photocatalytic activity. *Journal of Alloys and Compounds*. 2014;591:121–126.

[62] Arutanti O, Arif AF, Balgis R, Ogi T, Okuyama K, Iskandar F. Tailored synthesis of macroporous Pt/WO_3 photocatalyst with nanoaggregates via flame assisted spray pyrolysis. *Aiche Journal*. 2016;62(11):3864–3873.

[63] Mueller R, Mädler L, Pratsinis SE. Nanoparticle synthesis at high production rates by flame spray pyrolysis. *Chemical Engineering Science*. 2003;58(10):1969–1976.

[64] Fujiwara K, Pratsinis SE. Atomically dispersed Pd on nanostructured TiO_2 for NO removal by solar light. *AIChE Journal*. 2017;63(1):139–146.

[65] Ehrman SH, Friedlander SK, Zachariah MR. Characteristics of SiO_2/TiO_2 nanocomposite particles formed in a premixed flat flame. *Journal of Aerosol Science*. 1998;29(5-6):687–706.

[66] Bakrania SD, Miller TA, Perez C, Wooldridge MS. Combustion of multiphase reactants for the synthesis of nanocomposite materials. *Combustion and Flame*. 2007;148(1-2):76–87.

[67] Rayleigh L. On the dynamics of revolving fluids. *Proceedings of the Royal Society of London Series A, Containing Papers of a Mathematical and Physical Character*. 1917; 93(648):148–154.

[68] Righettoni M, Tricoli A, Pratsinis SE. Si:WO_3 Sensors for highly selective detection of acetone for easy diagnosis of diabetes by breath analysis. *Anal Chem*. 2010;82(9):3581–7.

[69] Hammond C, Straus J, Righettoni M, Pratsinis SE, Hermans I. Nanoparticulate Tungsten Oxide for Catalytic Epoxidations. *ACS Catalysis*. 2013;3(3):321–327.

[70] Arutanti O, Ogi T, Nandiyanto ABD, Iskandar F, Okuyama K. Controllable crystallite and particle sizes of WO_3 particles prepared by a spray-pyrolysis method and their photocatalytic activity. *AIChE Journal*. 2014;60(1):41–49.

[71] Nandiyanto ABD, Arutanti O, Ogi T, Iskandar F, Kim TO, Okuyama K. Synthesis of spherical macroporous WO_3 particles and their high photocatalytic performance. *Chemical Engineering Science*. 2013;101:523–532.

[72] Syred N, Beér JM. Combustion in swirling flows: A review. *Combustion and Flame*. 1974;23(2):143–201.

[73] Nakakura S, Arif AF, Rinaldi FG, Hirano T, Tanabe E, Balgis R, Ogi T. Direct synthesis of highly crystalline single-phase hexagonal tungsten oxide nanorods by spray pyrolysis. *Advanced Powder Technology*. 2019;30(1):6–12.

[74] Widiyastuti W, Hidayat D, Purwanto A, Iskandar F, Okuyama K. Particle dynamics simulation of nanoparticle formation in a flame reactor using a polydispersed submicron-sized solid precursor. *Chemical Engineering Journal*. 2010; 158(2):362–367.

[75] Widiyastuti W, Purwanto A, Wang WN, Iskandar F, Setyawan H, Okuyama K. Nanoparticle formation through solid-fed flame synthesis: Experiment and modeling. *AIChE Journal*. 2009;55(4):885–895.

[76] Kaskan W. The dependence of flame temperature on mass burning velocity. *Symposium (International) on Combustion*. 1957;6(1):134–143.

[77] Bird RB, Stewart WE, Lightfoot EN. *Transport phenomena*. John Wiley & Sons. 2006.

[78] Shimokuri D, Ishizuka S. Flame stabilization with a tubular flame. *Proceedings of the Combustion Institute*. 2005;30(1):399–406.

[79] Karlovitz B, Denniston Jr D, Knapschaefer D, Wells F. Studies on turbulent flames: A. flame propagation across velocity gradients b. turbulence measurement in flames. *Symposium (international) on combustion*. 1953;4(1):613–620.

[80] Williams GC, Hottel HC, Scurlock AC. Flame stabilization and propagation in high velocity gas streams. *Symposium on Combustion and Flame, and Explosion Phenomena*. 1948;3(1):21–40.

[81] Lewis B, Von Elbe G. *Combustion, flames and explosions of gases*. Elsevier. 2012.

[82] Lassner E, Schubert WD. *Tungsten: properties, chemistry, technology of the elements, alloys, and chemical compounds*. Springer Science & Business Media. 1999.

[83] Ogi T, Makino T, Okuyama K, Stark WJ, Iskandar F. Selective Biosorption and Recovery of Tungsten from an Urban Mine and Feasibility Evaluation. *Industrial and Engineering Chemistry Research*. 2016;55(10):2903–2910.

[84] Charlton MG. Hydrogen Reduction of Tungsten Trioxide. *Nature*. 1952; 169(4290):109–110.

[85] Schubert WD, Lassner E. Production and characterization of hydrogen-reduced submicron tungsten powders—Part 1: State of the art in research, production and characterization of raw materials and tungsten powders. *International Journal of Refractory Metals and Hard Materials*. 1991;10(3):133–141.

[86] Wu C. Preparation of ultrafine tungsten powders by in-situ hydrogen reduction of nano-needle violet tungsten oxide. *International Journal of Refractory Metals and Hard Materials*. 2011;29(6):686–691.

[87] Singla G, Singh K, Pandey OP. Structural and thermal properties of in-situ reduced WO_3 to W powder. *Powder Technology*. 2013;237:9–13.

[88] Zimmerl T, Schubert WD, Bicherl A, Bock A. Hydrogen reduction of tungsten oxides: Alkali additions, their effect on the metal nucleation process and potassium bronzes under equilibrium conditions. *International Journal of Refractory Metals and Hard Materials*. 2017;62:87–96.

[89] Sarmah T, Aomoa N, Bhattacharjee G, Sarma S, Bora B, Srivastava DN, Bhuyan H, Kakati M, De Temmerman G. Plasma expansion synthesis of tungsten nanopowder. *Journal of Alloys and Compounds*. 2017;725:606–615.

[90] Shin D, Swain B, Han C, Kim Y, Lee CG, Park KS. Comparison of different tungsten precursors for preparation of tungsten nanopowder by RF induction thermal plasma. *International Journal of Refractory Metals and Hard Materials*. 2020; 86:104995.

[91] Ryu T, Sohn HY, Hwang KS, Fang ZZ. Chemical vapor synthesis (CVS) of tungsten nanopowder in a thermal plasma reactor. *International Journal of Refractory Metals and Hard Materials*. 2009;27(1):149–154.

[92] Gromov A, Kwon YS, Choi PP. Interaction of tungsten nanopowders with air under different conditions. *Scripta Materialia*. 2005;52(5):375–380.

[93] Xiao J, Liu P, Liang Y, Li HB, Yang GW. Super-stable ultrafine beta-tungsten nanocrystals with metastable phase and related magnetism. *Nanoscale*. 2013; 5(3):899–903.

[94] Schottle C, Bockstaller P, Gerthsen D, Feldmann C. Tungsten nanoparticles from liquid-ammonia-based synthesis. *Chem Commun (Camb)*. 2014;50(35):4547–50.

[95] Sahoo PK, Kalyan Kamal SS, Premkumar M, Jagadeesh Kumar T, Sreedhar B, Singh AK, Srivastava SK, Chandra Sekhar K. Synthesis of tungsten nanoparticles by solvothermal decomposition of tungsten hexacarbonyl. *International Journal of Refractory Metals and Hard Materials*. 2009;27(4):784–791.

[96] Sun GD, Wang KF, Song CM, Zhang GH. A low-cost, efficient, and industrially feasible pathway for large scale preparation of tungsten nanopowders. *International Journal of Refractory Metals and Hard Materials*. 2019;78:100–106.

[97] Zhang S, Wen Y, Zhang H. Low temperature preparation of tungsten nanoparticles from molten salt. *Powder Technology*. 2014;253:464–466.

[98] Ricceri R, Matteazzi P. A study of formation of nanometric W by room temperature mechanosynthesis. *Journal of Alloys and Compounds*. 2003;358(1-2):71–75.

[99] Purwanto A, Lenggoro IW, Chang HW, Okuyama K. Preparation of submicron- and nanometer-sized particles of Y_2O_3:Eu^{3+} by flame spray pyrolysis using ultrasonic and two-fluid atomizers. *Journal of Chemical Engineering of Japan*. 2006; 39(1):68–76.

[100] Athanassiou EK, Grass RN, Stark WJ. Large-scale production of carbon-coated copper nanoparticles for sensor applications. *Nanotechnology*. 2006;17(6):1668–73.

[101] Hirano T, Kikkawa J, Rinaldi FG, Kitawaki K, Shimokuri D, Tanabe E, Ogi T. Tubular Flame Combustion for Nanoparticle Production. *Industrial and Engineering Chemistry Research*. 2019;58(17):7193–7199.

[102] Young R. *The rietveld method*. Oxford University Press. 1993.

[103] Coelho AA. TOPAS and TOPAS-Academic: an optimization program integrating computer algebra and crystallographic objects written in C++. *Journal of Applied Crystallography*. 2018;51(1):210–218.

[104] Coward HF, Jones GW. *Limits of flammability of gases and vapors*, vol. 503. US Government Printing Office. 1952.

[105] Gordon S, McBride BJ. Computer Program for Calculation of Complex Chemical Equilibrium. *NASA reference publication*. 1994;1311.

[106] Rinaldi FG, Arutanti O, Arif AF, Hirano T, Ogi T, Okuyama K. Correlations between Reduction Degree and Catalytic Properties of WO_x Nanoparticles. *ACS Omega*. 2018;3(8):8963–8970.

[107] Chatten R, Chadwick AV, Rougier A, Lindan PJ. The oxygen vacancy in crystal phases of WO_3. *J Phys Chem B*. 2005;109(8):3146–56.

[108] Liang TY, Chen HH, Tsai DH. Nickel hybrid nanoparticle decorating on alumina nanoparticle cluster for synergistic catalysis of methane dry reforming. *Fuel Processing Technology*. 2020;201:106335.

[109] Kinoshita T, Adachi M. Submicron Particle Synthesis of $Gd_{0.1}Ce_{0.9}O_{1.95}$, NiO–$Gd_{0.1}Ce_{0.9}O_{1.95}$ and $La_{0.8}Sr_{0.2}CoO_3$ by Ultrasonic Spray Pyrolysis. *Journal of Chemical Engineering of Japan*. 2015;48(3):238–244.

[110] Xie FY, Gong L, Liu X, Tao YT, Zhang WH, Chen SH, Meng H, Chen J. XPS studies on surface reduction of tungsten oxide nanowire film by Ar^+ bombardment. *Journal of Electron Spectroscopy and Related Phenomena*. 2012;185(3-4):112–118.

[111] Strobel R, Baiker A, Pratsinis SE. Aerosol flame synthesis of catalysts. *Advanced Powder Technology*. 2006;17(5):457–480.

[112] Fujiwara K, Okuyama K, Pratsinis SE. Metal–support interactions in catalysts for environmental remediation. *Environmental Science: Nano*. 2017;4(11):2076–2092.

[113] Guntner AT, Abegg S, Konigstein K, Gerber PA, Schmidt-Trucksass A, Pratsinis SE. Breath Sensors for Health Monitoring. *ACS Sens*. 2019;4(2):268–280.

[114] Beér JM, Chigier NA, Davies TW, Bassindale K. Laminarization of turbulent flames in rotating environments. *Combustion and Flame*. 1971;16(1):39–45.

[115] Ishizuka S, Shimokuri D, Ishii K, Okada K, Takashi K, Suzukawa Y. Development of practical combustion using tubular flames. *J Combust Soc Japan*. 2009;156:104–113.

[116] Ishizuka S, Motodamari T, Shimokuri D. Rapidly mixed combustion in a tubular flame burner. *Proceedings of the Combustion Institute*. 2007;31(1):1085–1092.

[117] Sauer VM, Fachini FF, Dunn-Rankin D. Non-premixed swirl-type tubular flames burning liquid fuels. *Journal of Fluid Mechanics*. 2018;846:210–239.

[118] Maron Sauer V, Dunn-Rankin D. Liquid Fuel Nonpremixed Swirl-Type Tubular Flame Burner. *Combustion Science and Technology*. 2018;pp. 1–12.

[119] Pham TK, Dunn-Rankin D, Sirignano WA. Flame structure in small-scale liquid film combustors. *Proceedings of the Combustion Institute*. 2007;31(2):3269–3275.

[120] Wei J, Ren Y, Zhang Y, Shi B, Li S. Effects of temperature-time history on the flame synthesis of nanoparticles in a swirl-stabilized tubular burner with two feeding modes. *Journal of Aerosol Science*. 2019;133:72–82.

[121] Wang WN, Purwanto A, Lenggoro IW, Okuyama K, Chang H, Jang HD. Investigation on the Correlations between Droplet and Particle Size Distribution in Ultrasonic Spray Pyrolysis. *Industrial and Engineering Chemistry Research*. 2008; 47(5):1650–1659.

[122] Egerton AC, Powling J. The limits of flame propagation at atmospheric pressure II. The influence of changes in the physical properties. *Proceedings of the Royal Society of London Series A Mathematical and Physical Sciences*. 1948;193(1033):190–209.

[123] Hirano T, Kikkawa J, Shimokuri D, Nandiyanto ABD, Ogi T. Sinter-Necked, Mixed Nanoparticles of Metallic Tungsten and Tungsten Oxide Produced in Fuel-Rich Methane/Air Tubular Flames. *Journal of Chemical Engineering of Japan*. 2021; 54(10):557–565.

[124] Park S, Baek JH, Zhang L, Lee JM, Stone KH, Cho IS, Guo J, Jung HS, Zheng X. Rapid Flame-Annealed $CuFe_2O_4$ as Efficient Photocathode for Photoelectrochemical Hydrogen Production. *ACS Sustainable Chemistry and Engineering*. 2019; 7(6):5867–5874.

[125] Shi X, Fields M, Park J, McEnaney JM, Yan H, Zhang Y, Tsai C, Jaramillo TF, Sinclair R, Nørskov JK, et al. Rapid flame doping of Co to WS_2 for efficient hydrogen evolution. *Energy & Environmental Science*. 2018;11(8):2270–2277.

[126] Cho IS, Logar M, Lee CH, Cai L, Prinz FB, Zheng X. Rapid and controllable flame reduction of TiO_2 nanowires for enhanced solar water-splitting. *Nano Lett*. 2014;14(1):24–31.

[127] Cai L, Cho IS, Logar M, Mehta A, He J, Lee CH, Rao PM, Feng Y, Wilcox J, Prinz FB, Zheng X. Sol-flame synthesis of cobalt-doped TiO_2 nanowires with enhanced electrocatalytic activity for oxygen evolution reaction. *Phys Chem Chem Phys*. 2014;16(24):12299–306.

[128] Feng Y, Cho IS, Rao PM, Cai L, Zheng X. Sol-flame synthesis: a general strategy to decorate nanowires with metal oxide/noble metal nanoparticles. *Nano Lett*. 2013;13(3):855–60.

[129] Feng Y, Cho IS, Cai L, Rao PM, Zheng X. Sol-flame synthesis of hybrid metal oxide nanowires. *Proceedings of the Combustion Institute*. 2013;34(2):2179–2186.

[130] Cho IS, Lee CH, Feng Y, Logar M, Rao PM, Cai L, Kim DR, Sinclair R, Zheng X. Codoping titanium dioxide nanowires with tungsten and carbon for enhanced photoelectrochemical performance. *Nat Commun*. 2013;4:1723.

PUBLICATIONS

REFEREED JOURNAL ARTICLES

1. **Tomoyuki Hirano**, Shuhei Nakakura, Febrigia Ghana Rinaldi, Eishi Tanabe, Wei-Ning Wang, Takashi Ogi, Synthesis of Highly Crystalline Hexagonal Cesium Tungsten Bronze Nanoparticles by Flame-assisted Spray Pyrolysis, *Advanced Powder Technology*, 29 (19), 2512-2520, 2018.

2. Febrigia Ghana Rinaldi, Osi Arutanti, Aditya Farhan Arif, **Tomoyuki Hirano**, Takashi Ogi, Kikuo Okuyama, Correlations between Reduction Degree and Catalytic Properties of WO_x Nanoparticles, *ACS Omega*, 3 (8), 8963-8970, 2018.

3. Shuhei Nakakura, Aditya Farhan Arif, Febrigia Ghana Rinaldi, **Tomoyuki Hirano**, Eishi Tanabe, Ratna Balgis and Takashi Ogi, Direct Synthesis of Highly Crystalline Single-phase Hexagonal Tungsten Oxide Nanorods by Spray Pyrolysis, *Advanced Powder Technology*, 30 (1), 6-12, 2019.

4. **Tomoyuki Hirano**, Jun Kikkawa, Febrigia Ghana Rinaldi, Kenshi Kitawaki, Daisuke Shimokuri, Eishi Tanabe, Takashi Ogi, Tubular Flame Combustion for Nanoparticle Production, *Industrial & Engineering Chemistry Research*, 58 (17), 7193-7199, 2019.

5. Takashi Ogi, Hiromitsu Fukazawa, Annie Mufyda Rahmatika, **Tomoyuki Hirano**, Kiet Le Anh Cao, Ferry Iskandar, Improving the crystallinity and purity of monodisperse Ag fine particles by heating colloidal sprays in-flight, *Industrial & Engineering Chemistry Research*, 59 (13), 5745-5751, 2020.

6. Leon Gradon, Ratna Balgis, **Tomoyuki Hirano**, Annie Mufyda Rahmatika, Takashi Ogi, Kikuo Okuyama, Advanced aerosol technologies towards structure and morphologically controlled next-generation catalytic materials, *Journal of Aerosol Science*, 149, 105608, 2020.

7. **Tomoyuki Hirano**, Daiki Tomonaga, Daisuke Shimokuri, Takashi Ogi, Direct spray combustion in a tubular flame burner toward fine particle synthesis, *Journal of Thermal Science and Technology*, 16 (3), JTST0035, 2021.

8. Asep Bayu Dani Nandiyanto, Yusuke Kitou, **Tomoyuki Hirano**, Risti Ragadhita, Le Hoai Phong, and Takashi Ogi, Correlation between particle/crystallite size and photoluminescence of spherical submicron YAG:Ce particles, *RSC Advances*, 11 (48), 30305-30314, 2021.

9. **Tomoyuki Hirano**, Jun Kikkawa, Daisuke Shimokuri, Asep Nandiyanto, Takashi Ogi, Metallic tungsten nanoparticles produced in inner reducing gas region of tubular flames, *Journal of Chemical Engineering of Japan*, 54 (10), 557-565, 2021.

10. Eka Lutfi Septiani, Jun Kikkawa, Kiet Le Anh Cao, **Tomoyuki Hirano**, Nobuhiro Okuda, Hiroyuki Matsumoto, Yasushi Enokido, and Takashi Ogi, Direct synthesis of submicron FeNi particles via spray pyrolysis using multiple reduction agents, Direct synthesis of submicron FeNi particles via spray pyrolysis using various reduction agents, *Advanced Powder Technology*, 32 (11), 4263-4272, 2021.

11. **Tomoyuki Hirano**, Takama Tsuboi, Eishi Tanabe, Takashi Ogi, *In-situ* flame deposition of Pt catalysts on Nb-doped SnO_2 nanoparticles, *Journal of Alloys and Compounds*, 898 (25), 162749, 2022.

BOOK CHAPTERS

1. Takashi Ogi, **Tomoyuki Hirano**, Synthesis of Core-shell Composite Nanoparticles by CVD, in "Novel Technology for the Control of Surface and Composite Structure of Powder Materials -Fundamentals and Applications-", Techno system Co., Ltd., Tokyo, Japan, 177-182, 2018. (in Japanese)

2. Takashi Ogi, **Tomoyuki Hirano**, Gas Phase Process, in "Novel Technology for the Control of Surface and Composite Structure of Powder Materials -Fundamentals and Applications-", Techno system Co., Ltd., Tokyo, Japan, 3-11, 2018. (in Japanese)

3. Takashi Ogi, **Tomoyuki Hirano**, Control of nanostructure of particle and its applications, in "How to synthesize, use, and characterize of PCP/MOF and other porous materials", Technical Information Institute Co., Ltd., Tokyo, Japan, 333-346, 2019. (in Japanese)

REVIEW

1. Takashi Ogi, **Tomoyuki Hirano**, Flame assisted nanoparticles synthesis for the near-infrared shielding materials, *Earozoru Kenkyu*, 34 (1), 1–6, 2019. (in Japanese)

2. **Tomoyuki Hirano** and Takashi Ogi, Tubular Flame Synthesis of Fine Particles, *Earozoru Kenkyu*, 35 (4), 1-7, 2020. (in Japanese)